GDAŃSK UNIVERSITY OF TECHNOLOGY

FACULTY OF MECHANICAL ENGINEERING AND SHIP TECHNOLOGY

Faculty of Mechanical Engineering and Ship Technology

The author of the PhD dissertation: Stanisław Głuch
Scientific discipline: Mechanical Engineering

DOCTORAL DISSERTATION

Title of PhD dissertation: Flow condensation of new refrigeration fluids in minichannels at the parameters close to the thermodynamic critical point

Title of PhD dissertation (in Polish): Kondensacja w przepływie nowych czynników chłodniczych w minikanałach przy parametrach bliskich termodynamicznemu punktowi krytycznemu

Supervisor *signature*	~~Second supervisor~~ *signature*
prof.dr hab.inż. Dariusz Mikielewicz	
Auxiliary supervisor *signature*	~~Cosupervisor~~ *signature*
dr. inż. Tacjana Niksa-Rynkiewicz	

Gdańsk, year 2024

STATEMENT

The author of the PhD dissertation: Stanisław Głuch

I, the undersigned, agree/do not agree* that my PhD dissertation entitled:
Flow condensation of new refrigeration fluids in minichannels at the parameters close to the thermodynamic critical point
may be used for scientific or didactic purposes.[1]

Gdańsk,.....

.....
signature of the PhD student

Aware of criminal liability for violations of the Act of 4th February 1994 on Copyright and Related Rights (Journal of Laws 2006, No. 90, item 631) and disciplinary actions set out in the Law on Higher Education (Journal of Laws 2012, item 572 with later amendments),[2] as well as civil liability, I declare, that the submitted PhD dissertation is my own work.

I declare, that the submitted PhD dissertation is my own work performed under and in cooperation with the supervision of prof.dr hab.inż. Dariusz Mikielewicz and the auxiliary supervision of dr. inż. Tacjana Niksa-Rynkiewicz.

This submitted PhD dissertation has never before been the basis of an official procedure associated with the awarding of a PhD degree.

All the information contained in the above thesis which is derived from written and electronic sources is documented in a list of relevant literature in accordance with art. 34 of the Copyright and Related Rights Act.

I confirm that this PhD dissertation is identical to the attached electronic version.

Gdańsk,.....

.....
signature of the PhD student

I, the undersigned, agree/do not agree* to include an electronic version of the above PhD dissertation in the open, institutional, digital repository of Gdańsk University of Technology, Pomeranian Digital Library, and for it to be submitted to the processes of verification and protection against misappropriation of authorship.

Gdańsk,.....

.....
signature of the PhD student

*) delete where appropriate.

[1] Decree of Rector of Gdansk University of Technology No. 34/2009 of 9th November 2009, TUG archive instruction addendum No. 8.

[2] Act of 27th July 2005, Law on Higher Education: Chapter 7, Criminal responsibility of PhD students, Article 226.

DESCRIPTION OF DOCTORAL DISSERTATION

The Author of the PhD dissertation: Stanisław Głuch

Title of PhD dissertation: Flow condensation of new refrigeration fluids in minichannels at the parameters close to the thermodynamic critical point

Title of PhD dissertation in Polish: Kondensacja w przepływie nowych czynników chłodniczych w minikanałach przy parametrach bliskich termodynamicznemu punktowi krytycznemu

Language of PhD dissertation: English

Supervision: Dariusz Mikielewicz

Auxiliary supervision: Tacjana Niksa-Rynkiewicz

Date of doctoral defense:

Keywords of PhD dissertation in Polish: Kondensacja w przepływie; Ciśnienie zredukowane; Współczynnik przejmowania ciepła; Termodynamiczny punkt krytyczny, Struktury przepływu; Mapy przepływu, Uczenie maszynowe; Jednokierunkowa sieć neuronowa

Keywords of PhD dissertation in English: Flow Condensation; Reduced Pressure; Heat transfer coefficient; Thermodynamic critical point; Flow patterns; Flow maps prediction; Machine learning; Feedforward neural network

Summary of PhD dissertation in Polish: Rozprawa ma na celu opracowanie metody przewidywania przejmowania ciepła podczas kondensacji w przepływie, zwłaszcza przy wysokich wartościach ciśnienia zredukowanego i temperatury nasycenia. Rozbudowano stanowisko laboratoryjne, przeprowadzono próby odbiorowe i wykonano kampanię pomiarową. Zebrano dane eksperymentalne dotyczące kondensacji w przepływie R1233zd(E) w minikanale przy średnich i wysokich wartościach temperatur nasycenia. Zmierzono współczynnik przejmowania ciepła dla kondensacji w przepływie w poziomej rurce miedzianej o średnicy wewnętrznej 3 mm. Eksperyment przeprowadzono dla temperatur nasycenia z zakresu od 83°C do 152°C, co odpowiada wartościom ciśnienia zredukowanego od 0,2 do 0,8. Zarejestrowano struktury przepływu wewnątrz badanej sekcji pomiarowej na odcinku szklanej rurki o średnicy 3 mm. Opracowano eksperymentalne mapy przepływu na podstawie danych eksperymentalnych z 4 źródeł literaturowych. Ponadto zebrano obszerną bazę danych punktów eksperymentalnych z literatury, dotyczącą wymiany ciepła, na którą składa się 4659 punktów dla 25 płynów. Zebrana baza danych obejmuje zakres ciśnienia zredukowanego od 0,1 do 0,9 dla różnych wartości prędkości masowych i średnic sekcji pomiarowych. Opracowano dwa alternatywne modele wyznaczania współczynnika przejmowania ciepła podczas kondensacji w przepływie. Pierwszy, to modyfikacja rozwijanego od lat modelu półempirycznego opartego o hipotezę energetyczną do przewidywania współczynnika przejmowania ciepła podczas kondensacji. Drugie podejście to model wykorzystujący jednokierunkową sieć neuronową do przewidywania współczynnika przejmowania ciepła. Dodatkowo opracowano mapy struktur przepływu dwufazowego podczas kondensacji w zakresie przejścia od przepływu pierścieniowego do obszaru przejściowego i pojedynczych pęcherzyków.

Summary of PhD dissertation in English: The dissertation aims to develop a method for predicting heat transfer during flow condensation, especially at high values of reduced pressure and saturation temperature. The existing laboratory testing rig has been expanded, acceptance tests have been performed and measurement campaign has been conducted. Experimental data were collected on flow condensation of R1233zd(E) in a mini-channel at medium and high values of saturation temperatures. The heat transfer coefficient for flow condensation in a horizontal copper tube with an

inner diameter of 3 mm was investigated. The experiment was carried out for saturation temperatures in the range from 78°C to 152°C, corresponding to reduced pressure values from 0.2 to 0.8. The flow structures inside the test measurement section on a section of a glass tube with a diameter of 3 mm was recorded. Experimental flow maps were developed based on experimental data from 4 literature sources. In addition, an extensive database of experimental heat transfer coefficient points from the literature was collected, consisting of 4659 points for 25 fluids. The collected database covers the range of reduced pressure from 0.1 to 0.9 for different values of mass velocities and test section diameters. Two alternative models for determining the heat transfer coefficient during flow condensation were developed. The first is a modification of the semi-empirical model based on the energy dissipation hypothesis, an in-house model which has been under development for years, for predicting the heat transfer coefficient during condensation. The second approach is a model using a unidirectional neural network to predict the heat transfer coefficient. In addition, maps of two-phase flow structures during condensation were developed in terms of the transition from annular flow to the transition region and single bubbles.

Acknowledgements

I would like to express my gratitude and appreciation to my supervisor Prof. Dariusz Mikielewicz for his guidance and support during my PhD research and studies.

Also, I would like to thank to my auxiliary supervisor PhD Tacjana Niksa-Rynkiewicz for her help and guidance.

I would like to give my thanks to my family, especially my wife, for invaluable support. Without their assistance I would not be able to complete my PhD journey.

Stanislaw Głuch

TABLE OF CONTENTS

LIST OF IMPORTANT SYMBOLS AND ABBREVIATIONS

A	cross section, m^2
ANN	Artificial Neural Network, -
Bd	Bond number $Bd = [d^2(\rho_l - \rho_v)g]/\sigma$, -
Bo	Boiling number $Bo = q/(h_{lv} \cdot G)$, -
CNN	Convolutional Neural Network, -
CNN	Convolutional Neural Network, -
Con	Confinement Number $Con = \left(\frac{\sigma}{g(\rho_l - \rho_v)}\right)^{0.5}/d$, -
c_p	specific heat capacity, J/(kg·K)
d	diameter, m
E	energy dissipation, W/m^3
Eo	Eötvös number $Eo = [d^2(\rho_l - \rho_v)g]/[8\sigma]$, -
FNN	Feedforward Neural Network, -
Fr	Froude number $Fr = G^2/gd\rho$, -
g	gravity acceleration, m/s^2
G	mass velocity, $kg/(m^2 \cdot s)$
GPR	Gaussian Process Regression, -
H	Enthalpy, J/kg
h	specific enthalpy, J/kg
HFO	hydrofluoroolefins, -
h_{lv}	latent heat of evaporation, J/kg
HRBF	Hierarchical Radial Basis Function, -
HTC	heat transfer coefficient, $kW/(m^2 \cdot K)$
HVAC	heating, ventilation, air conditioning,
I	electric current, A
J	dimensionless phase velocity, -
KNN	K-Nearest Neighbors, -
l	length, m
LSFM	Least Square Fitting Method, -
MAE	Mean Absolute Error, -
MAPE	Mean Absolute Percentage Error, -
ML	Machine Learning, -
MSE	Mean Squared Error, -
Nu	Nusselt number, $Nu = \alpha/(d\lambda)$
p	pressure, N/m^2
p_{per}	perimeter, m

Pr	Prandtl number $Pr = \frac{c_p \mu}{\lambda}$, -
Q	heat, W
q	heat flux, W/m^2
R	thermal resistance, K/W
RBF	Radial Basis Function, -
Re	Reynolds number $Re = \frac{GD}{\mu}$, -
ReLu	rectified linear unit – activation function for Artificial Neural Networks, -
R_{MS}	two phase multiplier due to Muller-Steinhagen and Heck, -
Su	Suratman number, $Su = \frac{\rho \sigma d}{\mu^2}$, -
SVR	Support Vector Regression, -
T	temperature; °C
U	electrical potential difference, V
v	specific volume, m^3/kg
We	Weber number $We = \frac{G^2 D}{\rho l}$, -
x	vapour quality, -
XGboost	Extreme Gradient Boosting, -
X_{tt}	Martinelli's correlating parameter $X_{tt} = \left[\frac{\mu_l}{\mu_v}\right]^{0.1} \cdot \left[\frac{1-x}{x}\right]^{0.9} \cdot \left[\frac{\rho_v}{\rho_l}\right]^{0.5}$, -
z	Shah corelating parameter, -
$\dot{m}$	mass flow, kg/s
±	uncertainty, -

Greek symbols:

α	heat transfer coefficient, W/(m^2 ·K)
φ	void fraction, -
λ	thermal conductivity, W/(m ·K)
μ	dynamic viscosity, Pa ·s
ν	kinematic viscosity, m^2/s
ρ	density, kg/m^3
σ	surface tension, N/m
ω	vector of initial weights for Artificial Neural Networks, -
η	efficiency, -

Subscripts and superscripts:

b/i	bubbly flow to intermittent flow transition
crit	critical
exp	experimental

g	gas
i/a	intermittent flow to bubbly flow transition
l	liquid
lo	liquid only
pred	predicted
pre	preheater
r	reduced conditions
sat	saturation
TP	two phase
TPC	two phase condensation
v	vapour
vo	saturated vapour

1. INTRODUCTION AND OBJECTIVES OF THE THESIS

Detailed knowledge on the thermal-hydraulic behaviour of working fluids which are not planned to be phased out and are acceptable for application in modern technical applications is indispensable. High temperature heat pumps (HTHPs) are one of the key technologies envisaged for the green energy transition. They provide an opportunity to utilize low and medium temperature waste heat for industrial processes with a use of electricity from zero-emission sources. The key process of HTHP performance is flow condensation under high saturation temperature. Most literature condensation studies were executed for conventional conditions where saturation temperatures range from -20°C to 40°C. Additionally, there are also applications in power engineering of modern working fluids, just to mention the transcritical thermodynamic cycles or supercritical cycles. Knowledge of the specifies of the condensation is of very high demand. There is a gap in knowledge regarding the flow pattern and heat transfer coefficient during condensation of low-boiling working fluids in the range of high saturation temperatures (above 100°C) and medium and high reduced pressures (0.5-0.9). Data in the literature are available for similar values of reduced pressures but for lower values of saturation temperatures. Moreover, many studies examining high saturation temperature condensation utilize refrigerants which are phased out for new applications due to the ozone-depleting potential ODP and global warming potential GWP. At high values of reduced pressure, the density of gas phase is relatively high, and the density of liquid phase is low. Additionally, there is a low specific volume difference between liquid and gas phases, the liquid phase surface tension value tend to decrease. The gas phase has a relatively high viscosity, and the liquid phase has a reduced value of viscosity. These changes in the parameters of refrigerants cause significant differences in flow patterns and heat transfer coefficients. Most of the literature models for condensation heat transfer prediction are based on specific experimental parameters and are not general in nature for applications to fluids and non-experimental thermodynamic conditions. Two qualitatively different accurate heat transfer prediction models were developed. For the prediction of the heat transfer coefficient during condensation at moderate and high reduced pressures the in-house semi-empirical model has been modified. This method is based on the analysis of the dissipation of energy on two-phase flow. The second model utilises the Feedforward Neural Network for the prediction of heat transfer coefficient during condensation. Additionally, the method to predict flow pattern transition from annular flow to coalescing bubble regime and isolated bubble regime has been devised. Flow patterns affect heat transfer mechanisms during two-phase flow and knowledge about them is often utilised in heat transfer models. All three developed models show very good if not excellent agreement with experimental data from literature and collected experimentally.

1.1. Research motivation

The condensation process in high-temperature heat pumps occurs at temperatures above 100˚C, yet there is a notable knowledge gap for saturation temperatures exceeding 100˚C as the industrial requirements are to reach condensation temperatures reaching even 250°C. Data on high reduced

pressures at these temperatures is scarce or even non-existent. Most existing experimental data pertains to saturation temperatures below 40˚C, relevant to refrigeration or air-conditioning applications. At temperatures above 100˚C, most refrigerants operate near their thermodynamic critical point, leading to rapid changes in viscosity and density in the liquid and vapour phases, significantly affecting interfacial interactions. During the 2022 energy price crisis, there emerged an increased demand for industrial high-temperature heat pumps (HTHPs), which facilitate energy recovery and utilization in industrial processes. These pumps often operate near the critical point, where thermal and hydraulic issues are not well understood. Most research has focused on carbon dioxide, with much less on water and even fewer studies on other fluids. The available data is consolidated into a database, but only a few experiments address condensation at high saturation temperatures near the critical point. The basic characteristics in flows through the channels at close to critical parameters has been studied since the 50's of last century. Key challenges observed include:

1. The fluid is very expandable, while the thermal diffusivity tends to zero due to very low thermal conductivity and high specific heat.
2. The thermal properties change nonlinearly, which is different from normal liquid or gas flow and leads to the new flow structures.
3. The absence of surface tension and a capillary effect leads to low pressure loss and low flow friction. complex buoyancy effects
4. The buoyancy effect can be more complex
5. here are expected thermal-mechanical effects and several time and spatial scales, related to thermal equilibrium or stability evolution in confined spaces

Environmental and safety regulations necessitate the search for new working fluids, many of which are mixtures with insufficiently studied physical characteristics. These mixtures complicate the near-critical area due to temperature glide effects and differing thermal and flow properties of the components, risking the formation of difficult-to-control vapour-liquid mixtures. This is also true for media containing additives like refrigerant oils, air, or inert gases. The unique and dynamic phenomena near the critical point require careful selection of operating parameters.

1.2. Research objective

The main research goal is to create and validate reliable prediction methods for the calculation of heat transfer coefficient during flow condensation at moderate and high values of reduced pressure, especially above a reduced pressure p_r=0.5. Reduced pressure is defined as a ratio of actual saturation pressure to the critical pressure and is commonly used for delineation of the region of interest in the two-phase region of p-v-T diagram.

The first research objective is to modify the existing flow boiling experimental facility for measurements of pressure drop and heat transfer coefficient during boiling to the capability of testing the selected

working fluids in the flow condensation mode. With that in mind, a new condensation test section has been designed, manufactured, installed and commissioned. The experimental facility allows tests up to temperature 200°C and pressure up to 40 bar. It also has a built in section enabling observation and recording of two phase flow patterns.

The second research objective is a collection of new experimental data for perspective eco-friendly working fluids with promising thermodynamics parameters as well as obeying the perspective implementation standards for potential applications in high temperature heat pumps or similar applications requiring knowledge of condensation pressure drop and heat transfer at moderate and increased reduced pressures. New data should cover the range of saturation temperatures especially above 100°C.

The third objective is to collect existing literature experimental data base especially in the vicinity of thermodynamic critical point for the sake of development of the machine learning tool for predicting the pressure drop and heat transfer in an alternative manner to the methods thus far exercised.

The final objective is to develop a robust theoretical model for accurate predictions of pressure drop and heat transfer coefficient under the influence of the reduced pressure. That activity is based in the further re-visiting of the in-house model to improve its applicability and consistency of predictions at moderate and high reduced pressures. The improved model is to be verified with own experimental data as well as data from literature with respect to different mass flow rates at varying reduced pressures, as well as channel diameters and quality.

Experimental data study of flow condensation of R1233zd(E) in minichannel at moderate and high saturation temperatures were collected. R1233zd(E) is an eco-friendly fluid with ODP 0 and GWP 1. The heat transfer coefficient was measured for flow condensation in a horizontal copper tube with a 3 mm internal diameter and a length of 50 mm. The experiment has been conducted for saturation temperatures ranging from 83°C to 152°C which corresponds to values of reduced pressures ranging from 0.2 to 0.8. Mass velocities ranged from 600 to 1000 kg/m^{2}s. The effects of reduced pressure, mass velocity, heat flux, vapour quality, and flow regime were analysed. Flow patterns were captured with a fast camera Photron UX100 inside a 3 mm glass tube. Flow pattern maps from 4 literature sources were collected. Furthermore extensive database of experimental points from literature was collected which consists of 4659 points for 25 fluids and covers a range of reduced pressure from 0.1 to 0.9 for various mass velocities and diameters.

1.2.1. Introduction to condensation

Condensation is the process of forming a liquid from vapour as a result of heat removal at saturation conditions. Saturation temperature depends on pressure and falls within the range between the triple point temperature and the critical temperature for a given substance. This allows the condensation

process to be carried out at a constant pressure and the corresponding saturation temperature. A prerequisite for condensation to occur is that the wall temperature or surrounding medium has to be below saturation temperature. Classification of condensation can be based on several factors, including [1]:

- Mode of condensation: homogeneous, dropwise, film, or direct contact.
- Fluid type: single-component, multicomponent with all components condensable, multicomponent including non-condensable component(s), etc.
- System geometry: plane surface, external, internal, etc.

There are, of course, overlaps among categories from different classification methods. However, classification based on the mode of condensation is likely the most practical.

- Homogeneous condensation

Homogeneous condensation occurs when vapour is sufficiently cooled below its saturation temperature to initiate droplet nucleation. This can be caused by the mixing of two vapour streams at different temperatures, radiative cooling of vapour no condensable mixtures (such as fog formation in the atmosphere), or sudden depressurization of vapour. Cloud formation in the atmosphere, for instance, results from the adiabatic expansion of warm, humid air masses that rise and cool. According to classical nucleation theory, in a pure, supersaturated vapour, homogeneous condensation happens when droplets reach a critical radius. These droplets are just large enough for the pressure difference between their interior and exterior to balance the surface tension force, allowing them to form in significant numbers.

- Heterogeneous condensation

The vast majority of condensation processes are heterogeneous, where droplets form and grow on solid surfaces. Significant subcooling of vapour is required for condensation to start when the surface is smooth and dry. The rate of embryo droplet generation in heterogeneous condensation can be modelled using kinetic theory, which is defined as the rate of droplet generation with critical size on a unit surface area of a clean and dry surface. This model suggests that considerable surface subcooling is necessary for nucleation to occur at a sufficiently large number of sites. However, in practice, pre-existing nucleation embryos, such as surface contaminants, enable condensation to initiate at lower wall subcooling temperatures. When liquid is present in surface cracks, rapid condensation occurs at much lower subcooling. Many oxides and corrosion products are hydrophilic, and absorbed water vapor molecules on these contaminants can act as nuclei for condensation on metallic surfaces.

- Dropwise condensation

Stable dropwise condensation occurs when the condensate liquid does not wet the surface, preventing the formation of a film. Instead, the condensate forms droplets that adhere to the surface. This mode of condensation is highly efficient for heat transfer, typically providing condensation rates an order of magnitude higher than filmwise condensation. To encourage dropwise condensation, industrial surfaces are treated to become hydrophobic that is non-wetting (with a contact angle θ>90°) using nucleation sites such for example long-chain fatty acids. In this scenario, droplets form and grow quickly, with larger droplets being removed by gravity or vapour shear, allowing the process to continue. However, maintaining these non-wetting surface characteristics can be challenging. The condensate liquid often gradually removes the promoters, and the accumulation of droplets on the surface can eventually lead to the formation of a liquid film.

- Film condensation

Film condensation is the dominant mode of condensation in most systems. Initially, the condensate forms droplets that wet the surface, and these droplets coalesce to create a continuous liquid film. This film then flows due to gravity, vapour shear, and other forces. Film condensation is common in the majority of engineering applications. The flow of liquid condensate follows the same principles as other flow fields, involving phenomena such as laminar flow, wavy flow, the transition from laminar to turbulent flow, and droplet entrainment at the film surface.

- Direct-contact condensation

Dropwise and film condensation both occur on a cold solid surface. In condensers, this surface is cooled by a secondary fluid flow, making the condenser a type of heat exchanger where the condensing fluid is separated from the secondary coolant by a solid wall. This wall introduces a thermal resistance to heat transfer between the fluids. Although this resistance is usually small and acceptable to keep the fluids separate, in some cases, the two fluid streams are brought into direct contact. An example is condensation on subcooled liquid sprays. Another example is direct-contact condensation is the rapid cooling of food in refrigerant vapour. This process allows for minimalize damage of tissue which is meant to be frozen. Direct-contact condensation is highly efficient, not only because it eliminates wall resistance but also because it allows the fluids to mix, creating large interfacial surface areas. However, direct-contact condensers are only used in specific applications since the condensate and coolant end up mixed. In most applications, it is essential to keep them separate.

1.2.2. Minichannel transition criteria

For the last 3 decades, many studies have been conducted on transition criteria between minichannels and macrochannels. Researchers have been using two approaches: one is based on geometrical

dimensions and the other is based on dimensionless criteria numbers. Most of these criteria are based on the incorporation of surface tension into the differentiation criteria leading to different non-dimensional criteria based on Bond number (Bd) Confinement number (Con) or Eötvös number (Eo). Eötvös number formula is nearly the same as the Bond number, but it is additionally divided by 8. Bond number is equal to the Confinement number raised to -2 power. Shah [2] revived on experimental data most classification methods and concluded that deviations of correlations are not related to the diameter alone or Bond number alone. Hence such criteria are not generally valid for heat transfer.

Methods based on hydraulic dimensions:

The most widely used classification is that by Kandlikar [3]. According to this method channels above hydraulic diameters d_h>3 mm are considered as conventional channels. Passages with hydraulic diameters smaller than d_h < 3mm are mini/microchannels. Mehendele et al. [4] considered minichannels as smaller than d_h <1 mm, compact heat exchangers as between 1 m and 6 mm, and conventional channels as bigger than 6 mm.

Methods based on physical criteria:

- Kew and Cornwell [5] introduced the Confinement number Con in the pioneering research paper. In their work, they proposed a criterion enabling arbitrary separation of phenomena occurring in conventional and small-diameter channels. The criterion expresses the ratio of the characteristic dimension of the boiling process to the hydraulic diameter of the channel. It includes surface tension, gravity acceleration, phase densities and diameter $\mathrm{Con} = \left(\frac{\sigma}{g(\rho_l - \rho_v)}\right)^{0.5} / d$. From this, it follows that the flow structure is significantly influenced by surface tension, which plays a dominant role in minichannels of small hydraulic diameters. According to this criterion, when the value of the Con number is greater than 0.5, two-phase flow exhibits characteristics typical of flows in channels with small hydraulic diameters.
- Ong and Thome [6,7] in experimental research concluded the lower threshold of macroscale flow is about Con= 0.3–0.4 whilst the upper threshold of symmetric microscale flow is considered to be at Co ~1, with a transition region in-between 0.3–0.4<Con<1.0.
- Tripplet at al. [8] concluded that the effect characteristic of miniscale occurs only at Con>1.
- Harirchian and Garimella [9] introduced another dimensionless number which should be lower than 160 for minichannel condition to occur $Bd^{0.5} \cdot Re < 160$. They concluded that criteria should include flow velocity.
- Li and Wu [10] proposed the relation $Bd \cdot Re^{0.5} < 200$ as the criterion for microchannel transition.
- Ullman and Brauner [11] proposed a criterion based on Eötvös number and defined it as Eo<1.6.

1.2.3. Introduction to two phase flow patterns

This introduction emphasises adiabatic flows. Co-current upflow and downflow of gas (or vapour) and liquid in a vertical tube are characterized by distinct flow structures. These structures, or "geometries," are used to classify the flows into various two-phase flow regimes or patterns. Despite the variety of names found in the literature, the most commonly accepted vertical channel regimes are known as: bubbly flow, slug flow, churn flow, annular flow, and mist flow. This methodology is based on [12]. Flow patterns in horizontal channels are similar but additional influence comes from the presence of stratification due to gravitational force and its combination with the mass flow rate of flowing fluids. Various literature sources consider patterns between bubbly flow and annular flow as intermittent or transitional region [13–16]. These patterns are depicted in Figure 1.1 [12].

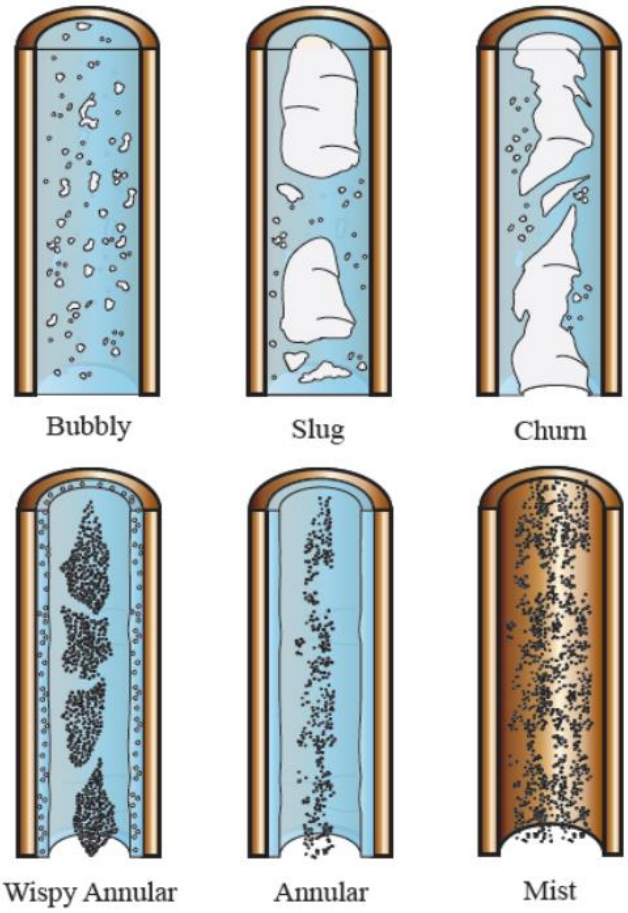

Figure 1.1 Two-phase flow patterns in vertical upflow [12]

- Bubbly flow

In this flow regime, numerous small bubbles, significantly smaller than the channel diameter, are present within the continuous liquid phase. These bubbles exhibit a wide range of sizes and shapes but are

typically densely packed, flowing closely alongside each other in succession, which creates a highly intricate flow pattern. Interaction between these bubbles includes collisions, coalescence, and breakup phenomena.

- Slug flow (intermittent/transitional)

This flow regime is distinguished by large bubbles that nearly fill the entire cross-section of the channel and are separated by distinct liquid slugs, hence its name. These bubbles have a cylindrical shape with a hemispherical front and a fluctuating blunt tail, commonly known as Taylor bubbles due to their characteristic instability. As these elongated bubbles flow, they trap a thin liquid film against the tube wall, which often descends due to gravity, even when the overall fluid flow is upward in vertical upward flow configurations. The liquid slugs between these long bubbles may contain small bubbles left over from the previous bubbly flow regime or formed by vapor condensation from the tails of the long bubbles.

- Churn flow (intermittent/transitional)

This regime represents a highly turbulent and fluctuating type of flow encountered during the transition from stable slug flow to stable annular flow. Essentially, the breakup of the tails of elongated bubbles creates large voids within the liquid slugs, destabilizing them. Subsequently, these destabilized liquid slugs affect the stability of the leading noses of the following bubbles. Additionally, the thin liquid film trapped between the long bubble and the tube wall can become unstable when gravity and shear forces exert opposing influences in vertical upward flow conditions. Churn flow is typically undesirable in two-phase piping due to its tendency to induce pressure and flow oscillations. Some flow pattern maps classify this regime as part of the transition region, or intermittent region, between slug flow and annular flow, akin to the transition from laminar to turbulent flow in single-phase flow, and therefore do not categorize it as a distinct flow pattern.

- Annular Flow

This flow regime is known for the continuous annular liquid film that moves along the inner perimeter of the channel, with a central core of higher-velocity gas or vapor. The interface of the annular liquid film is disrupted by high-frequency waves and ripples. Additionally, liquid droplets are typically carried within the gas core, and small bubbles may be trapped in the annular film due to roll waves. This flow pattern is notably stable and is preferred in piping systems and at the outlets of evaporator tubes. In instances where entrained droplets travel in periodic coherent structures resembling clouds or wisps within the central vapor core, some flow pattern maps classify this as wispy annular flow. However, generally, for practical purposes, this regime is considered as annular flow. Wispy annular flow occurs at high values of reduced pressure when bubbles can be observed inside liquid film.

- Mist flow

Mist flow occurs when the gas (or vapor) phase serves as the continuous phase, with numerous very small droplets entrained within it. These droplets are often difficult to observe without the aid of illumination or magnification. Mist flow typically occurs at high vapor qualities, where the annular liquid film is thinned by the shear forces of the gas core on the interface until it becomes unstable. This instability causes all the liquid to be entrained as droplets within the continuous gas phase. Mist flow can also occur during flow boiling when the critical heat flux is exceeded. Intermittently, impinging liquid droplets locally wet the tube wall, but overall heat transfer efficiency is significantly reduced compared to annular flow conditions.

The second even more significant orientation for two-phase flows is in horizontal channel. Most heat exchanger applications utilise horizontal orientation. The flow patterns in horizontal tubes are similar to those in vertical flows, except for the effects of flow stratification. In horizontal two-phase flow, buoyancy forces cause the liquid to settle at the bottom of the tube and the gas to rise to the top. At high enough flow rates, the influence of buoyancy becomes negligible, and the flow patterns resemble those in vertical flows. As in vertical channel patterns between bubbly flow and annular flow can be considered as intermittent/transitional [13–16]. Figure 1.2 [17] illustrates the flow patterns for co-current flow of gas and liquid in a horizontal tube.

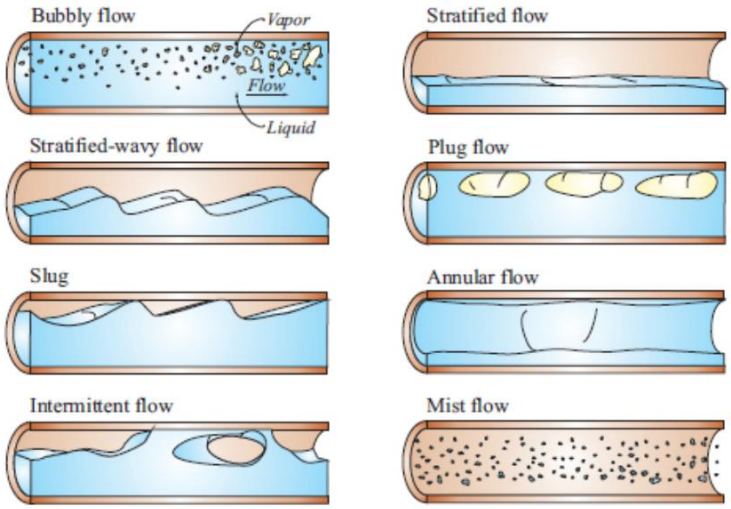

Figure 1.2 Two-phase flow patterns in horizontal flow [17]

- Bubbly flow (intermittent/transitional)

Many small gas bubbles are found throughout the continuous liquid phase, but their buoyancy causes them to accumulate in the upper portion of the tube. With increased liquid flow rates, shear forces become predominant, leading to a more even distribution of bubbles throughout the tube. In horizontal

flow scenarios, a bubbly flow pattern usually occurs only at higher mass flow rates, as lower rates tend to cause the numerous bubbles in the upper section to merge quickly into fewer, larger elongated bubbles.

- Stratified flow (intermittent/transitional)

When buoyancy forces prevail at low velocities of both liquid and gas, complete phase separation occurs: the gas flows along the upper part of the channel while the liquid flows along the bottom. The interface between the two phases remains nearly flat, with minimal wave formation.

- Stratified – wavy flow (intermittent/transitional)

As the gas velocity in a stratified flow increases, interfacial shear on the liquid surface generates waves that propagate in the flow direction and tend to wrap around the perimeter towards the top of the tube. These waves exhibit notable amplitudes; however, their crests do not typically reach the top of the tube. Typically, a significant portion of the upper perimeter of the tube remains dry, although occasional large amplitude waves may intermittently wet it.

- Intermittent flow (intermittent/transitional)

As the gas velocity is further increased, the interfacial waves grow consistently larger, sufficiently wetting the top perimeter of the tube. This results in a continuous liquid film around the entire perimeter of the tube. The large amplitude waves are interspersed with smaller amplitude waves that do not reach the top of the channel. Within the large waves, entrained bubbles are often observed, trapped by the rolling motion of these waves. The liquid segments separating these large, elongated bubbles can also be likened to large periodic amplitude waves. This characteristic defines the regime known as intermittent flow. Intermittent flow is sometimes classified into two distinct regimes: plug flow and slug flow.

- Slug and plug flow (intermittent/transitional)

The slug flow regime describes a flow pattern where large, elongated gas bubbles move along the top of the channel while the liquid phase forms a continuous flow beneath them. These elongated bubbles typically have diameters smaller than the diameter of the tube, allowing the liquid to flow continuously alongside and beneath them. Slug flow occurs when gaseous fraction is increased and diameters of elongated bubbles are similar to tube diameter.

- Annular flow

Similarly to vertical flows, as the gas flow rate increases, the liquid forms a continuous film around the tube's perimeter. Initially, this annular liquid film is thicker at the bottom of the pipe compared to the top. With further increases in gas flow rates, the thickness of the annular liquid ring becomes uniform throughout. The interface between the liquid annulus and the vapor core is disturbed by waves, and droplets may be dispersed within the gas core. At higher gas fractions, the thinner film at the top of the tube dries out first, leaving the annular film covering only the lower perimeter of the tube. This configuration can also be classified as a stratified-wavy flow regime.

- Mist flow

Similarly to vertical flow scenarios, at very high gas velocities, all the liquid in the tube can be stripped from the wall and dispersed as small droplets within the now continuous gas phase. This stripping process typically starts at the top of the tube where the liquid film is thinner, and then progresses downstream until all of the liquid is entrained as droplets. Occasionally, rivulets of liquid can also be observed following the breakdown of the liquid film, representing liquid that has not yet been entrained into the gas phase.

1.2.4. Two phase flow characteristics at increased values of saturation pressure

At higher reduced pressures, both surface tension and phase density differences decrease significantly. These changes affect flow patterns, pressure drop and heat transfer during two phase flows. Changes of thermofluidic parameters for R1233zd(E) with increasing value of reduced pressure is presented in Figure 1.3. Vertical axis represent percentage value of parameters in comparison to their maximal value. The Confinement number Con [5] characterizes the effects occurring in channels As mentioned earlier it has been introduced to distinguish between conventional size channels and minichannels. It exhibits changes in buoyancy and gravitational forces. This also characterise changes in flow nature at high reduced pressures. It encompasses the densities of both gas and liquid phases, surface tension, diameter, and gravitational acceleration. This adjustment allows for the consideration of the alterations in physical properties that influence the heat transfer process under high reduced pressures. Experimental research [18] has demonstrated that surface tension and density play significant roles in determining two-phase flow structures. For instance, at a reduced pressure 0.2, where surface tension and the disparity in phase densities are substantial, annular flow was observed even at a quality as low as 7%. Conversely, at a reduced pressure 0.8, near the critical point, annular flow appeared at 50% vapour quality. As can be noticed a significant variation of properties can be observed beyond values of reduced pressure p_r>0.65.

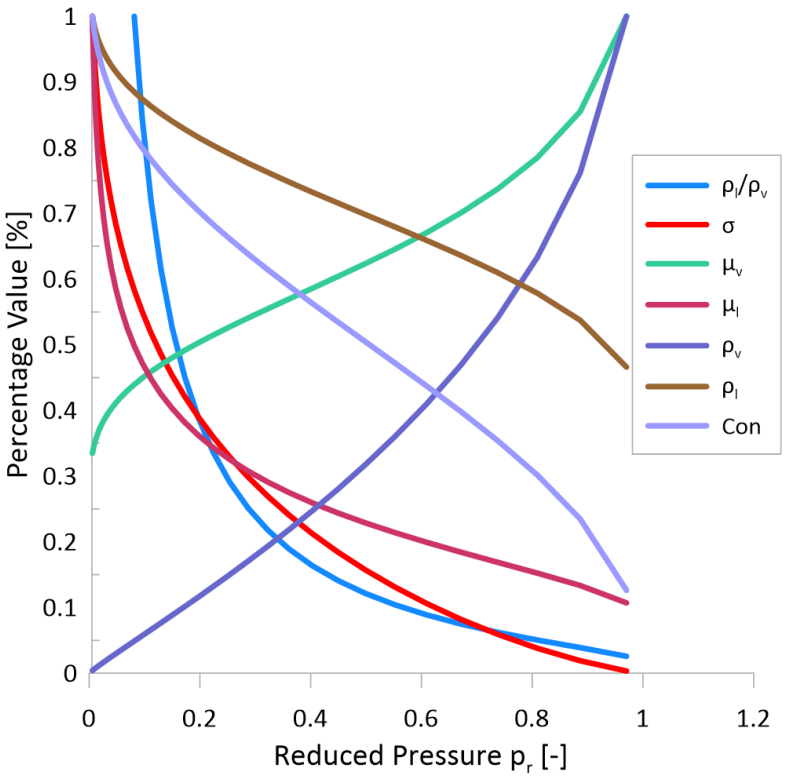

Figure 1.3 Properties change in function of reduced pressure for R1233zd(E)

2. STATE OF THE ART LITERATURE SURVEY ON FLOW CONDENSATION

2.1. Heat transfer experiments

In this section state of the art experiments investigating heat transfer coefficient experimental studies during flow condensation are presented and discussed. As mentioned earlier most conducted experiments are reported in literature for standard condensation conditions for HVAC applications, that is below 40 °C. Studies presented in the further served for collection of a database which subsequently was used in the analysis. Author exercised efforts to cover as wide range of saturation temperature and reduced pressure as possible to obtain a possibly complete picture of the flow condensation process. Data reported in the literature reached reduced pressure up to 0.9 and saturation temperatures up to 94 °C. Only a few experiments surpassed the value of reduced pressure of 0.6. Author did not find any experiment which covered temperatures above 100°C, not mentioning higher values, which could be encountered in high temperature heat pump or power engineering application. The most notable experiments in case of measurement technique development or most distinct results are discussed. It is worth to note that high reduced pressures do not always correspond to high saturation temperatures. There are refrigerants for which the critical point is at moderate temperatures or even below 0°C, but corresponding reduced pressures are very high. Consolidated database is presented in the last subsection in Table 2.1. Bandhauer and Garimella [19] developed thermal amplification technique for condensation two phase measurements in microchannels. The high heat transfer coefficients and low mass flow rates characteristic of microchannels pose challenges for precise measurement. Accurate heat duty measurement requirements conflict with the need to deduce heat transfer coefficients from observed temperatures and flow rates. Additionally, measuring local condensation heat transfer coefficients for small quality increments is challenging due to the low heat transfer rates associated with such changes. To alienate these issues the inlet and outlet qualities of a microchannel test section are determined via energy balances on pre- and post-condensers. The test section is cooled with water at a high flow rate to ensure the condensation side is the primary thermal resistance. A secondary cooling water stream at a much lower flow rate creates a significant temperature difference, which was used to measure the condensation duty. Local heat transfer coefficients were measured in small increments throughout the entire saturated vapor-liquid region. The technique was demonstrated with a square microchannel geometry having a hydraulic diameter of 0.76 mm. The heat transfer coefficients for R134a refrigerant condensation in this setup ranged from 2110 to 10640 W/(m²·K) over a mass flux range from 150 to 750 kg/(m²·s). Thermal amplification technique developed by Bandhauer and Garimella was utilised in my experiment.

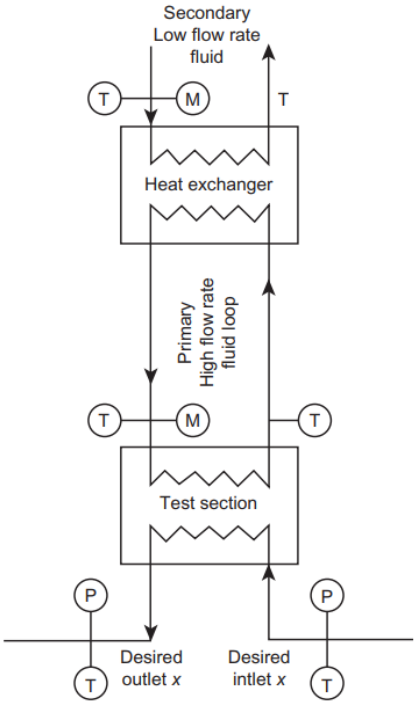

Figure 2.1 Thermal amplification technique

Jiang in [20] performed comprehensive investigation on the heat transfer and pressure drop of refrigerant R404A during condensation and supercritical cooling at near-critical pressures inside a 9.4 mm tube. The study examined five nominal pressures: 0.8, 0.9, 1.0, 1.1, and 1.2 times the critical pressure (p_{crit}). Heat transfer coefficients were accurately measured using a thermal amplification technique, which also provided refrigerant heat transfer coefficients with low uncertainties. For condensation tests, local heat transfer coefficients and pressure drops were measured over the mass flux range from 200 to 800 kg/(m²·s) in small quality increments across the entire vapor-liquid region. For supercritical tests, local heat transfer coefficients and pressure drops were measured within the same mass flux range for temperatures from 30°C to 110°C. In both phase-change condensation and supercritical cooling, frictional pressure gradients were calculated by isolating the deceleration component due to momentum change from the measured pressure gradients. Jiang further developed the measurement technique. She compared the methods of calculation heat transfer coefficient by measurements of wall temperature and by measurements of temperature before and after tests section. Difference in both methods was only 2.63%. For experiments the second method was utilised. Subsequent co-workers of prof. Garimella, i.e. Milkie [21], Keinath [22], Macdonald [23] also used the second technique. Such method has also been applied in the present study.

Mcdonald and Garimella [23,24] presented findings from an experimental study on propane condensation inside horizontal tubes at three different mass fluxes, two tube diameters, and reduced pressures ranging from 0.25 to 0.95. These conditions are relevant to the process and HVAC&R

industries due to their typical saturation pressures and mass fluxes. In this first part of a two-part study, the trends in heat transfer coefficients and frictional pressure gradients under these conditions are analysed, and comparisons are made with existing models from the literature. The study observed a slight increase in heat transfer coefficients with larger tube diameters, contrary to the predictions of most correlations. High-speed flow visualization results from a previous study, conducted in the same test facility, help explain this trend. None of the existing heat transfer coefficient correlations from the literature adequately predicted all the results of the present study, particularly at higher reduced pressures where their performance worsened. Similarly, no existing correlation accurately predicted the measured frictional pressure drops. In the companion paper, Part II, the heat transfer and pressure drop results from this study are used to develop correlations applicable to a broader range of operating conditions.

Cavallini et al. [25] investigated the condensation heat transfer coefficients and two-phase frictional pressure drops for R32 and R245fa in a single circular channel with a 0.96 mm diameter. These two HFC fluids have significantly different thermodynamic properties. R32 has critical pressure 57.8 bar and critical temperature 78°C while corresponding values for R245fa are 36.5 bar and 154°C. Despite this, the heat transfer coefficients for both fluids are similar under identical experimental conditions (mass flux and vapour quality). However, the frictional pressure drop is significantly higher for the low-pressure refrigerant, which is expected. The experimental heat transfer coefficient values indicate that condensation is primarily shear stress dominated for most data points. Under these operating conditions, the Cavallini et al.[26] model for macroscale condensation accurately predicted the heat transfer coefficients.

Del Col et al. [27] presented a new test section designed and built to measure the heat transfer coefficient during condensation in a 1.18 mm high square cross-section channel. Contrary to experiments conducted by team of prof. Garimella the developed test section is long and it is designed to measure multiple local heat transfer coefficients. Length of this test section is 220 mm. The experimental technique has proven to be highly accurate on single-phase heat transfer tests. Additionally, pressure drop tests were conducted in both laminar and turbulent flow. By comparing the laminar flow friction factor with theoretical predictions, the geometric dimensions of the channel were verified. A detailed error analysis was performed for the condensation tests, focusing particularly on the uncertainty related to heat flux. Overall, in the quality range between 0.9 and 0.1, the experimental uncertainty never exceeds 6% for mass fluxes equal to or greater than 200 kg/m²·s. When comparing the heat transfer coefficients to those previously measured in a circular channel, it is observed that heat transfer is enhanced in a square channel at 200 kg/m²·s, likely due to surface tension effects, while this enhancement is not present at higher mass fluxes. It was recommended that further research is needed to verify the heat transfer enhancement at lower mass fluxes.

Zhuang et al. [28] studied the condensation heat transfer and pressure drop of R170 in a horizontal tube with an inner diameter of 4 mm. The tests were conducted at saturation pressures ranging from 1 MPa to 2.5 MPa, with mass fluxes between 100 kg/m²·s and 250 kg/m²·s, and average heat fluxes from 55.3 kW/m² to 96.3 kW/m² across the entire vapor quality range. The effects of vapor quality, mass flux, and saturation pressure on condensation heat transfer and pressure drop were examined and analysed.

The experimental data were compared with various well-known correlations for condensation heat transfer coefficient and pressure drop. The consolidated database is presented in Table 2.1. It consists of data presented in 28 publications for 21 fluids. In these collected experiments mass velocity varies from 75 to 1400 kg/(m^2s), whereas the reduced pressure covers the range from 0.1 to 0.9. Experiments were conducted for various test section diameters ranging from 0.76 mm to 15 mm. All sources were used for classical prediction methods of heat transfer. Data for saturation temperatures ranging from - 107°C to 91°C were collected. One of the objectives of the present work is to develop an Artificial Neural Network for heat transfer coefficient predictions. With that in mind the first 22 sources featuring almost 3940 data points were used to train the developed neural network. The 6 last sources were intended for ANN testing as the excluded databases. Artificial intelligence have a capability to account the systematic measurement errors which lead to the results being clearly better than the uncertainty propagation. It is important to conduct test on databases from experiments which were unavailable for learning.

Table 2.1 Consolidated database

	Authors	Diameter [mm]	Fluid [-]	Synthetic S or Natural N	Mass Velocity G [kg/(m2·s)]	Reduced Pressure p_r [-]	Saturation Temperature Ts [°C]	Number of Points [-]
1	Macdonald and Garimella [23,24]	0.76-1.45	R290	N	150-450	0.254-0.809	30-94	260
2	Aroonat [29]	8.1	R134a	S	300-500	0.251-0.325	40-50	54
3	Cavallini et al. [30]	8	R22, R410a, R32, R236ea,R134a, R125	S	100-800	0.307-0.55	40	251
4	Cavallini et al. [31]	1.4	R134a, R410a	S	200-1400	0.251	40	196
5	Cavallini et al. [25]	0.96	R32, R254fa	S	100-1200	0.068-0.428	40	117
6	Keinatch [22]	0.86-3	R404a	S	200-800	0.382-0.618	30-60	522
7	Garimella et al. [32]	0.76-1.52	R410a	S	200-800	0.805-0.899	60.95 – 66.35	214
8	Jiang et al. [33]	9.4	R410a, R404a	S	200-800	0.8005-0.9	60.95 – 67.15	416
9	Andersen [34]	3.05	R410a	S	400-800	0.8	60.92	52
10	Del Col et al. [35]	0.96	R1234yf	S	200-1000	0.3007	40	67
11	Del Col et al. [36]	0.762	Propane	N	100-1000	0.3225	40	63
12	Longo et al. [37]	4	R290, Propylene, R404a	S and N	75-300	0.25-0.322	30-40	194
13	Longo et al. [38]	4	R32, R410a	S	100-800	0.33-0.49	30-40	159
14	Longo et al. [39]	4	R134a, R152a, R1234yf, R1234ze(e)	S	75-600	0.13-0.3	30 – 40	280
15	Ghim and Lee [40]	7.75	R245fa	S	150-500	0.093	40 – 50	20
16	Patel et al. [41]	1	R134a, R1234yf	S	202-811	0.256-0.3	40	77
17	Zhuang et al. [28]	4	Ethane	N	101-255	0.22-0.522	(-29.51) – (2.9)	230
18	Song et al. [42]	4	R14	S	200-650	0.27-0.79	(-84.76) – (-53.17)	189
19	Zhuang et al. [43]	4	Methane	N	99-254	0.43-0.76	(-107.3) – (-91.21)	286
20	Milkie et al. [21]	7.75	R245fa, n-Pentane	S and N	150-600	0.04-0.17	44-75	266
21	Keniar and Garimella [44]	1.55	R245fa, R134a, R1234ze(E)	S	50-200	0.05-0.32	30-50	149
22	Moriera et al. [45]	9.43	R134a, Propylene, R290, R600a	S and N	50-250	0.12-0.32	35	140
23	Huang et al. [46]	1.6	R410a	S	200-600	0.49	35	35
24	Illan-Gomez et al. [47]	1.16	R1234yf	S	350-945	0.23-0.43	30-50	219
25	Del Col et al. [48]	1	Propylene	N	80-1000	0.35	40	109
26	Azzolin et al. [49]	3.4	R134a	S	50-200	0.25	40	73
27	Berto et al. [50]	3.38	R245fa	S	30-150	0.68	40	124
28	Present study	3	R1233zde(E)	S	600-1000	0.178-0.81	78.7-152.1	42
	Summary	0.76-9.4	26 fluids	S and N	75-1400	0.103-0.9	(-107.3) – 152.1	4700

2.2. Classical heat transfer prediction methods

This subsection describes heat transfer prediction methods used in experimental data analysis. Equations are presented in the last subsection in Table 2.2. Mikielewicz and Mikielewicz [51] unveiled a model for calculating the heat transfer coefficient during condensation within channels, referred to in the remainder of the thesis as the in-house model. This method was based on the model initially developed for flow boiling, however with a capability to predict also flow condensation when the bubble generation term was switched off. The analysis aimed to predict heat transfer coefficients in flow condensation and compare the results with correlations developed for annular flow structures. In this approach, flow boiling and flow condensation were considered as symmetrical phenomena. The comparisons produced satisfactory results. Furthermore, the study investigated non-adiabatic effects in the heat transfer coefficient model, incorporating the blowing parameter into the modelling process [52]. The modifications significantly influenced condensation of low qualities, indicating that non-adiabatic effects are less critical for higher qualities. Similarly, in the case of flow boiling, the most substantial changes to the heat transfer coefficient occurred at lower qualities. Subsequently, in [53], a method for calculating the heat transfer coefficient during flow boiling was proposed, taking into account the effect of reduced pressure. This paper introduced also a modified Müller-Steinhagen and Heck two-phase multiplier to consider the effects of increased reduced pressures. Although promising results were obtained, there was still room for further improvements. In [54], the authors presented the latest version of the two-phase pressure drop model based on the Müller-Steinhagen and Heck method. That introduced modification into the shear stress between liquid phase and vapour phase in annular flow rendering that the case flow boiling was not symmetrical to condensation.

Shah [55] introduced a simple dimensionless correlation for predicting heat transfer coefficients during film condensation inside pipes. The study included various fluids like water, R-11, R-12, R-22, R-113, methanol, ethanol, benzene, toluene, and trichloroethylene condensing in horizontal, vertical, and inclined pipes with diameters from 7 to 40 mm. It also analysed condensation within an annulus. The parameters covered in the dataset included reduced pressures from 0.002 to 0.44, saturation temperatures from 21 to 31°C, vapor velocities from 3 to 300 m/s, and vapor qualities from 0 to 100%. This version was created to predict only annular flow. An updated version of the correlation, which expanded the range of parameters, was published in 2009 [56]. This method aligns well with data from both highly turbulent and laminar flow conditions. The capability to predict heat transfer in mini and microchannels was introduced in [57]. The improved versions of the correlation are significantly more complex than the original.

Cavallini et al. [26] introduced a new method for determining the condensation heat transfer coefficient of refrigerants in horizontal plain tubes with inner diameters greater than 3 mm (D > 3 mm). This method was designed for simplicity, enabling easy application in heat exchanger modelling and design for both traditional and new fluids in the HVAC industry. The method emphasizes accuracy and has been

validated against an experimental database from various researchers, ensuring reliability with minimized experimental uncertainties. It employs two equations: one for temperature difference-independent fluid flows and another for temperature difference-dependent flows, incorporating parameters that influence condensation heat transfer. The method's accuracy was confirmed through extensive comparison with data from HCFCs, HFCs, HCs, carbon dioxide, ammonia, and water. Applying the temperature-dependent part of the correlation is often challenging because the wall temperature is usually unknown. Most data sources do not provide precise experimental wall temperature values, necessitating iterative calculation for design purposes.

Bohdal et al. [58] performed experimental study of condensation heat transfer. The results of a study on heat transfer and pressure drop during the condensation of R134a and R404A refrigerants in minichannels have been discussed. The internal diameters of these minichannels ranged from 0.31 to 3.30 mm. The research focused on evaluating the local heat transfer coefficient and pressure drop within individual minichannels, comparing these findings with methods suggested by other researchers. Based on the measured data, the authors developed their own correlation for determining the local heat transfer coefficient.

Dorao and Fernandino [59] introduced a new and simple model for determining the local heat transfer coefficient during flow condensation in plain pipes. The model distinguishes between two regimes based on mass velocity values. For each regime, a new correlation is provided, which is similar to the single-phase heat transfer coefficient model. The relevant Reynolds and Prandtl numbers are calculated using the combined superficial liquid and vapor versions. These models highlight the crucial role of the superficial vapor Reynolds number in determining the heat transfer coefficient. The model I aimed to predict the heat transfer coefficient for a variety of channels, including microchannels and conventional channels, and for different refrigerants.Formulas of presented correlations for heat transfer are shown in Table 2.2. It can be observed that degree of complication differs for all methods. Some of them are straightforward while other incorporate different formulas for corresponding flow patterns or zone.

Table 2.2 Condensation heat transfer prediction methods formulas

Model	Formula	Aplicability
Mikielewicz [51,53]	$\frac{\alpha_{TPB}}{\alpha_{LO}} = \sqrt{R_{MS}^{n}}$ $R_{MS} = \left[1 + 2\left(\frac{1}{f_1} - 1\right) xCon^{m}\right] \cdot (1-x)^{\frac{1}{3}} + x^{3}\frac{1}{f_{1z}}$ turbulent flow: $f_1 = \frac{\left(\frac{\rho_l}{\rho_v}\right)}{\left(\frac{\mu_l}{\mu_v}\right)^{0.25}}$ $f_{1z} = \frac{\left(\frac{\mu_v}{\mu_l}\right)}{\left(\frac{\lambda_l}{\lambda_v}\right)^{1.5}} * \left(\frac{c_{pl}}{c_{pv}}\right)$ Laminar flow: $f_1 = \frac{\frac{\rho_l}{\rho_v}}{\frac{\mu_l}{\mu_v}}$ $f_{1z} = \left(\frac{\lambda_v}{\lambda_l}\right)$	General model for macro channels and minichannels
Bohdal [58]	$Nu = 25.084 \cdot {Re_l}^{0.258} \cdot {Pr_l}^{-0.495} \cdot Pr^{-0.288} \cdot \left(\frac{x}{1-x}\right)^{0.266}$	Model for minichannels
Dorao and Fernandiono [59]	${Nu_l} = 0.023 \cdot {Re_{tf}}^{0.8} \cdot {Pr_{tf}}^{0.3}$ ${Nu_{II}} = 41.5 * d^{0.6} \cdot {Re_{tf}}^{0.4} \cdot {Pr_{tf}}^{0.3}$ $Nu = \sqrt[9]{({Nu_l}^{9} + {Nu_{II}}^{9})}$	General model for macro channels and minichannels
Shah (1979) [55]	$\alpha = 0.023 * {Pr_l}^{0.4} * {Re_l}^{0.8} * \frac{(1-x)^{0.8} + (3.8 * x^{0.76} \cdot (1-x)^{0.04})}{{p_r}^{0.38}} \cdot \frac{\lambda_l}{d}$ $Re_l > 3000$	Model for annular flow
Shah (2009) [56]	$\alpha = hi \; for \; Jg \geq 0.98 * (z + 0.263)^{-0.62}$ $\alpha = hi + h_{Nu} \; for \; Jg < 0.98 * (z + 0.263)^{-0.62}$ $hi = 0.023 \cdot {Re_l}^{0.8} \cdot {Pr_l}^{0.4} \cdot \left(\frac{\mu_l}{14 * \mu_v}\right)^{n_2} \cdot (1-x)^{0.8} + \frac{3.8 * x^{0.76} \cdot (1-x)^{0.04}}{Pr^{0.38}} \cdot \frac{\lambda_l}{d}$ $n_2 = 0.0058 + 0.557 \cdot \mathrm{P}r$ $h_{Nu} = 1.32 * Rel^{-\frac{1}{3}} * \left[\frac{\rho_l(\rho_l - \rho_v) g k_l^{3}}{\mu l^{2}}\right]^{1/3}$ $Z = \left(\frac{1}{x-1}\right)^{0.8} \cdot Pr^{0.4}$ $Jg = \frac{xG}{\sqrt{gD\rho_v(\rho_l - \rho_v)}}$	General model for macro channels and minichannels
Shah (2019) [57]	$\alpha = hi \; for \; Jg \geq 0.98 * (z + 0.263)^{-0.62}, Fr_l > 0.012 \; and \; We_f \geq 100$ $\alpha = hi + h_{Nu} \; for \; Jg < 0.95 \cdot (1.254 + 2.27 \cdot Z^{1.249})^{-1}, Fr_l > 0.012$ $for \; other \; regimes$ $h = hII + h_{Nu}$ $hII = 0.023 \cdot {Re_l}^{0.8} \cdot {Pr_l}^{0.3} \cdot (1 + 1.128 \cdot x^{0.8170} \frac{\rho_l}{\rho_v}^{0.3685} \cdot \frac{\mu_l}{\mu_v}^{0.2363} \cdot \frac{1-\mu_v}{\mu_l}^{2.144} \cdot {Pr_l}^{-0.1} \cdot \frac{\lambda_l}{d}$ $h_{Nu} = 1.32 \cdot {Re_l}^{-\frac{1}{3}} \cdot \left[\frac{\rho_l(\rho_l - \rho_v) g k_l^{3}}{\mu l^{2}}\right]^{1/3}$ $Jg = \frac{xG}{\sqrt{gD\rho_v(\rho_l - \rho_v)}}$	General model for macro channels and minichannels

Cavallini (2006) [26]	$Jg = \frac{xG}{\sqrt{gD\rho_v(\rho_l - \rho_v)}}$ $J_G^T = \sqrt[-3]{\frac{7.5}{4.3 \cdot Xtt\text{^}1.111}^{-3} + Ct^{-3}}$ "For hydrocarbons : CT = 1.6 ; For other refrigerants : CT = 2.6" $\alpha_{LO} = 0.023 \cdot {Re_l}^{0.8} \cdot {Pra_l}^{0.4} \cdot \frac{\lambda_l}{d}$ Δ T-independent flow regime ($J_G > J_G^T$) $\alpha_A = \alpha_{LO} \cdot \left[1 + 1.128 \cdot x^{0.817} \cdot \left(\frac{\rho_l}{\rho_v}\right)^{0.3685} \cdot \left(\frac{\mu_l}{\mu_v}\right)^{0.2363} \cdot \left(1 - \frac{\mu_v}{\mu_l}\right)^{2.144} \cdot {Pr_l}^{-0.1}\right]$ Δ T-dependent flow regime ($J_G < J_G^T$) $\alpha_{strat} = 0.725\left\{1 + 0.741\left[\frac{1-x}{x}\right]^{0.3321}\right\}^{-1} \cdot \left[\frac{{\lambda_l}^3 \cdot \rho_l(\rho_l - \rho_v)g \cdot h_{lv}}{\mu_l \cdot D \cdot \Delta T}\right]^{0.25} + (1 - x^{0.087}) \cdot \alpha_{LO}$ $\alpha_D = \left[\alpha_A\left(\frac{J_G^T}{J_G}\right)^{0.8} - \alpha_{strat}\right]\left(\frac{J_G}{J_G^T}\right) + \alpha_{strat}$	General model for tubes with hydraulic diameter above 3 mm
Shah (2022) [60]	Method is almost the same as Shah 2019, but hII is replaced with Cavallini 2006 α_A for tubes with hydraulic diameter higher than 6 mm.	General model for macro channels and minichannels

2.3. Flow patterns and flow maps prediction methods

Knowledge about flow patterns is important because it allows to much better understand the nature of two phase flow and mechanisms governing pressure drop and heat transfer. Several prediction methods of heat transfer coefficient, such as methods due to Kim and Mudawar [16], Costa Patry [61], El Hajal et al. [62] or Cavallini et al. [26,63], utilise different heat transfer prediction formulas annular, intermittent and bubbly flow. It is important to accurately predict flow patterns to correctly apply heat transfer method developed for annular flow or wavy flow. These are only few cases from numerous other examples. Equations are presented in the last subsection in Table 2.3.

Cavallini et al. [63] introduced a novel predictive model designed to calculate both the heat transfer coefficient and pressure drop during condensation within smooth tubes, particularly when operating with pure or blended halogenated refrigerants, including newer high-pressure HFC fluids for which existing prediction methods are insufficient. This proposed model stems from a predictive examination of flow patterns occurring during the condensation process. To validate its efficacy, predictions from this new model are compared with experimental data provided by the authors as well as with a comprehensive experimental dataset from various independent researchers. The study involved obtaining heat transfer coefficients during the condensation process of refrigerants such as R-22, R-134a, R-125, R-32, R-236ea, R-407C, and R-410A within plain tubes with an inner diameter of 8 mm. These experiments were conducted at saturation temperatures ranging from 30 to 50°C and mass velocities varying from 100 to 750 kg/(m²·s) across the entire vapour quality spectrum. Prediction method of annular flow was proposed to utilise different calculation methods for annular flow and stratified flow regimes. Division line was based on superficial vapour velocity and was set a bit further than previous experiments to be certainly in area of annular flow.

Coleman and Garimella [64] investigated two-phase flow mechanisms during the condensation of refrigerant R134a in six small diameter tubes with round (4.91 mm), square (d_h=4 mm), and rectangular cross-sections (4x6 mm and 6x4 mm: d_h =4.8 mm; 2x4 mm and 4x2 mm: d_h =2.67 mm). Specialized experimental techniques and test sections were developed to document the flow mechanisms during the phase change. For each tube, flow mechanisms were recorded across the entire range of qualities for five different refrigerant mass fluxes between 150 and 750 kg/(m²·s). The flow mechanisms were categorized into four distinct flow regimes, namely intermittent flow, wavy flow, annular flow, and dispersed flow. Furthermore, the extensive data allowed for the identification of various flow patterns within each regime, enhancing the understanding of two-phase flow modes. Transition lines between the respective flow patterns and regimes on these maps were established based on the experimental data. It was found that for similar hydraulic diameters, the flow regime transitions are not significantly dependent on the tube shape or aspect ratio. These maps and transition lines can be used to predict the specific flow pattern or regime for a given mass flux, quality, and tube geometry. Observed flow patterns are presented in Figure 2.2.

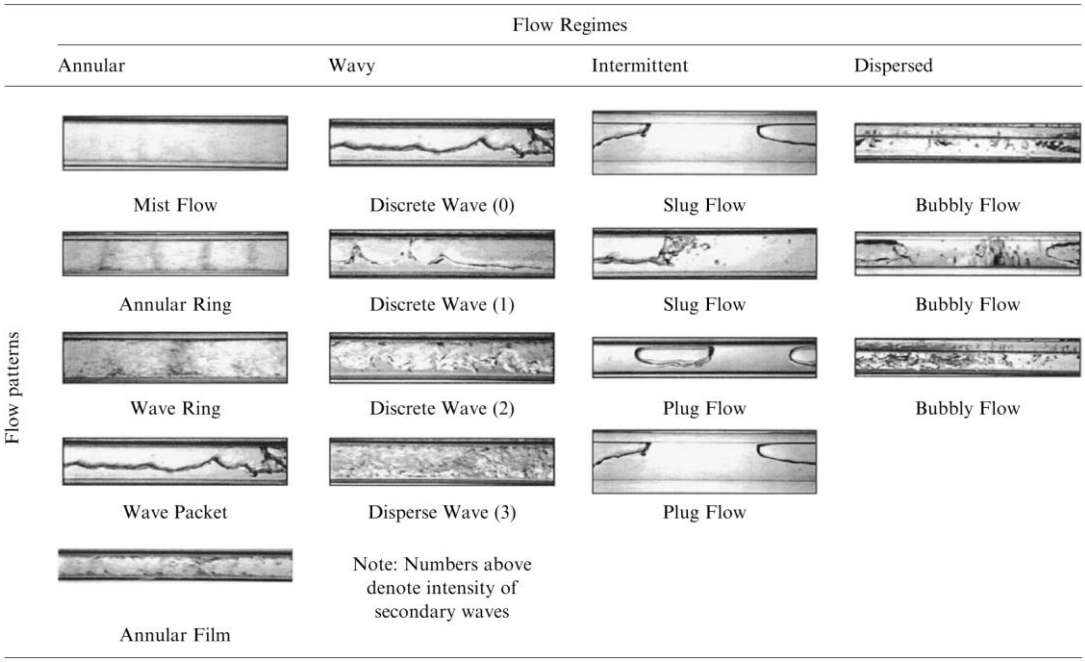

Figure 2.2 Flow patterns observed by Coleman and Garimella [64]

El Hajal et al. [62] introduced a new flow pattern map and a heat transfer model specifically tailored for condensation within horizontal plain tubes. The model is a revised version of a two-phase flow pattern map, initially developed by Kattan et al. [65] for flow boiling, which is presented in the context of condensation inside horizontal tubes. On that basis he introduced a novel heat transfer model. The updated flow pattern map integrates a newly formulated logarithmic mean void fraction approach for computing vapour void fractions across a range of pressures extending from low pressures to near-critical point conditions. Additionally, several adjustments are made to suit the requirements of

condensation rather than evaporation. Given the absence of void fraction data at elevated reduced pressures under these circumstances, the new method was indirectly validated using the convective condensation model for annular flow and corresponding heat transfer test data at reduced pressures up to 0.8. Furthermore, the new map was effectively compared with recent flow pattern observations for condensation and with other existing criteria and maps delineating flow transitions. Flow map is presented in Figure 2.3.

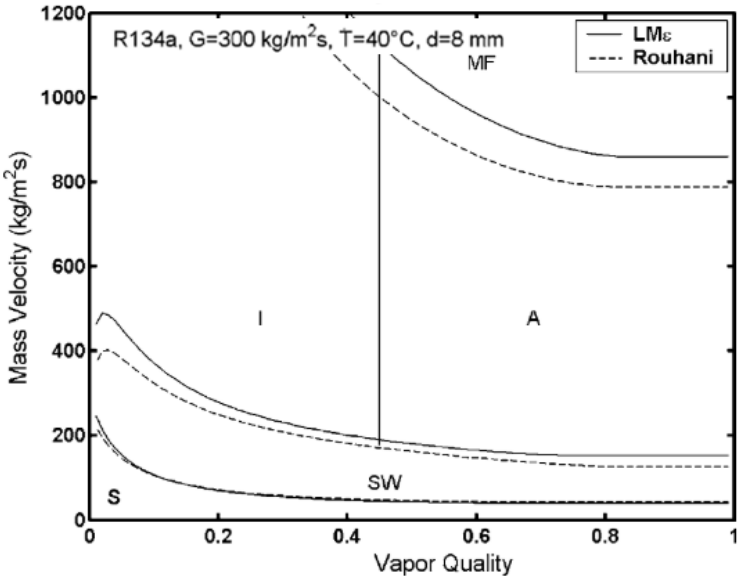

Figure 2.3 El Hajal et al. Flow pattern map comparison for R-134 at 40°C in an 8 mm tube [62]

Cheng et al. [66] developed a novel heat transfer model for flow boiling and an updated flow pattern map, both specifically tailored for CO_2 in horizontal tubes. Firstly, a nucleate boiling heat transfer correlation was introduced, which accounts for the impact of reduced pressure and heat flux, particularly at low vapour qualities for CO_2. Secondly, a nucleate boiling heat transfer suppression factor correlation is proposed, considering factors such as liquid film thickness and tube diameters. This correlation is grounded in the underlying mechanisms of flow boiling heat transfer, aiming to capture trends observed in the data. The new flow pattern map introduces criteria for transitioning from intermittent flow to annular flow and from annular flow to the dryout region, based on observed changes in flow boiling heat transfer trends. The flow boiling heat transfer model successfully predicted 75.5% of the CO_2 dataset within ±30% accuracy. Both the heat transfer model and flow pattern map are applicable across a broad range of conditions: tube diameters (or equivalent diameters for non-circular channels) ranging from 0.8 to 10 mm, mass velocities from 170 to 570 kg/(m²·s), heat fluxes from 5 to 32 kW/m², and saturation temperatures from -28 to 25 °C (corresponding to reduced pressures from 0.21 to 0.87). Flow map is similar to the one presented in Figure 2.3.

Revellin and Thome [67] published the flow pattern data and bubble measurements obtained from two small-diameter sight glass tubes which were utilized to propose a novel approach to constructing a flow

pattern map for evaporating flows in microchannels. Unlike previous methods that categorized observations into traditional flow regimes alongside an adiabatic map, this new diabatic map classifies flows into three distinct types:

1. The isolated bubble regime, characterized by a bubble generation rate significantly exceeding the bubble coalescence rate, encompassing both bubbly and slug flows

2. The coalescing bubble regime, where the bubble coalescence rate greatly surpasses the bubble generation rate, extends until the conclusion of the coalescence process

3. The annular regime, delimited by the vapour quality at the onset of critical heat flux, with its extent constrained accordingly

This formulation is deemed more beneficial for the phenomenological modelling of processes governing boiling heat transfer and two-phase pressure drops in microchannels. Additionally, it visually delineates the feasible operational limit of microchannel heat spreaders at the critical vapour quality corresponding to critical heat flux. The dataset encompasses two refrigerants (R-134a and R-245fa) and two channel diameters (0.509 and 0.790 mm). The micro-evaporator length was varied from 20 to 70 mm, inlet subcooling from 2 to 15°C, mass flux from 200 to 2000 kg/(m²·s), and heat fluxes up to 597 kW/m². Three different saturation temperatures were tested: 26°C, 30°C, and 35°C. The developed flow map is presented in Figure 2.4.

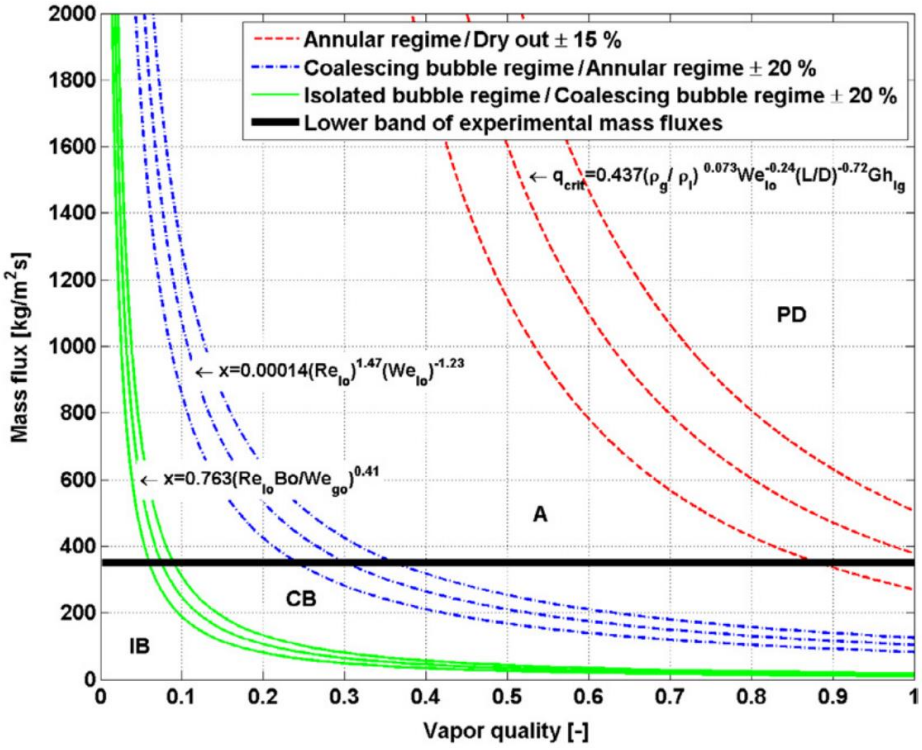

Figure 2.4 Revellin and Thome flow map with prediction formulas [67]

Kim et al. [16,68] performed a two part study on condensation heat transfer and flow pattern prediction of FC-72. In the initial phase of a two-part investigation, experiments were conducted to study the condensation process of FC-72 within parallel square micro-channels. These channels, having a hydraulic diameter of 1 mm and a length of 29.9 cm, were etched into the top surface of a solid copper plate. Operational conditions ranged from mass velocities of 68–367 kg/(m²·s), saturation temperatures of 57.2–62.3 °C, and water mass flow rates of 3–6 g/s. Through the utilization of high-speed video imaging and photomicrography techniques, researchers identified five distinct flow patterns: smooth-annular, wavy-annular, transition, slug, and bubbly, with smooth-annular and wavy-annular being the most commonly observed. The authors presented a new flow pattern prediction method based on the Soliman [13] methodology. The flow pattern prediction method was later used to predict transition regions for the new heat transfer prediction method. Flow map is presented in Figure 2.5.

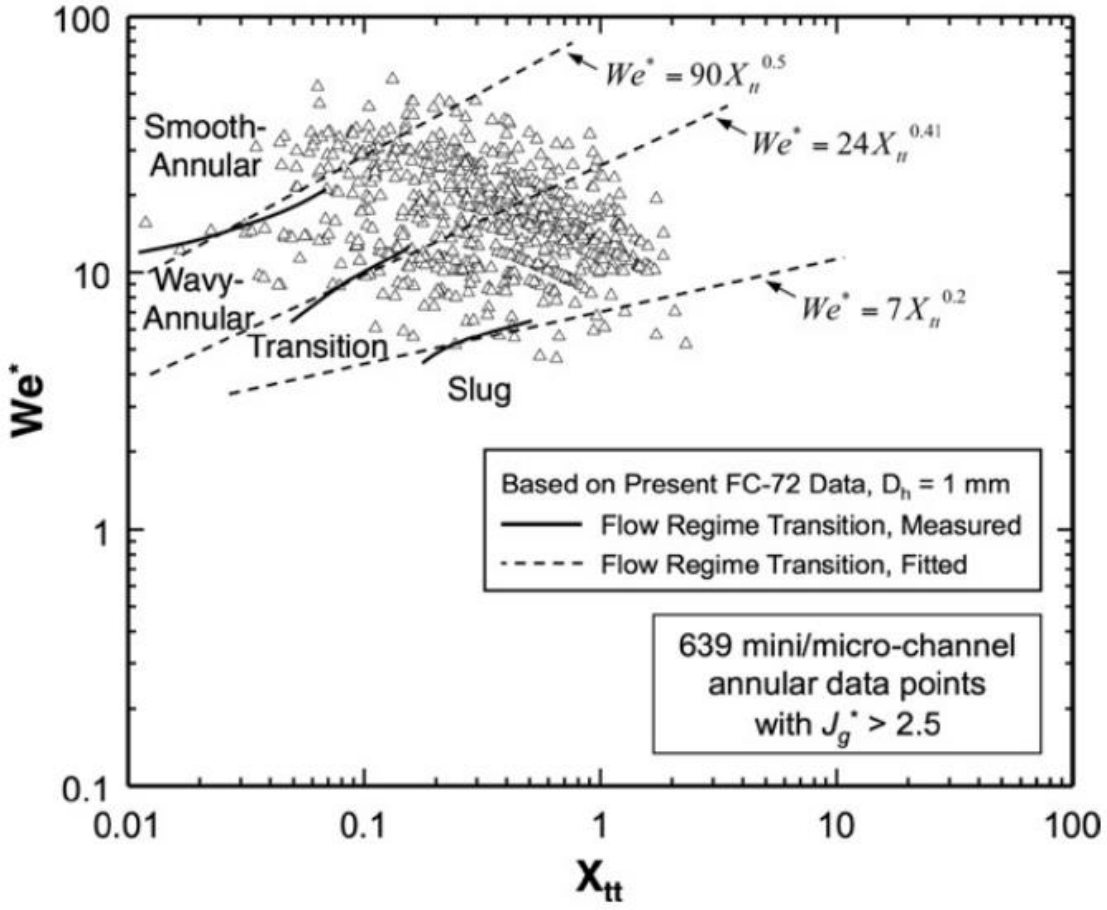

Figure 2.5 Kim and Mudawar [16] flow map based on Soliman method [13].

Zhuang et al. [14] performed a study on the behaviour of R170 in a smooth horizontal tube, focusing on its two-phase flow patterns and transition lines. Tests were conducted across various saturation pressures (ranging from 1.5 MPa to 2.5 MPa) and mass fluxes (from 100 kg/(m²·s) to 250 kg/(m²·s)) covering the full range of vapour quality. The research examined how changes in mass flux and

saturation pressure influenced the transitions between different flow patterns. It was found that the physical properties of velocity, viscosity, and surface tension played significant roles in determining the criteria for flow pattern transitions under the experimental conditions. The experimental data were compared with existing two-phase flow pattern maps for horizontal tubes, and a new map specifically for R170 in a horizontal tube, built upon prior work by Kim et al. [16] was developed. Flow map is based on Soliman method and is similar to Kim and Mudawar presented in Figure 2.5.

Charnay et al. [15] presented an experimental study which consisted of flow visualizations and measurements to discern transitions in flow regimes during the flow boiling of R-245fa within a 3.00 mm inner diameter minichannel at elevated saturation temperatures, ranging from 60°C to 120°C. Notably, flow boiling experiments at such high temperatures have been scarcely documented in existing literature. The mass velocity spanned from 100 to 1500 k kg/(m²·s), heat flux varied from 10 to 50 kW/m^2, and inlet vapour quality ranges from 0 to 1. Utilizing an image processing technique and thorough analysis of the heat transfer coefficient, four primary flow regimes are identified, namely intermittent flow, annular flow, dryout, and mist flow. Their transitions are pinpointed and mapped onto flow pattern diagrams. The impact of heat flux and saturation temperature is elucidated and discussed. Comparative assessments with transition lines documented in the literature were conducted. Despite indications of a macroscale flow regime, the observed transitions in flow patterns bore closer resemblance to those typically observed in microscale flow systems. Figure 2.6 presents flow map for R245fa boiling in 3 mm tube under 120°C saturation temperature. Only a few experimental visualization studies exceeded saturation temperature 100 °C. Other are Billiet at al.[69], Głuch et al.[18] and Pysz et al. [70]

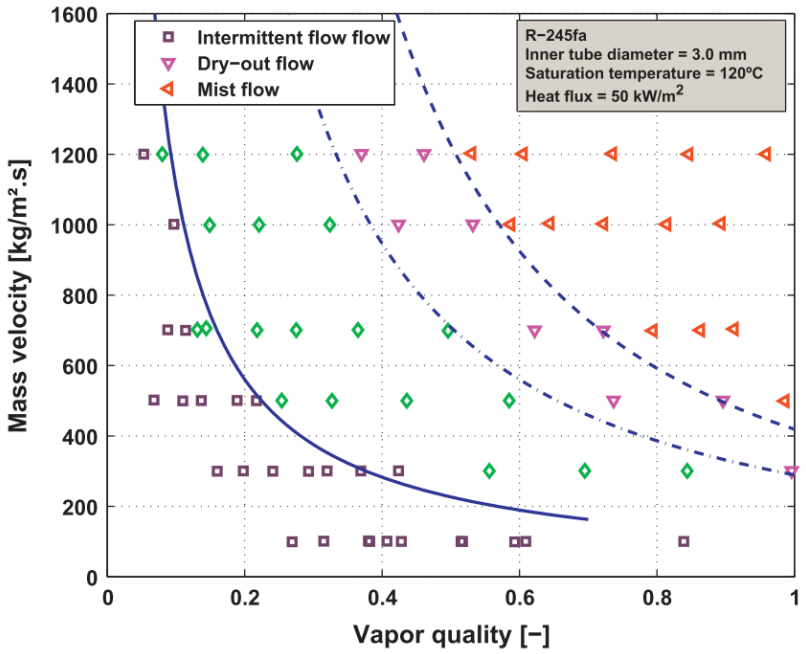

Figure 2.6 Charnay et al. map for R245fa boiling in 3 mm tube under 120°C saturation temperature

Sikora [71] experimentally investigated visualiziation the flow of three Novec refrigerants during condensation within minichannels. The experimental exploration of two-phase flow patterns was carried out in minichannels with internal diameters ranging from 0.5 to 2.5 mm. Utilizing a MATLAB algorithm, images capturing the two-phase flow structures were analysed. A two-dimensional areal quantitative stereology technique was employed to calculate void fraction. The primary objective of the investigation was to observe the flow structures formed during the condensation process. The condensation studies encompassed a broad spectrum of mass flux densities (G=80–5500 kg/(m²·s)) and saturation temperatures (Ts = 30–70°C). Critical temperatures of examined fluids is 165°C for HFE7000, 169°C for Novec649 and 195°C for HFE7100. Reduced pressure reached p_r=01.28. Based on the experimental findings, a flow structure map was developed and presented. Three principal flow structures were identified during the condensation of HFE7000, HFE7100, and Novec649 refrigerants in pipe minichannels: dispersed, stratified, and intermittent. These structures were further categorized into substructures, including mist and frothy for dispersed, annular, annular wave, and wave for stratified, and slug, plug, and bubble for intermittent. Throughout the study, frothy and wave substructures were less commonly observed, whereas annular, annular wave, and slug substructures were predominant. The visualization investigations also captured phenomena such as transitions between structures, bubble coalescence, and the simultaneous coexistence of two flow structures. Proposed flow map is presented in the Figure 2.7.

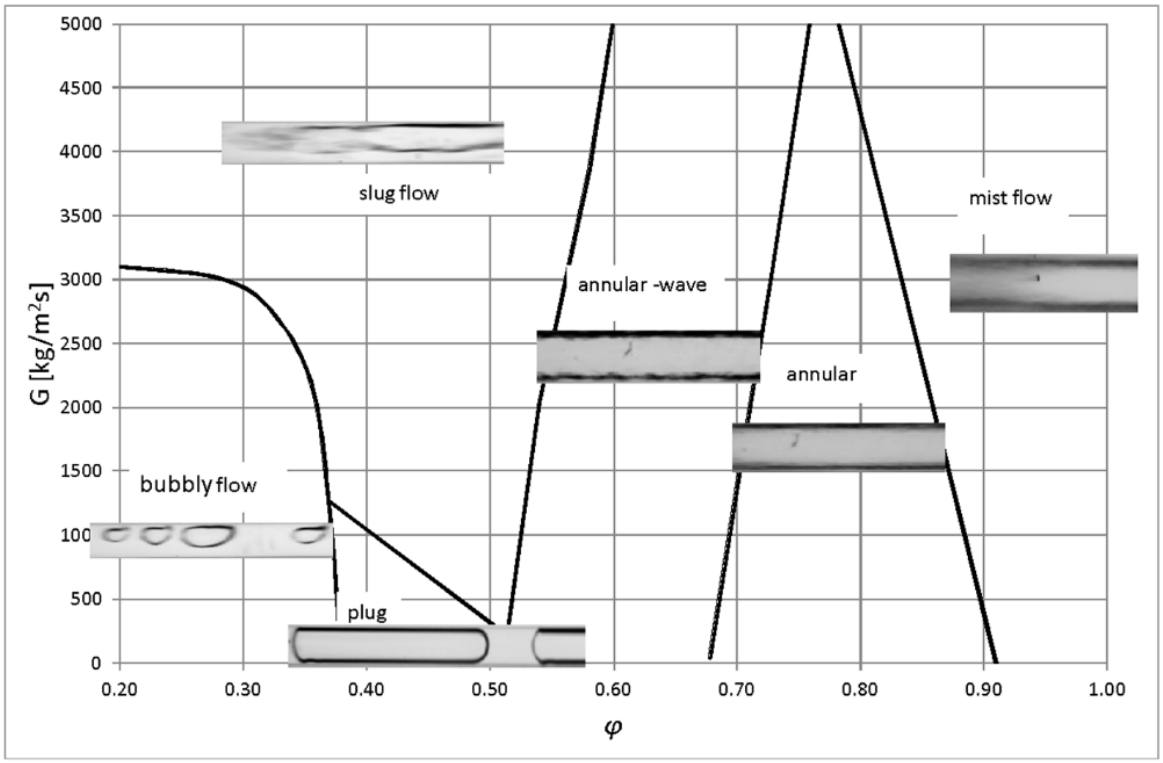

Figure 2.7 Sikora generalized flow structure map during HFE7000, HFE7100, and Novec649 refrigerant condensation in minichannels with an internal diameter of d = 0.5 ÷ 2.0 mm [71]

Głuch et al. [18] conducted experimental study of flow patterns of boiling R1233zd(E) inside a vertical 3mm channel. Unique data was gathered for reduced pressures from 0.2 to 0.8 what corresponds to a saturation temperature of 152 °C. Mass velocity was ranging from 180 to 465 [kg/(m²·s)]. At elevated reduced pressure levels, the gas phase exhibits relatively high density compared to the low density of the liquid phase, resulting in a minimal difference in specific volume between the two phases. Moreover, the liquid phase demonstrates reduced surface tension, while the gas phase exhibits comparatively higher viscosity. These alterations in refrigerant parameters lead to significant variations in flow structures. For instance, at a reduced pressure of 0.2, annular flow is observed at a quality of 0.07 for a mass velocity of G=355 [kg/(m²·s)], whereas at a reduced pressure of 0.8, annular flow occurs much later, at a quality of 0.47 for the same mass velocity. Flow maps depicting mass velocity as a function of quality for constant reduced pressure values, and flow maps illustrating reduced pressure as a function of quality at constant mass velocity are presented. These flow maps were then compared with existing literature correlations for transition lines between intermittent and annular flow structures. The authors introduced a novel correlation for the annular flow transition line for the investigated conditions. Notably, their new prediction method is the was the sole approach capable of accurately predicting the transition to annular flow at high reduced pressure levels for the collected experimental data. New flow map is presented in Figure 2.8

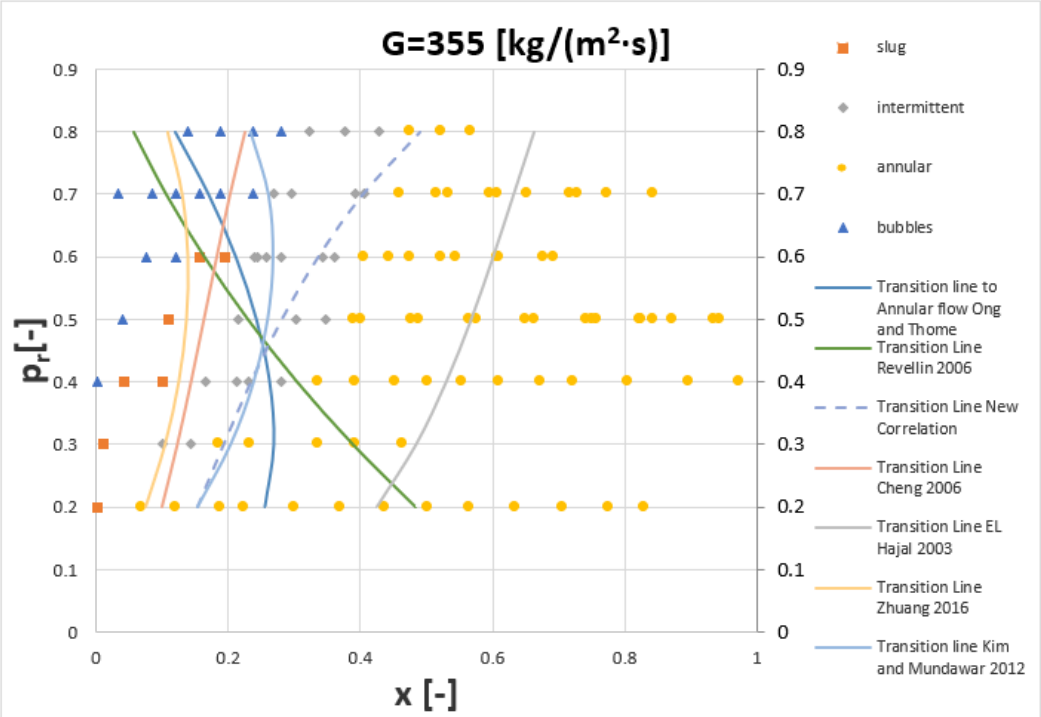

Figure 2.8 Flow map for reduced pressure ranging from 0.2 to 0.8 for mass flow 355 [kg/(m²·s)] [18]

Flow maps prediction methods formulas are presented in Table 2.3. Only transition lines from bubbly regime to intermittent regime and from intermittent regime to annular are analysed in this study.

Table 2.3 Flow maps prediction methods formulas

Author	Formula	Purpose
Cavallini 2002 [63]	annular flow transition line: $Jg \geq 2.5$ $Jg = \frac{xG}{\sqrt{gD\rho_v(\rho_l - \rho_v)}}$	Condensation inside channels above 3 mm
Cheng 2006 [66]	intermittent/annular flow transition line: $x = \left(1.8^{\left(\frac{1}{0.875}\right)} \cdot \left(\frac{\rho_v}{\rho_l}\right)^{-\frac{1}{1.75}} \cdot \left(\frac{\mu_l}{\mu_v}\right)^{-\frac{1}{7}} + 1\right)^{-1}$	evaporation
El Hajal 2003 [62]	intermittent/annular flow transition line: $x = \left(\left(0.2914 \cdot \left(\frac{\rho_v}{\rho_l}\right)^{-\frac{1}{1.75}} \cdot \left(\frac{\mu_l}{\mu_v}\right)^{-\frac{1}{7}}\right) + 1\right)^{-1}$	16 < G < 1532 kg/ (m2 s); 3:14 < d < 21:4 mm; 0:02 < pr < 0:8;
Ong Thome [7]	coalescing bubble/annular and plug–slug/annular transition line: $x = 0.047 \cdot (Con^{0.05}) \cdot \left(\frac{\mu_v}{\mu_l}\right)^{0.7} \cdot \left(\frac{\rho_v}{\rho_l}\right)^{0.6} \cdot Re_v^{0.8} \cdot We_l^{-0.91}$ isolated bubble/coalescing transition line: $x = 0.036 \cdot (Con^{0.20}) \cdot \left(\frac{\mu_v}{\mu_l}\right)^{0.65} \cdot \left(\frac{\rho_v}{\rho_l}\right)^{0.9} \cdot Re_v^{0.75} \cdot We_l^{-0.91} \cdot Bo^{0.25}$	Condensation in mini and macrochannels
Revellin 2006 [67]	coalescing bubble/annular transition line: $x = 0.00014 \cdot \frac{Re_{lo}^{1.47}}{We_{lo}^{1.23}}$ isolated bubble/coalescing transition line: $x = 0.763 \cdot \left(\frac{Re_{lo} * Bo}{We_{vo}}\right)^{0.41}$	Condensation in mini/micro channels.
Zhuang 2016 [14]	Slug to intermittent transition line: $We = 4.38 \cdot {X_{tt}}^{0.2}$ Wavy - annular to intermittent transition : $We = 18.91 \cdot {X_{tt}}^{0.33}$ We*-modified Weber number by Soliman X_{tt}-Lockhart Martinelli parameter $We^* = \frac{2.45 Re_v^{0.64}}{Su_v^{0.3}\left(1 + 1.09 * \left(\frac{\mu_v}{\mu_l}\right)^{0.1}\left(\left(\frac{1-x}{x}\right)^{0.9} * \left(\frac{\rho_v}{\rho_l}\right)^{0.5}\right)^{0.039}\right)^{0.4}}$ $We^* = \frac{2.45 Re_v^{0.64} Xtt^{0.157}}{Su_v^{0.3}(1+1.09 \cdot Xtt^{0.039})^{0.4}}\left[\left(\frac{\mu_v}{\mu_l}\right)^2 \cdot \left(\frac{\rho_l}{\rho_v}\right)\right]$	Condensation R170 insidemacrochannel
Kim and Mudawar [16]	Slug to intermittent transition line: $We = 7 \cdot {X_{tt}}^{0.2}$ Wavy - annular to intermittent transition line: $We = 24 \cdot {X_{tt}}^{0.41}$ We*-modified Weber number modified by Soliman	Condensation inside minichannel

2.4. Heat transfer prediction methods by artificial neural networks

Machine learning (ML) is a specialized field within artificial intelligence (AI) that allows computers to "self-learn" from training data and enhance their performance over time without explicit programming. ML algorithms identify patterns within data and leverage these patterns to make predictions, effectively learning from experience. In traditional programming, a software engineer writes a series of instructions that direct a computer on how to process input data to produce the desired output. Although AI and machine learning are often used interchangeably, they are distinct concepts. AI is the overarching field concerned with machines that can make decisions, acquire new skills, and solve problems in a manner similar to humans. Machine learning is a subset of AI focused on enabling systems to autonomously learn from data. Rather than programming tasks directly, machine learning involves providing algorithms with labelled examples (training data). This data enables the algorithms automatically make calculations, process information, and recognize patterns, thus improving their ability to make accurate predictions and decisions. Application of machine learning into forecasting of heat transfer in flow condensation is an novelty introduced in the present thesis. Only a small number of models is available at the moment.

Qiu et al. [72] proposed a machine learning-based approach to predict heat transfer during saturated flow boiling in mini/micro channels. A comprehensive dataset was collected comprising 16 working fluids, spanning reduced pressures from 0.0046 to 0.77, hydraulic diameters ranging from 0.15mm to 6.5mm, mass velocities from 19 to 1608 kg/(m²·s), liquid-only Reynolds numbers between 27 and 55270, and qualities from 0 to 1. An Artificial Neural Network (ANN) model was constructed using this consolidated database, with training and test data subsets. The ANN model, featuring dimensionless input parameters and hidden layers architecture, achieved a Mean Absolute Percentage Error of 14.3% in predicting test data. It outperformed conventional correlations in forecasting heat transfer during saturated flow boiling, even demonstrating high accuracy when applied to individual datasets. The robustness of the ANN model was evaluated by excluding certain databases from the training set and predicting them separately, with results indicating superior performance when including working fluid data in the training process. This study underscores the potential of a universal ANN model utilizing a consolidated dataset for accurately predicting heat transfer coefficients in saturated flow boiling within mini/micro channels.

Zhou et al. [73] performed investigation which employed a substantial dataset to construct machine-learning models aimed at predicting condensation heat transfer coefficients in mini/micro-channels. A consolidated dataset comprising 4882 data points from 37 sources is assembled, encompassing 17 working fluids and a range of parameters including reduced pressures, hydraulic diameters, mass velocities, Reynolds numbers, superficial vapor Reynolds numbers, and flow qualities. Four machine learning models—Artificial Neural Networks (ANN), Random Forest, AdaBoost, and Extreme Gradient Boosting (XGBoost)—are developed using this dataset. Through parametric optimization, ANN and XGBoost exhibited superior predictive accuracy. Notably, the optimized machine-learning models

outperform a highly reliable generalized flow condensation correlation. Furthermore, they demonstrate reasonable accuracy in predicting excluded datasheets, particularly when data points involving the specific working fluid are included in the training dataset. This research underscores the potential of machine learning algorithms as robust tools for predicting condensation heat transfer coefficients in mini/micro channels

Moradkhani et al. [74] in a paper on modelling the flow boiling heat transfer coefficient (HTC) in smooth helically coiled tubes considered dataset comprising 1035 samples from 13 independent studies, covering a wide range of geometrical and operational conditions. Evaluation of earlier models' predictive capabilities for both straight and coiled tubes using the dataset revealed their lack of precision. Consequently, a new empirical model based on the least square fitting method (LSFM) was developed, incorporating seven effective dimensionless factors as input. However, it was observed that LSFM could not adequately capture the complex and nonlinear nature of HTC in smooth helically coiled tubes. Subsequently, the genetic programming intelligent method was employed to derive a more accurate explicit correlation for HTC. Furthermore, machine learning techniques such as multilayer perceptron (MLP), Gaussian process regression (GPR), and radial basis function (RBF) were utilized to model HTC in smooth coiled tubes. While all intelligent-based models performed well, the GPR model demonstrated superior performance with an AARE of 5.93% for the tested dataset. Additionally, the study identified the most influential factors governing boiling HTC in coiled tubes.

Moradkhani et al. [75] performed study compiling an extensive dataset of experimental data points sourced encompassing 37 condensing fluids across various operational parameters. The aim was to develop robust and accurate models capable of predicting HTC in both mini/micro and conventional channel heat exchangers. Conventional intelligent techniques such as Gaussian Process Regression (GPR), Radial basis function (RBF), Hybrid Radial Basis Function (HRBF), and Least Square Fitting Method (LSFM) are employed to craft these new models. Initially, existing two-phase HTC models are evaluated using the gathered data, revealing average absolute relative error (AARE) values exceeding 29%, highlighting the need for more precise models. Through Pearson's correlation analysis, eight dimensionless groups are identified as the most crucial input parameters. The GPR model emerges as the most accurate in estimating Nusselt number for the test process, achieving an AARE of 4.50%. However, RBF and HRBF models exhibit AARE values of 19.41% and 24.36% respectively for testing data points. Furthermore, a general explicit correlation is formulated using LSFM to estimate HTC, yielding acceptable results with an AARE of 23.40% across all analysed data. The performance of these new models, along with established ones, is assessed across different channel sizes, flow regimes, fluid types, and operating conditions, demonstrating predictive capability. Finally, a sensitivity analysis is conducted based on experimental data and LSFM outcomes.

Hughes et al. investigated machine learning regression models created to anticipate the heat transfer coefficient and frictional pressure gradient during the condensation process of three zeotropic mixtures

(ethane/propane, R245fa/pentane, and R410A) in both micro- and macro-channels (with diameters ranging from 0.76 mm to 14.45 mm). A total of 1032 data points were employed to train, test, and validate four machine learning models: support vector regression (SVR), random forest regression (RFR), gradient boost (GB), and artificial neural networks (ANN). Among these, SVR exhibited the most accurate prediction of the apparent Nusselt number for testing data. To assess the impact of additional heat and mass transfer resistances in zeotropic condensation, Shapley analysis was conducted on the models to assess the importance of all dimensionless parameters employed in predicting heat transfer and pressure drop. Overall, the three most critical parameters for predicting heat transfer were identified as the Reynolds number of both phases and a dimensionless temperature glide, while for pressure drop prediction, the most significant parameters were the Bond number, Weber number, and vapor-phase Reynolds number. The significance of mass transfer is deliberated alongside the suitability of other simple mixture models. Only data from database from University of Georgia was used. The model was not tested on validation dataset for different laboratory.

Nie et al. [76] examined machine learning (ML) techniques for forecasting flow condensing HTCs in horizontal tubes, leveraging a comprehensive database. Database served to train and assess five machine learning models: K-nearest neighbours (KNN), artificial neural network (ANN), convolutional neural network (CNN), random forest (RF), and Extreme gradient boosting (XGBoost) algorithms. The developed machine learning models exhibit great predictive capabilities for 1213 test data points. Through parametric importance analysis conducted by the trained XGBoost models, a new universal correlation was formulated by integrating several key parameters to characterize condensation heat transfer. Moreover, an additional excluded database was collected to verify the universality of the new correlation and these ML models, affirming the effectiveness of ML models as predictive tools for HTCs.

Mattiuzzo et al. [77] the condensation process of two mixtures, R513A (comprising 56% R1234yf and 44% R134a by mass) and R516A (comprising 77.5% R1234yf, 14% R152a, and 8.5% R134a by mass), within channels with inner diameters of 0.96 mm and 3.38 mm. Both R513A and R516A are azeotropic blends. Condensation heat transfer tests were conducted at a saturation temperature of 40°C, with mass flux ranging from 40 kg/(m²·s) to 600 kg kg/(m²·s). The obtained heat transfer coefficient data were compared with results from three semi-empirical models and a specifically developed Artificial Neural Network model. Developed model had 12 hidden layers. Database from experiments of University of Padova was used.

Summarising the above it can be concluded that analysed works used following machine learning techniques:

- Gaussian process regression (GPR)
- Radial basis function (RBF)
- Hybrid radial basis function (HRBF)

- Least square fitting method (LSFM)
- Artificial neural network (ANN)
- K-nearest neighbours (KNN)
- Convolutional neural network (CNN)
- Random forest (RF)
- Extreme gradient boosting (XGBoost)
- Support vector regression (SVR)

Artificial neural network (ANN) and Extreme gradient boosting (XGBoost) achieved the best results among reviewed methods. The referenced studies demonstrate that using artificial intelligence methods can yield better results than traditional correlations for predicting the heat transfer coefficient [72–74,78]. Methods based on machine learning had proved to be able of prediction of two phase heat transfer coefficient with error value lower than typical measurement uncertainty. It is caused by their ability to learn also systematic errors of measurements is experiments which were used for training. Because of that it is important to conduct testing procedure also on a dataset based on experiments excluded from learning data. In this case artificial intelligence cannot predict systematic errors and results are meaningful for the real world scenario. Not all researchers conducted testing procedure on excluded data.

3. RESEARCH METHODOLOGY

As mentioned earlier experimental data study of flow condensation of R1233zd(E) in minichannels at moderate and high saturation temperatures were collected. R1233zd(E) is an eco-friendly fluid with ODP= 0 and GWP=1. The heat transfer coefficient was measured for flow condensation in a horizontal copper tube with a 3 mm internal diameter and a length of 50 mm. The experiment has been conducted for saturation temperatures ranging from 83°C to 152°C which corresponds to values of reduced pressures ranging from 0.2 to 0.8. Mass velocities ranged from 600 to 1000 kg/m^{2}s. The effects of reduced pressure, mass velocity, heat flux, vapour quality, and flow regime were analysed. In this chapter the laboratory testing stand and research methodology is described. Research methodology is based on the methodology used by prof. Garimella's team described in Garimella and Bandhauer [19] and Jiang [20]. Two major improvements have been introduced namely:

- Second loop is cooled by a laboratory ultra-thermostat, instead of municipal water, what enables control of condensation section heat duty. Too high heat duty would result in a significant quality change across the test section. It also enables measurement of wall temperature and heat flux effect on heat transfer.
- the effect of tube wall temperature distribution on heat transfer at the border of test section is incorporated into post processing code. Details are described in the subsections.

3.1. Refrigerant R1233zd(E)

R1233zd(E) is a new eco-friendly refrigerant with potential applications in ORC, HVAC and heat pumps. Its critical temperature is 165.5°C, and critical pressure is 35.73 bar. Its ozone depleting potential ODP is 0, and global warming potential GWP is 1. Its critical point parameters are nearly identical to R245fa which is widely used for ORC, but GWP of R245fa is 1030. R1233zd(E) belongs to hydrofluoroolefin (HFO) refrigerants together with R1234yf, R1234ze. R245fa, R1234yf, and R1233zd(E) critical point parameters are compared in the Table 3.1.

Table 3.1 Comparison of R245fa, R1234yf, and R1233zd(E) critical parameters

Fluid	R245fa	R1234yf	R1233zd(E)
T_{crit} [°C]	153,86	94.7	166.45
p_{crit} [bar]	36.51	33.82	36.23

3.2. Experimental setup

The measurement system operates within a closed loop for the test fluid, which includes a tank for the working fluid, circulation pump, mass flow meter, pre-heater, measuring section, and a condenser. Apparatus specification with uncertainties are presented in Table 3.2. The experimental rig is originally designed for measuring heat transfer during boiling at conditions up to 200 °C and 30 bar. It consists of stainless steel ¼-inch seamless circular tubes connected by Hy-Lok stainless steel tube fittings. The rig also includes union tees, union crosses, ball valves, needle valves, and quick connectors. NPT taper threads are used for connecting sensors and components such as the pump, as they maintain a seal under high pressure. All components are designed to ensure safe operation under high pressure and temperature. Scheme of the testing rig is presented in Figure 3.1, whereas the general view of the facility is presented in Figure 3.2.

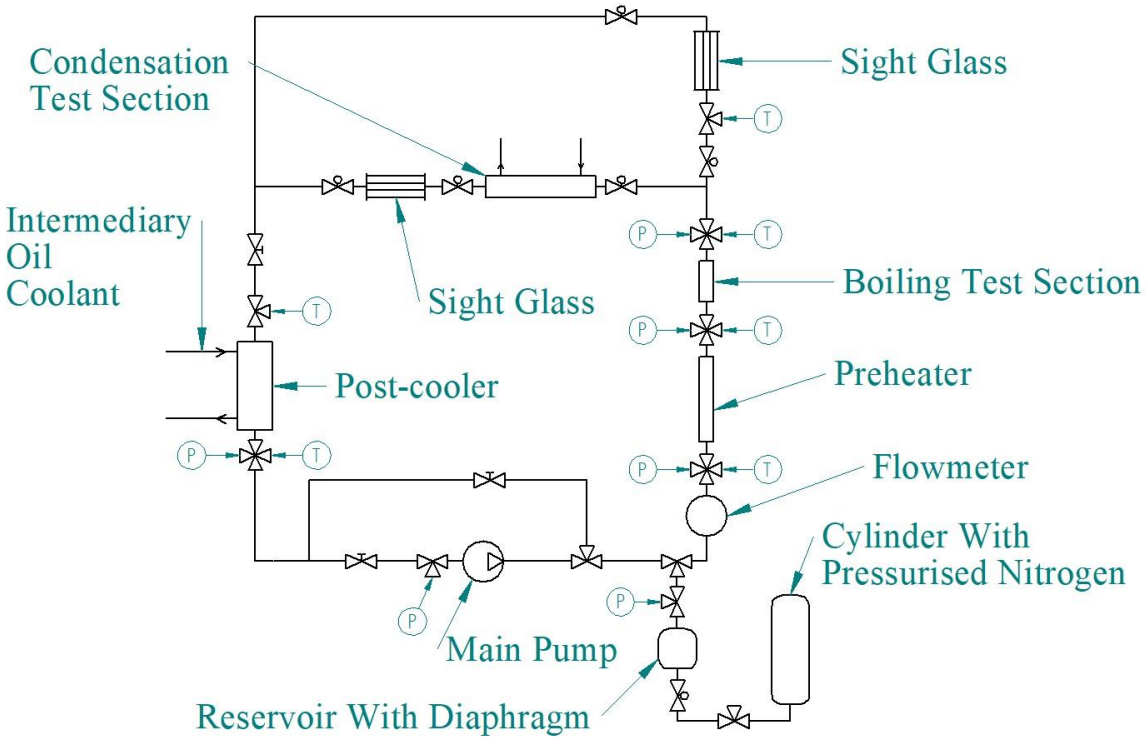

Figure 3.1 Scheme of laboratory test rig

In the experimental rig, pressure is generated by pressurized nitrogen connected to a hydraulic accumulator with a diaphragm. This setup smooths out pressure spikes from the pump and maintains stable conditions. The pump drives the flow and compensates for pressure losses in the system. The facility can operate over a wide range of mass flows, from 0.2 to 18 g/s, measured by a Coriolis flowmeter. Flowmeter is a sensor type MASS 2100 DI 1.5 with the transmitter MASS 6000 19" IP20. It is two-part kit, intended to measure the flow of any fluid (including erosive and corrosive fluids). In addition to mass flow measurement, the flowmeter allows to measure: volumetric flow, density,

temperature and a percentage content of solid admixtures. The measuring range is from 0 to 30 kg/h at the fluid temperature of -50 to +125°C. Its accuracy is 0.1% of the measured value. The preheater and boiling test section are heated by a direct current power supply with a total output of 2 kW. Both components are electrically insulated with PEEK material inside the connecting flanges. The test section and preheater are well-instrumented and thermally insulated, enabling accurate calculation of refrigerant quality at the outlet of the boiling test section. A condensation test section is installed after the boiling test section. The next component is the post-cooler, which is connected to an intermediary oil rig with a mixing valve regulated by a PIC controller to ensure a stable outlet temperature from the post-cooler. This design helps to maintain stable experimental conditions. Scheme of condensation test section is presented in Figure 3.3. The tank for working fluid is hydraulic accumulator with diaphragm MEAK 1.4-250. It is connected to pressurized nitrogen. The accumulator can operate at the pressure up to 250 bar. Pressure spikes created by the pump are smoothed by this hydraulic accumulator. Hydraulic accumulator also enables to set stable saturation pressure inside the testing rig. Pressure is created by connecting pressurised nitrogen tank by reducer. Main pump is a gear pump Verdergear VGS040. Gear pump enables smooth operation without vibration and pressure spike unlike reciprocating pumps. Thermocouples of K and T type are used for temperature measurements. Temperature measurement points shown in Figure 3.1 are representing thermocouple K locations where locations of thermocouple T are placed in the condensations measuring part presented in Figure 3.3. Direct current power supply is connected to preheater and boiling test section. It can separately output power up to 1.79 kW for preheater and 1.22 kW for boiling test section, what gives a total power of 3 kW. It allows to precisely achieve required temperature and quality at the inlet of condensation test section. Utilization of boiling test section as an additional preheater was not required during the experiments. Mounted gauge pressure transducers VEGABAR 83 can measure pressure up to 40 bars at 105°C at accuracy 0.075%. Summary of experimental facility instrumentation is presented in Table 3.2. In the modified version the facility is enabling flow boiling and flow condensation experiments. In the present study the case of flow condensation has been scrutinised.

Figure 3.2 Photograph of laboratory testing rig

Table 3.2 Summary of experimental facility instrumentation

Measurment place	Instrumentation	Range	Uncertainty
Preheater	thermocouple K	0-400°C	1.5 K
Test section	thermocouple T	0-350°C	0.5 K
Water cooling loop II	Peltron NXPG16 pressure transducer	0-16 bar	0.1 %
Preheater, Water cooling loop I	Peltron NXPG40 pressure transducer	0-40 bar	0.1 %
Test sections, Cooling loops	Vegabar 83 pressure transducer	0-40 bar	0.075%
Refrigerant main loop	Coriolis MASSFLO 2100	0-30 kg/h	0.1%
Preheater	DC power supply	0.1-17.9 V	0.2%
		0-100 A	0.5%
Boiling test section	DC power supply	0.3-6.1 V	0.2%
		0-200 A	0.5%
Water cooling loop II	Atrato AT710	0,002-0,5 l/min	1%
Water cooling loop I	Atrato AT720	0,01-1,7 l/min	1%

The test section consist of a copper circular tube with an internal diameter of 3 mm and a length of 50 mm. The internal is cooled by two separate cooling loops. The water in the first loop will flow at a high velocity to ensure a high convective heat transfer coefficient on the cooling side and to maintain a low temperature difference (less than 3 °C) between the inlet and outlet of the test section. It is essential that the heat transfer coefficient is higher on the water side for the experiment. The flow in the second cooling loop is be several times smaller to achieve a significant temperature difference, which is necessary for accurately determining the heat duty of the test section, a critical aspect of the experiment. The heat transfer coefficient is calculated based on the recorded value heat flux, condensation thermal resistance. Procedure of calculation of heat transfer coefficient is presented in equations (3.4-3.15). The heat added by the pump and heat loss to environment are accounted for. Measurement methodology is based on Garimella and Bandhauer [19] and Jiang [20] experiments. Jiang used municipal water for cooling of the second cooling loop. In this experiment laboratory ultra-thermostat Julabo F-33 is used for that purpose. Temperature range of Julabo F-33 is ranging from -30°C to 200°C. It enables control of cooling water temperature condensation temperature, which subsequently enables control of condensation heat flux. Scheme of the cooling loops is presented in Figure 3.3. Figure 3.4 present the cross section and photograph of the condensation test section. Dimensions of the test section are presented in Figure 3.5. Outer shell is 3D printed from ABS. ABS (acrylonitrile butadiene styrene) is a common thermoplastic polymer typically used for injection molding and 3D printing applications. This material is widely used because its properties: relatively high structural strength, chemical resistance, relatively high and low temperature resistance and electrical insulation properties. ABS conduction coefficient is equal to 0.14 W/(m·K), what prevent enhancement of heat transfer area by the wall of outer shell.

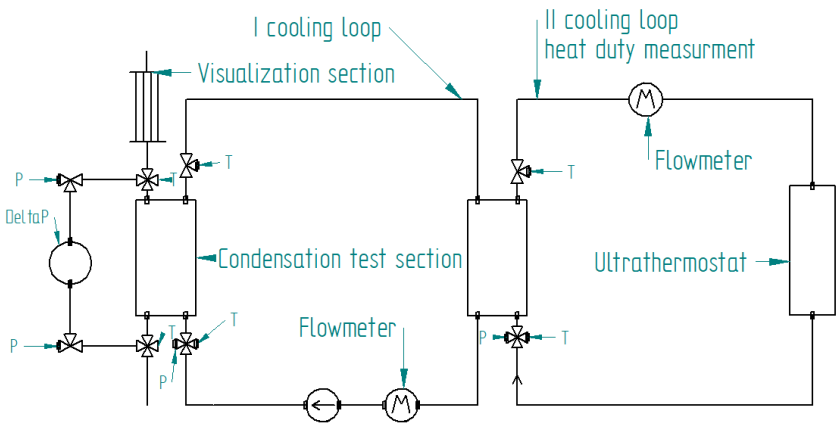

Figure 3.3 Scheme of condensation test section with cooling loops

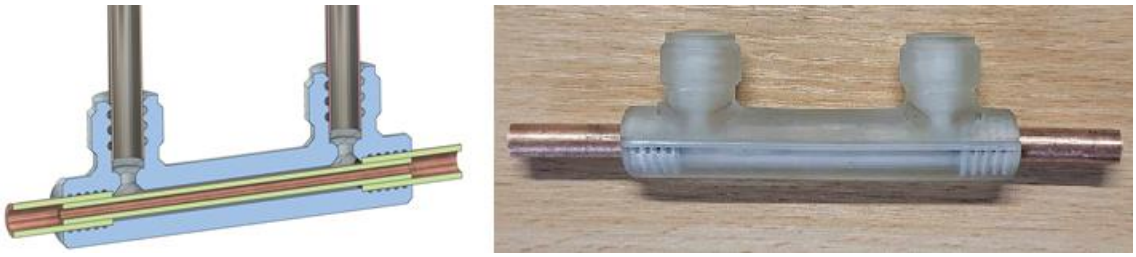

Figure 3.4 Cross section and photograph of condensation test section

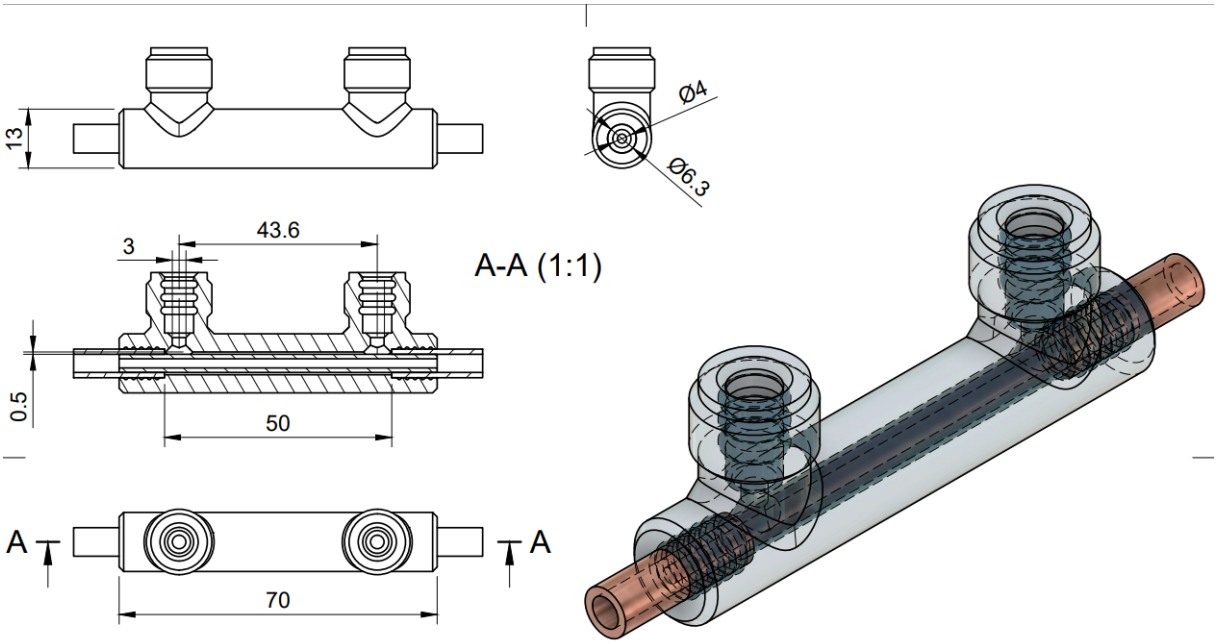

Figure 3.5 Test section dimensions

3.2.1. Wall temperature outside of test section effect on heat transfer

For the sake of information about axial conduction in the test section the preliminary numerical simulation of temperature distribution has been executed. Numerical simulation was conducted in Ansys 2021 Mechanical Steady-State Thermal simulation module. Grid consisted from 445830 elements. Postprocessing procedure takes into account the real wall temperature difference alongside the test section. In standard heat exchanger calculations connectors are not taken into account. In reality connectors work like circular fins. Copper tube could equalize temperature with medium even after 20 or 30 millimetres. The issue of additional heat transfer has been carefully examined numerically. Case when cooling water has 35 °C, and cooled liquid single-phase refrigerant has 60 °C is presented in Figure 3.6. Blue area is cooled from outside by the flowing water. Water heat transfer coefficient in this place is 28454 W/(m^2·K) (calculated by the formula from Garimella and Christiensen [79]). Refrigerant is flowing inside the tube and its heat transfer coefficient is 2264 W/(m^2·K) (calculated by Gnielinski (2013) model [80]) and mass flow was 4.29 g/s. Green and red area is outside of test section where wall temperature is starting to rise. Fin effect could increase heat duty of test section even by 20%. To account for this effect calculation of “fin” conduction through pipe has been derived from differential conduction equation and added to post processing procedure. Forula is presented in equation (3.3). This case is similar to the “infinite fin” and “finite fin” presented in heat transfer coursebooks [81,82]. To accurately calculate this effect experiment for measurement of copper tube conduction has been executed. This experiment is presented in the Appendix 4. Author did not find work which incorporated this effect into calculation procedure. Most experiments have larger heat transfer area where fin effect has negligible effect, but in some cases it could affect results. Experiments which utilise wall temperature measurement are less prone to this. To clarify, numerical simulation was utilised for identification of effect of axial conduction on heat duty of the test section, but numerical simulation is not part of postprocessing procedure.

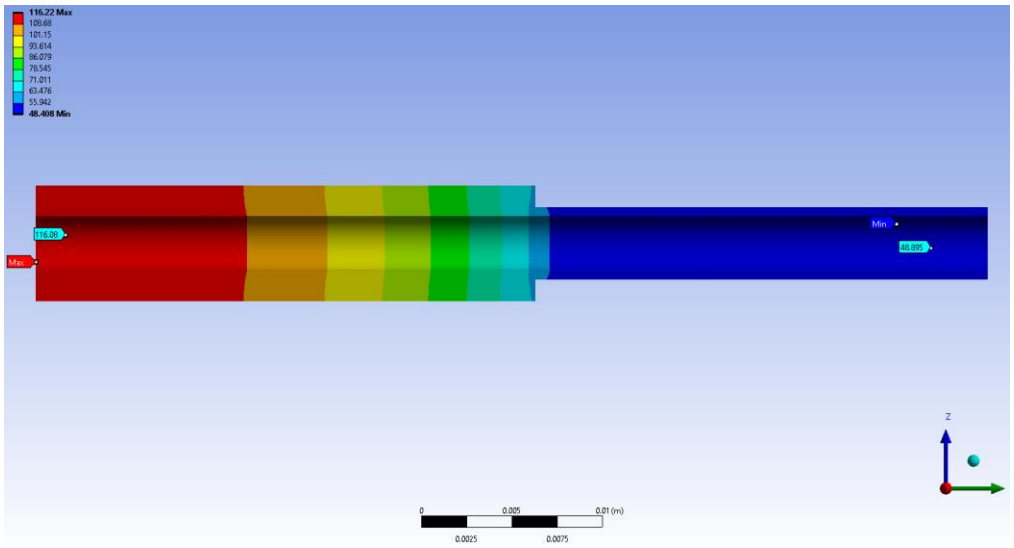

Figure 3.6 Temperature distribution alongside test section tube.

3.2.2. Test section quality

Average quality inside test section was calculated from heat balance. From heat transferred to refrigerant value of liquid enthalpy for saturation temperature and half of heat transferred to cooling water as in equations (3.1) and (3.2)

$$x_{avg} = \frac{Q_h - H_l - \frac{Q_{loopI}}{2}}{H_{lv}} \quad (3.1)$$

$$Q_h = Q_{pre} * \eta \quad (3.2)$$

x_{avg}- average quality inside test section

Q_h-heat transferred to refrigerant in preheater

Q_{loopI}-heat transferred to cooling water in loop I

Q_{pre}-electric power delivered to of preheater

η- efficiency of preheater measured for each saturation temperature during one phase tests.

3.2.1.3 Wall heat addition – "fin effect"

Equation (3.3) for heat transfer between refrigerant and wall outside of the test section was derived from Fourier conduction equation. This case is nearly identical to infinite fin case presented in heat transfer coursebooks [81].

$$Q_{wall,inlet} = \frac{\alpha_c \cdot p_{per} \cdot \lambda_{wall} \cdot A_{cross-section}}{T_{sat,inlet} - T_{wall,inlet}} \quad (3.3)$$

p_{per}-perimeter

$A_{cross-section}$-area of tube cross section

α_c-condensation heat transfer coefficient

T_{wall}- wall temperature

3.2.3. Heat transfer coefficient calculation

Experimental heat transfer coefficient is calculated from overall heat transfer inside test section and Thermal resistance of each component: water, wall and refrigerant resistances. Overall resistance was designated experimentally. Wall resistance and water resistance were calculated as in equations (3.5) and (3.6). Refrigerant resistance was calculated as in equation (3.13) Experimental heat transfer coefficient was then calculated from equation (3.14).

$$R_{total} = R_{water} + R_{wall} + R_{refrigerant} \quad (3.4)$$

$$R_{water} = \frac{1}{\alpha_l \cdot \pi \cdot d \cdot l_s} \quad (3.5)$$

$$R_{refrigerant} = \frac{1}{\alpha_{exp} \cdot \pi \cdot d \cdot l_s} \quad (3.6)$$

$$R_{wall} = ln(\frac{d_{outer}}{d_{inner}}) \cdot 2 \cdot \pi \cdot \lambda_{wall} \cdot l_s \quad (3.7)$$

$$R_{total} = \frac{1}{UA} \quad (3.8)$$

$$dT_a = t_{water,inlet} - t_{refrigerant,inlet} \quad (3.9)$$

$$dT_b = t_{water,outlet} - t_{refrigerant,outlet} \quad (3.10)$$

$$LMTD = \frac{dta - dtb}{ln(\frac{dta}{dtb})} \quad (3.11)$$

$$UA = \frac{Q_{loopI}}{LMTD} \quad (3.12)$$

$$R_{refrigerant} = R_{total} - R_{wall} - R_{water} \quad (3.13)$$

$$\alpha_{exp} = \frac{1}{R_{refrigernat} \cdot \pi \cdot d \cdot l_s} \quad (3.14)$$

3.3. Commissioning tests of the test facility

Every newly constructed test facility should be rigorously tested. Firstly test rig was tested with pressurized nitrogen with small addition of refrigerant SES36 to determine potential leaks. Refrigerant leak detector has been used to find leaks. After tightening and adjusting seals all apparatus have been checked. Next step was conduction of measurements of Loop I energy balance and test section energy balance. After that heat transfer coefficient measurement method was validated during single phase liquid flow test.

3.3.1.1 Data collecting and processing

The data acquisition system is based on the National Instruments interface PXIe-1071. It offers 32 inputs for thermocouples (PXIe-4353 module) and 32 current inputs 4 - 20 mA (TB-4302C module). LabVIEW has been utilised for data collection. Figure 3.7 present the LabVIEW front view of data acquisition programme. Raw data was post processed in EES Engineering Equation Solver [84].

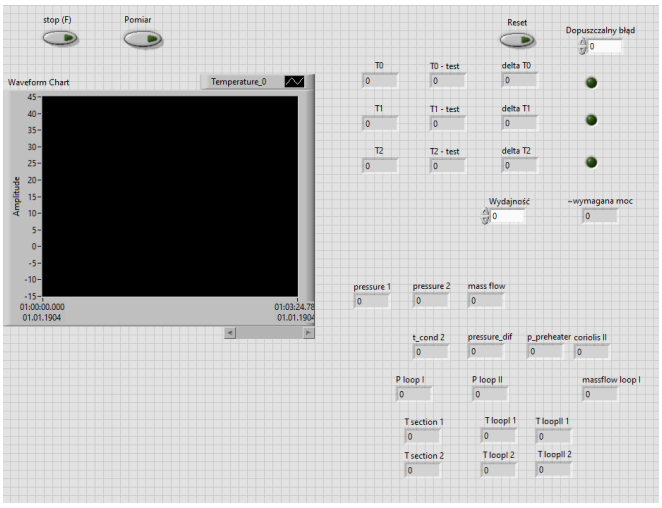

Figure 3.7 LabVIEW front view of data acquisition programme

Post processing code is presented in the Appendix 2. Experimental data is presented in the Appendix 1.

3.3.1.2 Single phase flow validation

Prior to proper condensation experiments experimental procedure has been validated during single phase measurements. Results are presented in Figure 3.8. Experimental refrigerant single phase heat transfer coefficient has been compared with Gnielinski (2013) [80] correlation as well as Taler and Taler (2017) [83] correlation. Mean absolute percentage error MAPE for Gnielinski correlation is 6.45%, whereas MAPE for Taler and Taler correlation is 4.24%.

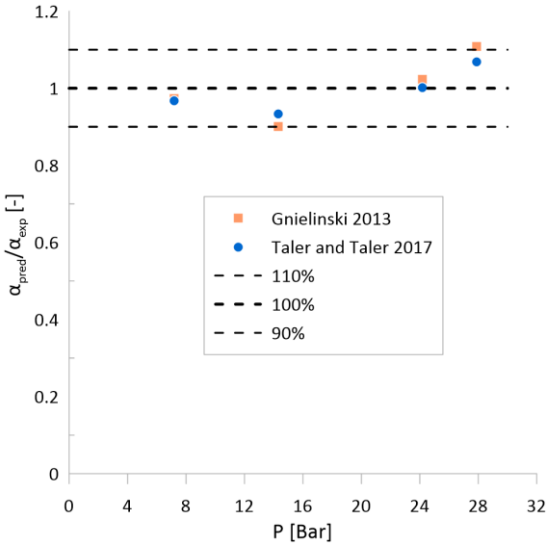

Figure 3.8 Results of single phase heat transfer validation for different pressures.

3.3.1.3 Loop I energy balance

Loop I is presented in Figure 3.3. Temperature inside this loop can be adjusted by laboratory ultrathermosat Julabo F-33 described earlier. Heat loses to ambient from loop I are dependant from temperature. Circulation pump transfers heat into loop, which is generated by pressure drop. Heat loses and heat pump addition have been measured for different temperatures of cooling loop I. This measurements were later used to interpolate heat addition into loop I for each measurement point. Measurements are presented in the Table 3.3.

Table 3.3 Pump head addition and heat loos from loop I for difference between ambient temperature and loop internal water temperature.

Q [W]	dt [°C}
10.62	-1.443
9.367	0.6746
7.666	4.854
3.692	9.977
2.806	17.81
2.532	28.58
-3.948	37.32

3.3.1.4 Test section energy balance

During the single phase test the heat duty was calculated form the cooling water side Q_{wat} on the second loop and from the refrigerant side Q_{ref}. Average difference between Q_{wat} and Q_{ref} was 5.30%. This test was performed to validate thermal amplification technique proposed by Bandhauer et al. [19]. Results of the test section balance are presented in table. Percentage value was calculated as $\frac{Q_{wat}-Q_{ref}}{Q_{ref}}$.

Table 3.4 Test section balance

Qref	Qwat	Difference	Percentage value
60.15	57.18	2.97	4.94%
73.08	78.44	-5.36	-7.33%
79.76	77.48	2.28	2.86%
73.09	64.79	8.3	11.36%

3.3.1.5 Experimental challenges at high saturation temperature

Exaction of experiment at high saturation temperature and high saturation pressure simultaneously is related to multiple challenges. Firstly all tubes, fitting, connections and apparatus have to withstand

experiment conditions. One of the biggest problems is sealant applications in form of O-rings, PTFE type and gaskets. While polytetrafluoroethylene (PTFE) and other popular sealant materials such as nitrile rubber (NBR) are stable at low temperatures such as 40°C they tend to degrade quickly at temperatures above 100 °C. Solder and high temperature thread glue are preferable means of sealant but they are not suitable in all cases. Preheater has to be electrically separated from the rest of apparatus. For this purpose PEEK flanges and PTFE O-rings were used. Visualization test sections was constructed with use of carbon enriched PTFE seals for increased temperature durability. Testing rig had to be checked for new potential leakages. During experimental campaign a few seals had to be replaced and threads had to be retightened. Thermal expansion of tubes also has to be taken into account. Visualization test section had to be monitored because glass tubes are prone to cracking and breaking under stress. Many elements such as condensation test section had to be designed and manufactured from high quality materials. Custom made elements are preheater, boiling test section, condensation test section and visualization test section. There are two commonly used methods of stabilization pressure in testing rig. One use heated refrigerant tanks which is heated up to desired saturation temperature. Second is refrigerant tank with diaphragm connected to pressurised nitrogen. First method is challenging at high saturation temperature because it would require high temperature thermostat and refrigerant tank which could safely sustain temperatures above 100°C at high pressure. Second method require high pressure rated diaphragm tank. Furthermore all heat loses need to be carefully examined, measured and calculated, because their effect is usually higher at high saturation temperatures. Important factor is safety of experiment. Poorly designed or inadequately constructed laboratory testing stand could result in operator injury or valuable equipment damage when internal examined fluid parameters reach up to 150°C and 30.

3.4. Uncertainty analysis

Uncertainty analyses were conducted using the EES [84] uncertainty propagation function. Methodology is based on assumption that individual measurements are uncorrelated and random Taylor and Kuyatt [85]. Uncertainties for each measurement are presented in Table A1.1 in the Appendix 1. Uncertainties were calculated for heat transfer coefficient, quality, heat flux, and difference between wall temperature and fluid temperature. Average uncertainty for heat transfer coefficient for all measurements is 13.13%. Minimal uncertainty for one measurement point is 9.74% and maximal is 22.85%. Table 3.5 presents average percentage value of uncertainty for mass velocity G, quality x, experimental heat transfer coefficient α_{exp}, heat flux q and difference between refrigerant saturation temperature and wall temperature ΔT.

$$U_y = \sqrt{\sum_i \left(\frac{\partial Y}{\partial X_i}\right)^2 U_{xi}^2}$$

Table 3.5 Average uncertainty values

Parameter	± G	± x	$\pm\alpha_{exp}$	±q	±ΔT
Percentage value	0.67%	2.38%	13.13%	10.77%	0.71%

3.5. Visualization test section

Flow structures are observed in the transparent sight glass. This sight glass was build in-house for the purpose of observation of refrigerant flow structures. Is consists of a circular borosilicate glass tube with internal diameter 3 mm. It is secured inside the stainless steel chassis and sealed by elements made from the coal reinforced PTFE. Sealing allows glass to expand thermally. This sight glass was operating at high saturation temperatures during boiling tests and it is well suited into the considered experiment. Figure 3.9 show the photograph of visualization test section. Fast camera Photron Mini UX100 is utilised for the purpose of flow patterns capture. LED light source with refractor is used as backlight. Drawings of Visualization test section are presented in Figure 3.10 and Figure 3.11.

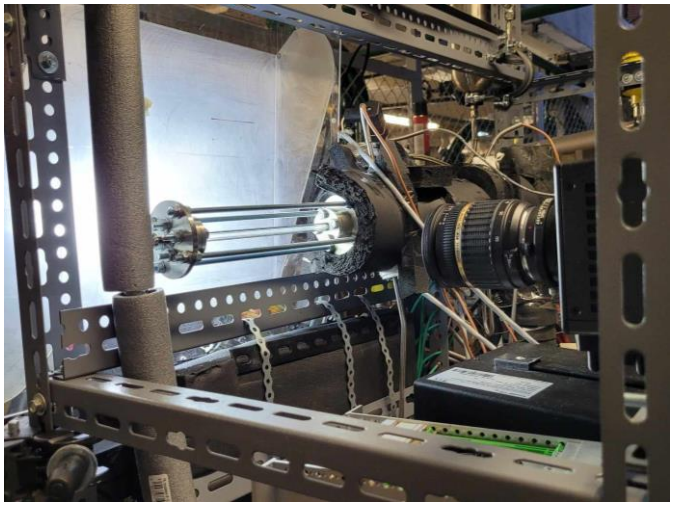

Figure 3.9 Photograph of visualization test section

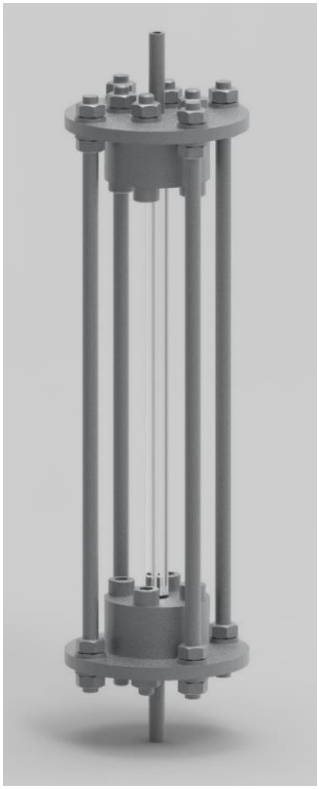

Figure 3.10 Rendered visualization test section

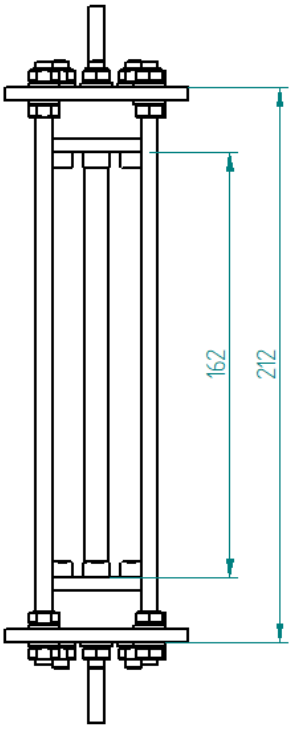

Figure 3.11 Dimensions of visualization test section

3.6. Modification of in-house prediction method for prediction of heat transfer coefficient during condensation

Mikielewicz and Mikielewicz [51] previously developed a semi-empirical method for modelling heat transfer during boiling and condensation in mini-channels. This method is based on the hypothesis that total energy dissipation in two-phase flow with boiling is the sum of energy dissipation from shearing flow and from bubble generation. This general model of boiling and condensation which contrary to most models has theoretical background. The basic hypothesis in the model is the fact that the heat exchange during boiling in flow with bubble generation is modelled as the sum of energy dissipation from convection in two phase flow, ETP, and energy dissipation derived from bubble generation,

$$E_{TPB} = E_{TP} + E_{Pb} \tag{3.15}$$

Energy dissipation under steady state conditions can be approximated by dissipation in the laminar boundary layer that dominates heat transfer and momentum in the process under consideration. Dissipation in flow is expressed as the power lost per unit volume in the two-phase flow in the boundary layer. Power is expressed as the product of the aerodynamic force and velocity. Substituting the appropriate dependencies on the definition of power in the flow leads to the formation of a relationship in the form of the ratio of the square of shear stress to the dynamic viscosity coefficient in the laminar layer.

$$E_{TP} = \frac{\tau_{TP}^2}{\mu_l} = \frac{\xi_{TP}^2 \rho_l^2 w_{TP}^4}{64\mu_l} \tag{3.16}$$

Analogically, energy dissipation due to the generation of bubbles in two-phase flow at a velocity

$$E_{TP} = \frac{\xi_{Pb}^2 \rho_l^2 w_{TP}^4}{64\mu_l} \tag{3.17}$$

The total energy dissipation in two-phase flow with bubble generation reads:

$$E_{TP} = \frac{\xi_{TPB}^2 \rho_l^2 w_{TP}^4}{64\mu_l} \tag{3.18}$$

Substituting (2-4) to (1) the geometrical relation between friction coefficients is obtained:

$$\xi_{TPB}^2 = \xi_{TP}^2 + \xi_{Pb}^2 \tag{3.19}$$

By applying the analogy between momentum and heat transfer, the above result can be generalized and the dependence of the heat transfer coefficient on boiling in two-phase flow as a function of simpler heat exchange mechanisms:

$$\alpha_{TPB}^2 = \alpha_{TP}^2 + \alpha_{Pb}^2 \tag{3.20}$$

Expressing the heat transfer coefficient for the two-phase flow with friction in function of the two-phase flow multiplier, $\alpha_{TP}=R_{0.4}\alpha_l$, the final form of the underlying model is obtained:

$$\frac{\alpha_{TPB}}{\alpha_L} = \sqrt{R^{0.8} + \left(\frac{\alpha_{PB}}{\alpha_L}\right)^2} \tag{3.21}$$

Mentor developed that formulation to a more advanced formulation for the saturated flow boiling,

$$\frac{\alpha_{TPB}}{\alpha_L} = \sqrt{R_{MS}^n + \frac{C}{1+P}\left(\frac{\alpha_{PB}}{\alpha_L}\right)^2} \tag{3.22}$$

Using this method of determining the heat transfer coefficient requires the choice of the appropriate two phase flow multiplier R and the relevant relation describing the heat transfer coefficient for pool boiling, α_{Pb}. Constant C = 1 for boiling in flow and C = 0 for condensation in flow. Correction P is a multi-parameter function and the result of multiple regression matching the experimental data. In condensation, bubble generation dissipation is absent. The main equation includes terms for resistance in two-phase flow and for flow resistance from nucleation during boiling. The modified equation in this paper focuses solely on flow resistance, as it addresses heat transfer modelling during condensation. The flow resistance term is modelled using the modified Muller-Steinhagen and Heck correlation [54], with α_{LO} representing the heat transfer coefficient for single-phase liquid flow, and α_{TPB} representing the heat transfer coefficient during condensation, which will be denoted later as α_{TPC}. Standard Dittus-

Boelter correlation for predicting forced internal convection in single liquid phase heat transfer is recommended.

This work introduces the confinement number (Con), into the two-phase flow multiplier R_{MS}. The flow resistance part is multiplied by the Confinement number raised to the power of $S = 0.1 + 0.28 \cdot p_r$. The Confinement number, described in equation (3.27), accounts for changes in flow nature at high reduced pressures and includes gas and liquid phase densities, surface tension, diameter, and gravitational acceleration. This modification addresses changes in physical properties affecting heat transfer at high reduced pressures.

Experimental research [18] has shown that surface tension and density differences significantly impact two-phase flow structures. At a reduced pressure of 0.2, where surface tension and phase density differences are high, annular flow was observed at as low as 7% quality. At a reduced pressure of 0.8, near the critical point, annular flow occurred around 50% quality. Surface tension and phase density differences decrease significantly at high reduced pressures. The form of a modified in-house model presented in the present work reads:

$$\frac{\alpha_{TPC}}{\alpha_{LO}} = \sqrt{R_{MS}^{n} \cdot Con^{S}} \tag{3.23}$$

n=0.76 for turbulent flow and n=2 for laminar flow

$$S = 0.1 + 0.28 \cdot p_r \tag{3.24}$$

$$R_{MS} = \left[1 + 2\left(\frac{1}{f_1} - 1\right) x Con^{m}\right] \cdot (1 - x)^{1/3} + x^{3} \frac{1}{f_{1z}} \tag{3.25}$$

$$Con = \frac{\sqrt[2]{\frac{\sigma}{g(\rho_l - \rho_v)}}}{d} \tag{3.26}$$

$$turbulent\ flow: \quad f_1 = \frac{\left(\frac{\rho_l}{\rho_v}\right)}{\left(\frac{\mu_l}{\mu_v}\right)^{0.25}} \quad f_{1z} = \frac{\left(\frac{\mu_v}{\mu_l}\right)}{\left(\frac{\lambda_l}{\lambda_v}\right)^{1.5}} * \left(\frac{c_{pl}}{c_{pv}}\right) \tag{3.27}$$

$$Laminar\ flow: f_1 = \frac{\frac{\rho_l}{\rho_v}}{\frac{\mu_l}{\mu_v}} \quad f_{1z} = \left(\frac{\lambda_v}{\lambda_l}\right) \tag{3.28}$$

This is general model for prediction of heat transfer coefficient during flow condensation for conventional and minichannels for whole range of reduced pressures. Model have been tested on consolidated database presented in Table 2.1. Results of modelling are presented in subsequent chapter.

4. EXPERIMENTAL RESULTS

Main goal of experimental research was to determine effect of parameters in the vicinity of thermodynamical critical point on condensation heat transfer coefficient. Studies of Charnay et al. [86] and Pysz et al. [70] have shown that during two phase boiling nucleation effect is dominant in heat transfer phenomenon, although during condensation only convective heat transfer occurs. Studies of Jiang et al. [33] and Zhuang et al. [28] on condensation at high reduced pressures have shown that convective heat transfer tend to decrease at high saturation pressures. Studies of condensation heat transfer at high reduced pressures are limited. None was performed for new eco-friendly hydrofluoroolefin refrigerants. Although tests were performed for reduced pressures up to 0.9 no data was collected for refrigerant condensation above 100°C. Current research focused on identification and quantification of effect of reduced pressure on heat transfer coefficient in new refrigerant at high reduced pressure. Firstly two measurements series were conducted for reduced pressure 0.2 which correspond to saturation temperature 83°C and saturation pressure 7 bar. At this pressure HTC for two mass velocities was measured, namely G=600 [kg/(m²·s)] and G=1000 [kg/(m²·s)]. High pressure drop on G=1000 [kg/(m²·s)] limited the measurement range. It was decided to continue measurements firstly at G=600 [kg/(m²·s)] for varying value of saturation pressure. Subsequent tests were performed for p_r=0.4, p_r=0.6, p_r=0.7 and p_r=0.8. Saturation temperature for p_r=0.8 is 152°C and saturation pressure is 28.3 bar. Range of experiment is presented in Table 4.1.

Table 4.1 Range of experiment

Measured value	Mass velocity G	Quality	Saturation Temperature	Saturation Pressure	Reduced Pressure	Heat Transfer Coefficient	Heat Flux
Unit	G [kg/(m²·s)]	x [-]	T_{sat} [°C]	p_{sat} [bar]	p_r [-]	α [W/(m²·K)]	q [W/(m²)]
Minimum	585.5	0.01988	78.71	6.64	0.186	2068	161.886
Maximum	1003	0.7832	153.2	28.94	0.81	6940	359.787

4.1. Experimental heat transfer coefficient

Experimental results for reduced pressure p_r=0.2 are shown in Figure 4.1. This graph represents the effect of mass velocity on heat transfer coefficient during condensation. The major conclusion from this presentation is that the increase of mass velocity causes increase of heat transfer coefficient at the low value of reduced pressure. Experimental results for mass velocity 600 [kg/(m²·s)] and different values of reduced pressure are shown in Figure 4.2. This graph represents the effect of saturation pressure on heat transfer coefficient during condensation. Increase of saturation pressure causes the decrease of heat transfer coefficient during flow condensation. Value of saturation temperature for reduced pressure p_r=0.2 for R1233zd(E) is 82 °C and saturation temperature for reduced pressure 0.8 is 151°C.

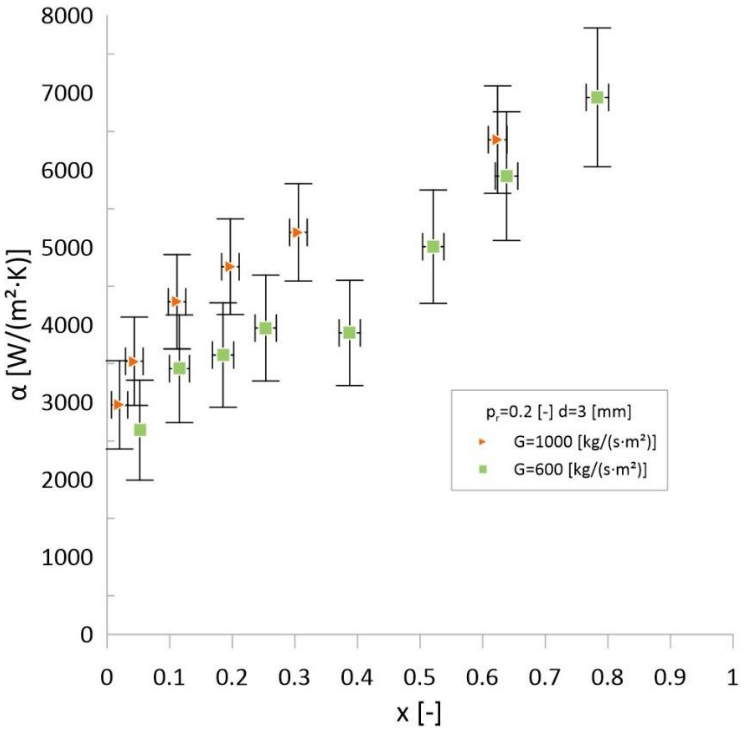

Figure 4.1 Condensation heat transfer coefficients for reduced pressure 0.2

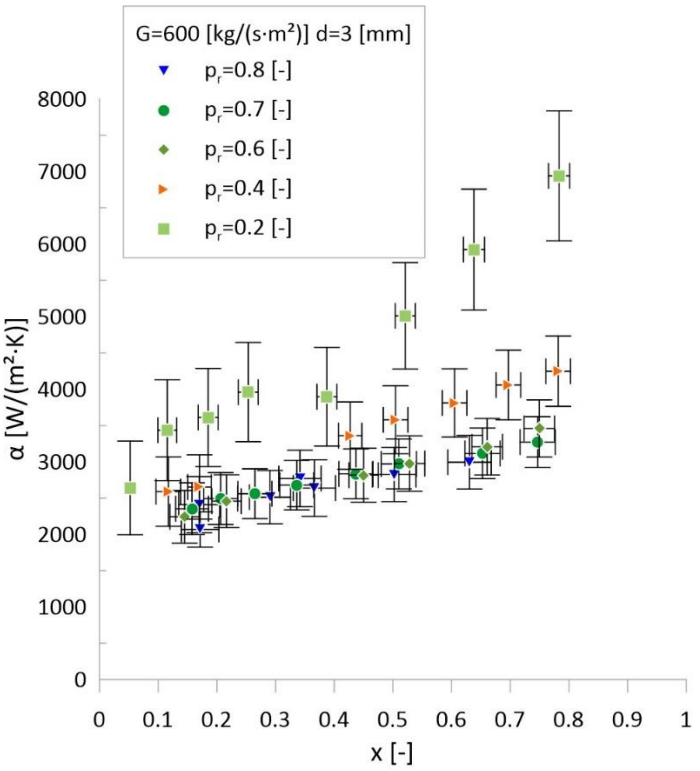

Figure 4.2 Condensation heat transfer coefficients for G=600 [kg/(m²·s)] at varying reduce pressure p_r

Experimental results are compared with a selection of established in literature prediction methods of flow condensation in Figure 4.3, Figure 4.4, Figure 4.5, Figure 4.6 and Figure 4.7. Plots show the effect

of reduced pressure at values of reduced pressure p_r=0.2, 0.4, 0.6, 07 and 0.8. The considered models are presented in the earlier section of the thesis. Modified in-house model is described in the former chapter.

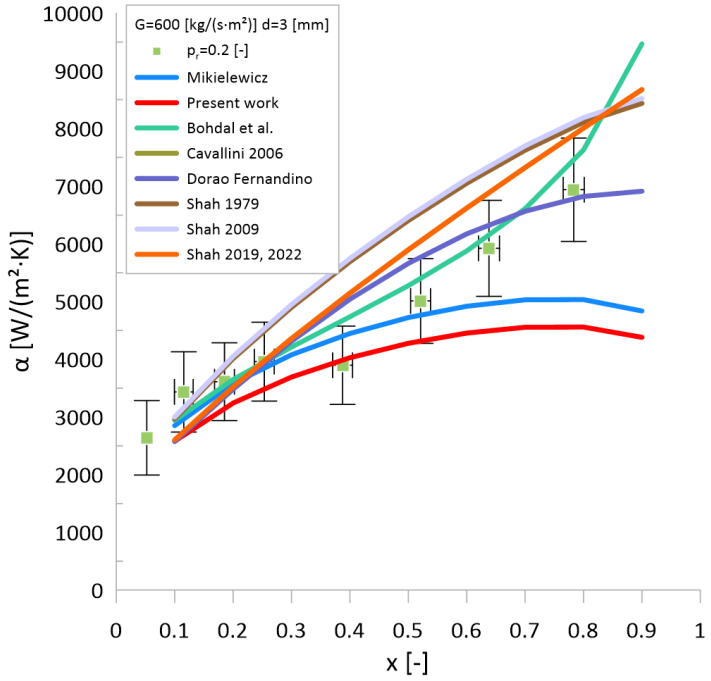

Figure 4.3 Heat transfer Coefficient for G=600 [kg/(m²·s)] p_r=0.2 compared with prediction methods

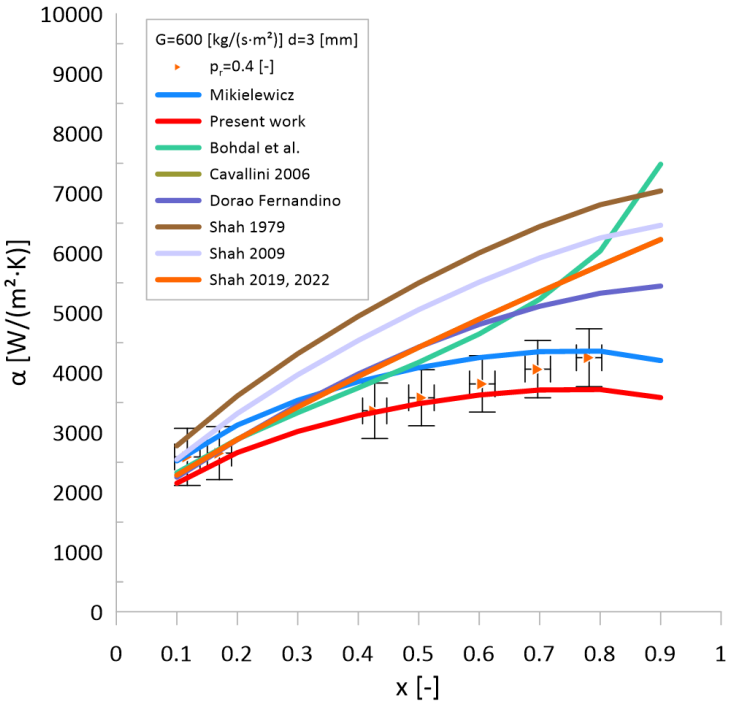

Figure 4.4 Heat transfer coefficient for G=600 [kg/(m²·s)] p_r=0.4 compared with prediction methods

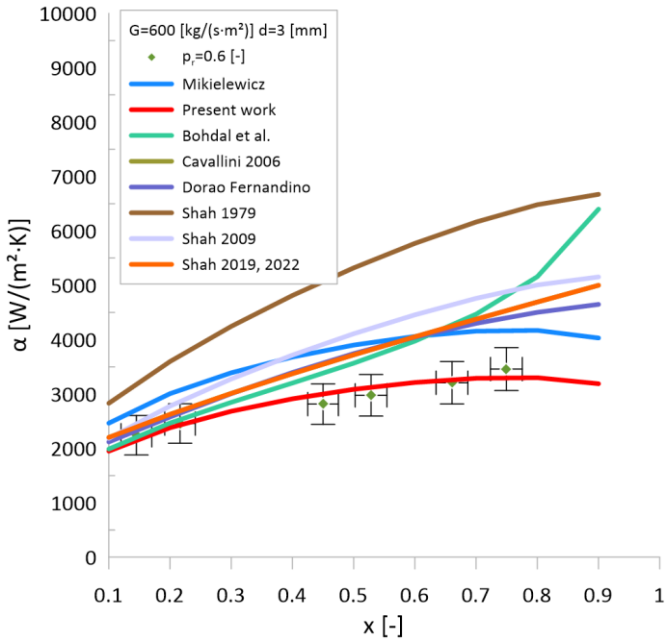

Figure 4.5 Heat transfer coefficient for G=600 [kg/(m²·s)] p_r=0.6 compared with prediction methods

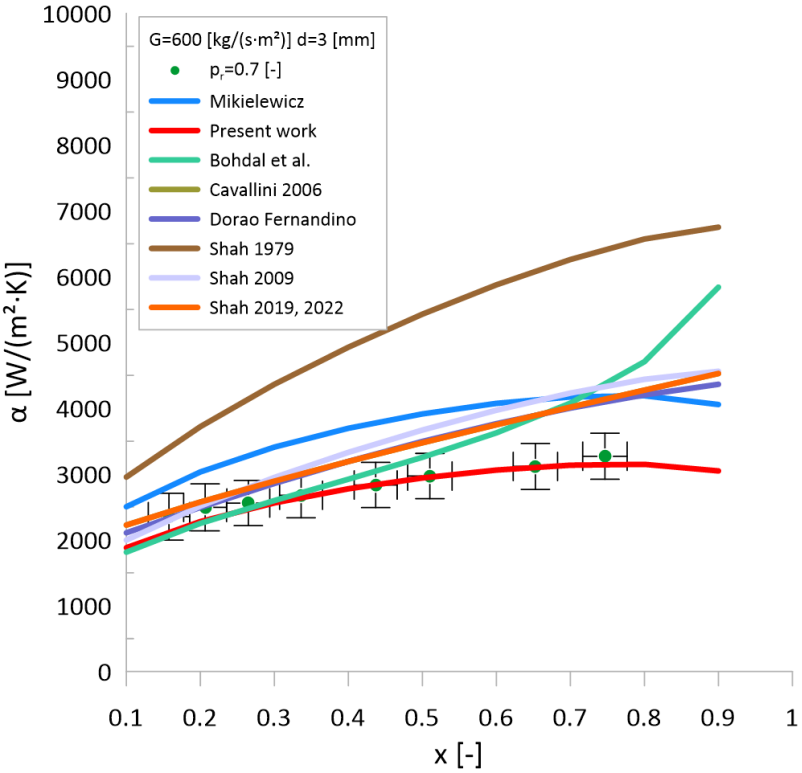

Figure 4.6 Heat transfer coefficient for G=600 [kg/(m²·s)] p_r=0.7 compared with prediction methods

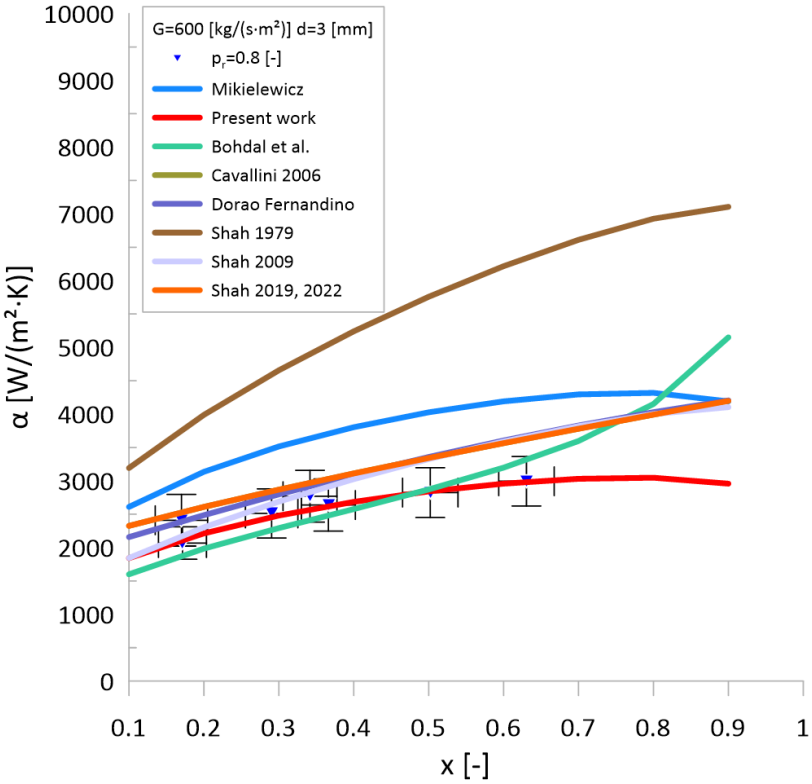

Figure 4.7 Heat transfer coefficient for G=600 [kg/(m²·s)] p_r=0.8 compared with prediction methods

Results of modelling for experimental data is presented in Table 4.2. Figure 4.8 presents a plot comparing authors own experimental data points with predicted values using original Mikielewicz correlation [51]. Figure 4.9 presents graph with modified Mikielewicz correlation presented in equation (4.9), Figure 4.10 presents graph for Bohdal et al. correlation [58], Figure 4.11 presents graph for Cavallini et al.correlation [26] .Figure 4.12 presents graph for Dorao and Fernandino correlation[59], Figure 4.13 presents graph for Shah1979 correlation [55], Figure 4.14 presents graph for Shah2009 correlation [56] and Figure 4.15 presents graph for Shah2019 and Shah 2022 correlation [57,60]. The modified model achieved MAPE 13.71%. The best results of comparison were obtained using a Shah19 model with MAPE=11.02%. Second best correlation is due to Dorao and Fernandino with MAPE=11.36%. The other methods due to Shah and Cavallini achieved slightly worse results. The general form of Mikielewicz model was performing quite well achieving a very good result of MAPE=15.61%, but in comparison with the present study it exhibited a slightly worse consistency than other methods. Average measurement uncertainty for this experiment achieved 13.5%. 7 prediction methods of 9 tested achieved lower value of MAPE than the uncertainty of database. Difference in results between them is small and insignificant. Modified version did not did not achieve the best result for experimental dataset because for R1233zd(E) has relatively low confinement number Con in comparison with other refrigerants. The correlation form is general for all fluids. It can be observed that most correlations known from literature are much better in predictions of heat transfer coefficients at low

value of reduced pressure, than for high pressures, which justifies the activities in the thesis leading to investigating the effects at higher values of reduced pressures.

Table 4.2 Results of modelling for experimental data

Model	MAPE	number of points below <30%	percent o points <30%
Mikielewicz [54]	15.61%	37	88.10%
Present work	13.17%	40	95.24%
Bohdal [58]	12.40%	42	100.00%
Dorao Fernandino [59]	11.36%	42	100.00%
Shah79 [55]	42.58%	15	35.71%
Cavallini2006 [26]	11.73%	41	97.62%
Shah09 [56]	11.73%	41	97.62%
Shah19 [57]	11.02%	40	95.24%
Shah22 [60]	11.02%	40	95.24%

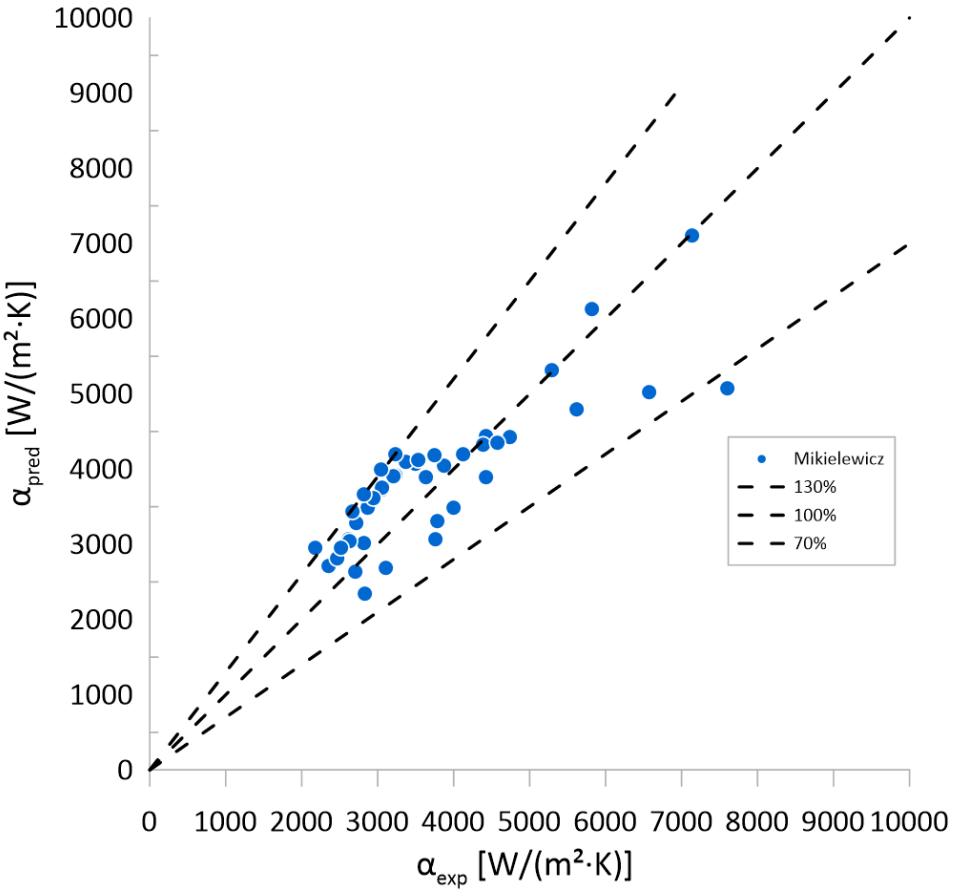

Figure 4.8 Results of modelling with original Mikielewicz correlation

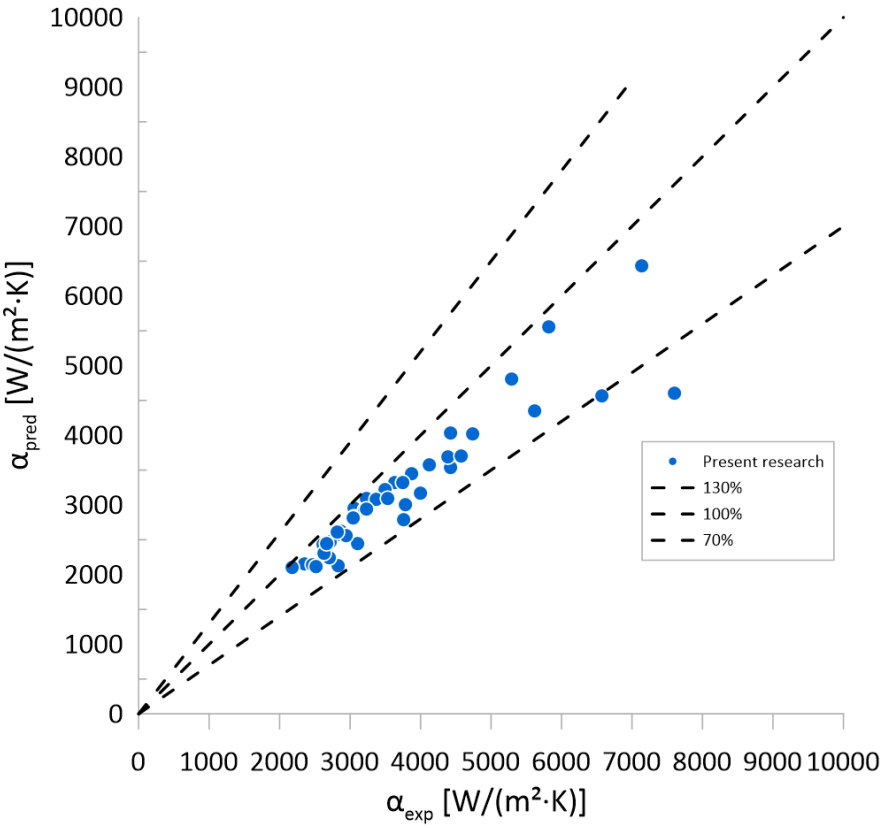

Figure 4.9 Results of modelling with modified Mikielewicz correlation

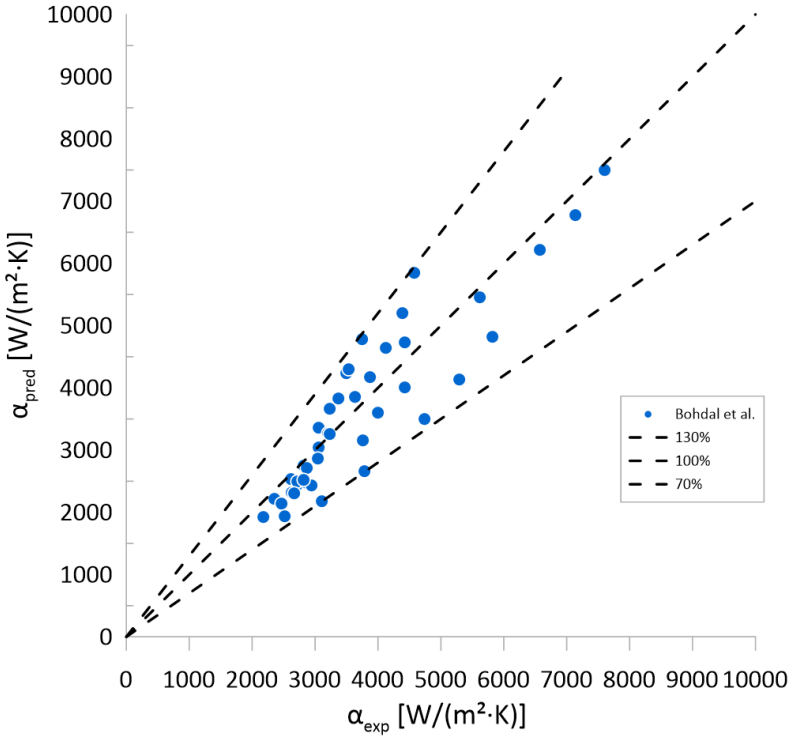

Figure 4.10 Results of modelling with Bohdal et al.[58] correlation

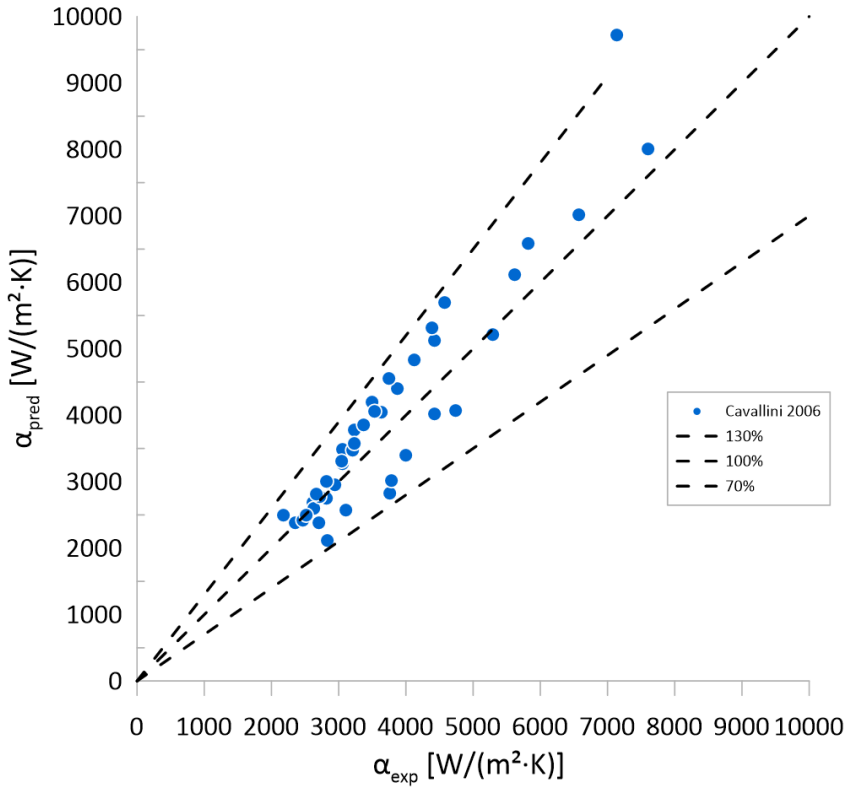

Figure 4.11 Results of modelling with Cavallini et al.[26] correlation

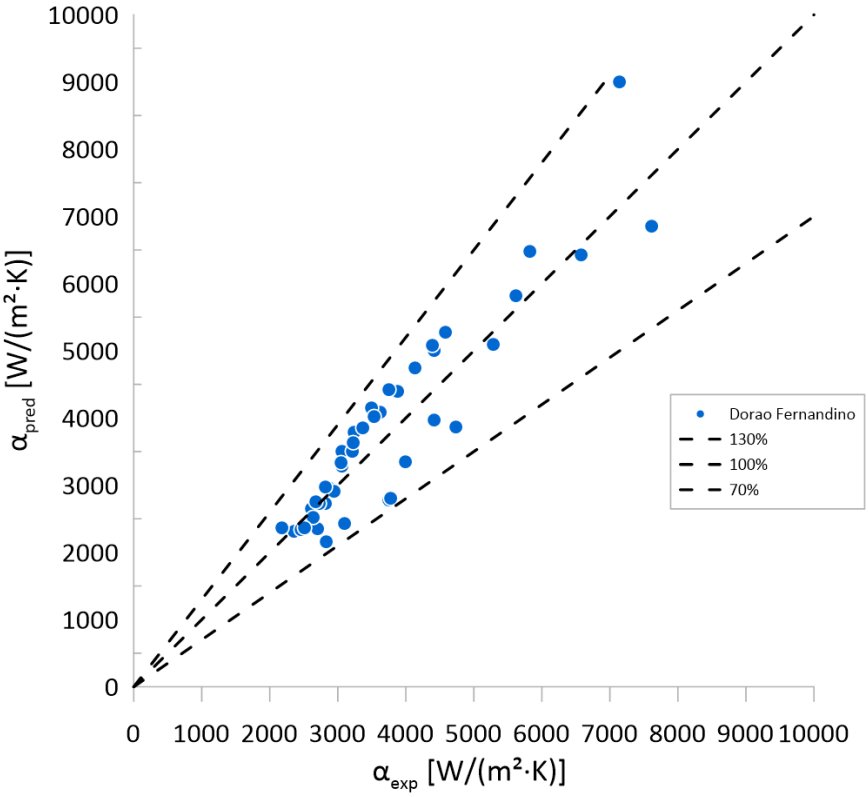

Figure 4.12 Results of modelling with Dorao and Fernandino[59] correlation

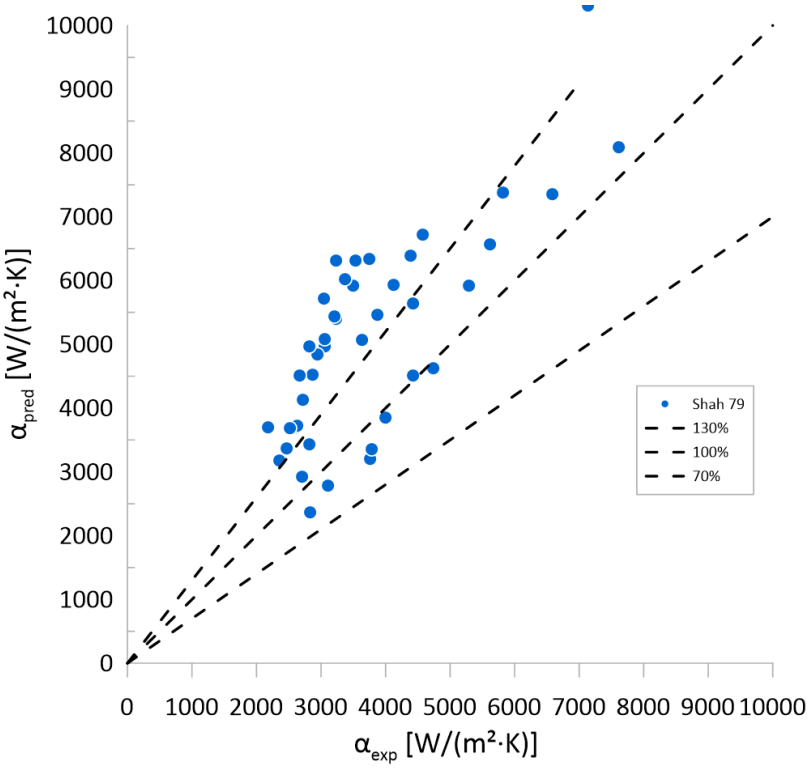

Figure 4.13 Results of modelling with Shah 1979 [55] correlation

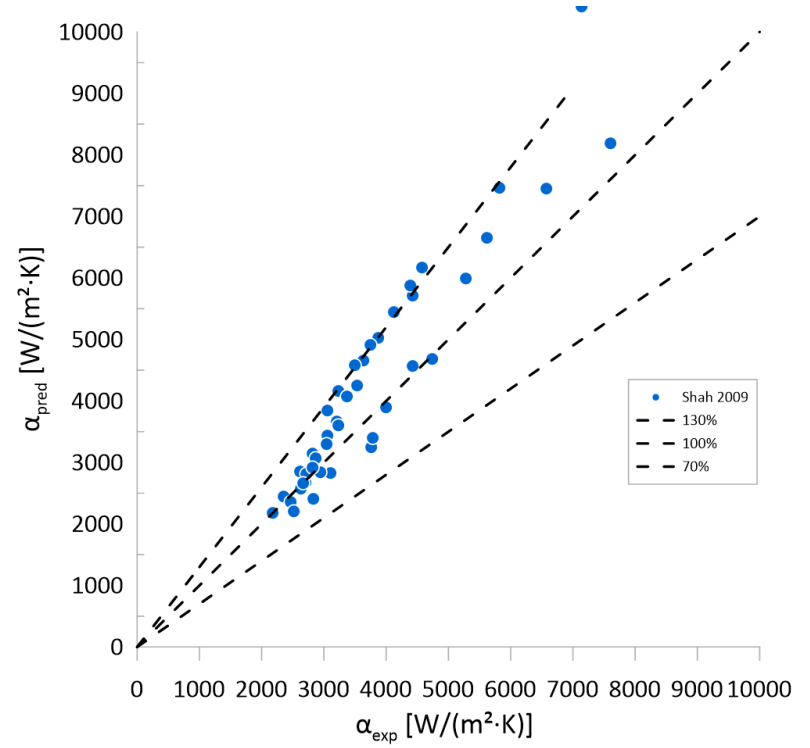

Figure 4.14 Results of modelling with Shah 2009 [56] correlation

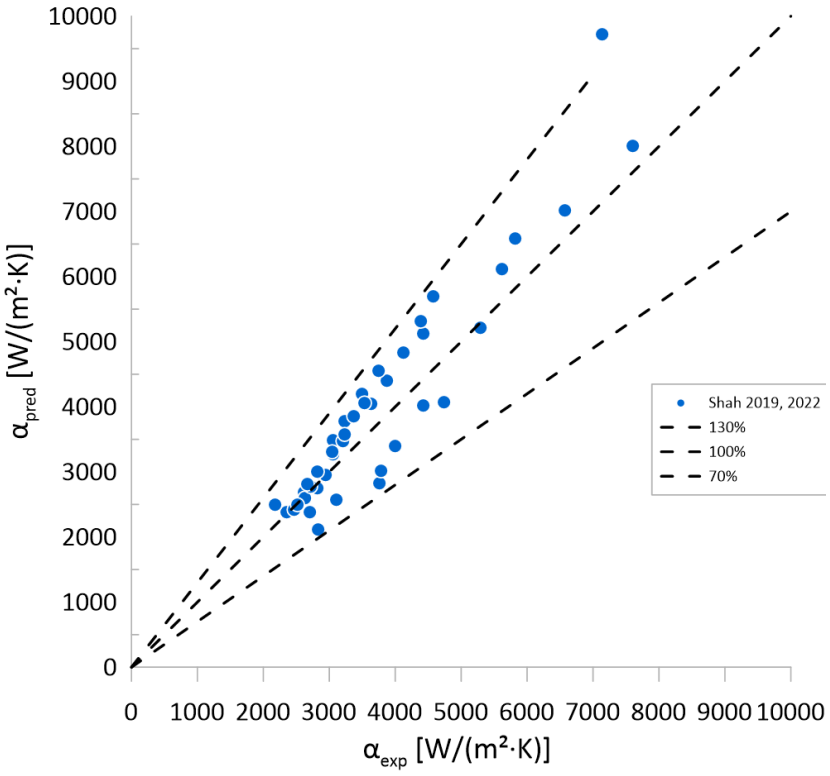

Figure 4.15 Results of modelling with Shah 2019 [87] and Shah 2022 [60] correlation

4.1.1. Results for saturation pressure above 50% of critical pressure

Results of modelling for data at p_r>0.5 are presented in Table 4.3. for increased pressure conditions The best correlation is Dorao and Fernandino with 8.38% MAPE, and second one is due to Cavallini 2006 and Shah 2022 with 8.47%. MAPE. Present work correlation achieved 8.89% MAPE. The difference between these prediction methods is 0.5 of percentage point and their accuracy is nearly identical. Confinement number Con added to original Mikielewicz equation improves results especially at high values of saturation pressure.

Table 4.3 Results of modelling for data above 50% value of reduced pressure

Model	MAPE	number of points below <30%	percent o points <30%
Mikielewicz [54]	21.66%	17	80.95%
Present work	8.89%	21	100.00%
Bohdal [58]	11.48%	21	100.00%
Dorao Fernandino [59]	8.38%	21	100.00%
Shah79 [55]	63.54%	0	0.00%
Cavallini2006 [26]	8.47%	21	100.00%
Shah09 [56]	12.18%	21	100.00%
Shah19 [57]	8.47%	21	100.00%
Shah22[60]	8.47%	21	100.00%

4.1.2. Results for saturation pressure below 50% of critical pressure

Results of modelling for data at p_r<0.5 are presented in Table 4.4 for increased pressure conditions The best correlation in this region is original Mikielewicz correlation with 9.57% MAPE, and second one is Bohdal et al. with 13.32%. The third best is Dorao and Fernandino with 14.33% MAPE. In this particular case most methods underpredict experimental heat transfer coefficient at low values of reduced pressure. Their performance is however better in the region with higher values of reduced pressure.

Table 4.4 Results of modelling for data below 50% value of reduced pressure

Model	MAPE	number of points below <30%	percent o points <30%
Mikielewicz [54]	9.57%	20	95.24%
Present work	17.45%	19	90.48%
Bohdal [58]	13.32%	21	100.00%
Dorao Fernandino [59]	14.33%	21	100.00%
Shah79 [55]	21.61%	15	71.43%
Cavallini2006 [26]	15.00%	20	95.24%
Shah09 [56]	18.21%	20	95.24%
Shah19 [57]	15.00%	20	95.24%
Shah22[60]	15.00%	20	95.24%

4.2. Experimental flow patterns and flow map

Experimental flow maps for horizontal flows in 3 mm channel are presented in this section. Figure 4.16 present results for the reduced pressure p_r=0.2 and two mass velocities whereas Figure 4.17 present the flow map for mass velocity G=600 [kg/(m^2·s)] and reduced pressure ranging from p_r=0.2 to p_r=0.8. It can be observed that annular flow occurs at lower values of quality for higher values of mass velocity. Annular flow occurs at higher values of quality for higher values of reduced pressure. Bubbly flow occurs only at very low quality. Flow patterns prediction methods are presented in the chapter 7.

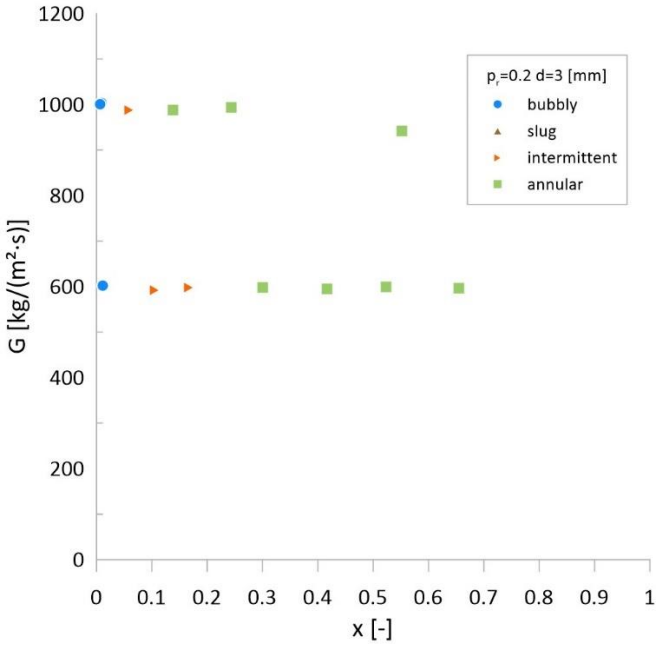

Figure 4.16 Experimental flow map for reduced pressure p_r=0.2 for R1233zd(E)

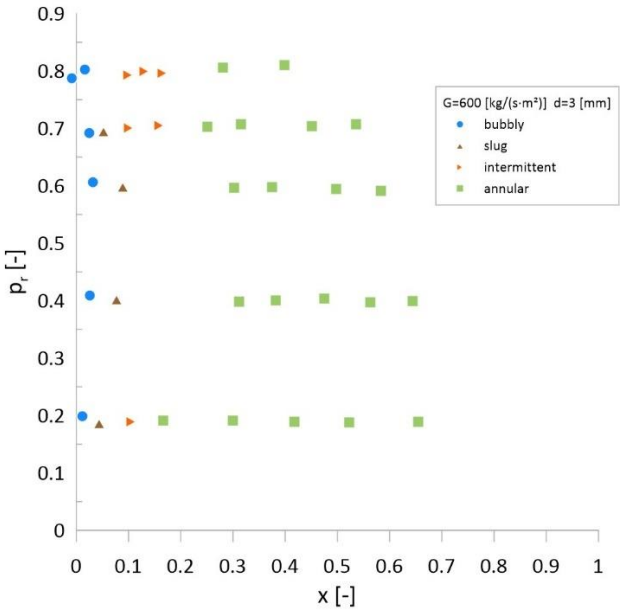

Figure 4.17 Experimental flow map for mass velocity G=600 [kg/(m2·s)] and reduced pressure ranging from p_r=0.2 to p_r=0.8 for R1233zd(E)

Flow patterns were captured during horizontal flow inside 3 mm inner diameter borosilicate tube after condensation test section. Tests were performed at reduced pressures p_r ranging from 0.2 to 0.8 with mass velocities of 600 and 1000 kg/(m²·s). Examples of flow patterns can be observed in Figures 4.18-4.23. Changes in flow patterns with varying values of reduced pressures can be observed. Bubbles for high reduced pressures have significantly smaller diameters. Wavy-stratified flow for high reduced pressures is much more wavy and disturbed. Liquid occupies much more space at low reduced

pressures for wavy-stratified flow. For very high reduced pressures (0.7 and 0.8) small bubbles are present in liquid in wavy-stratified flow. Annular flow is similar for the whole range of reduced pressure.

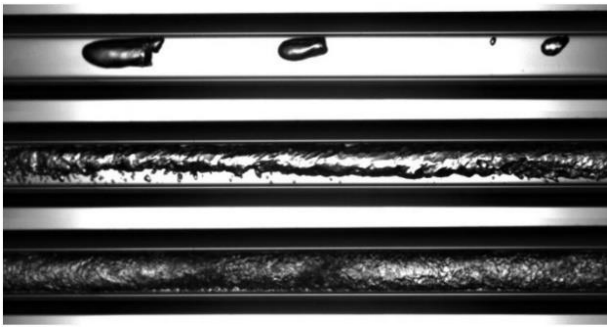

Figure 4.18 Flow patterns of R1233zd(E) in 3mm horizontal pipe under saturation temperature 83°C, saturation pressure 0.71 MPa, reduced pressure p_r=0.2, and mass velocity G=1000 kg/(m²s). Quality respectively: 0.67% 5.9% 24.3%

In Figure 4.18 bubbly flow, wavy-stratified and annular flow can be observed.

Figure 4.19 Flow patterns p_r=0.2 G=600 kg/(m2·s) Quality respectively: 1.13% 10.47% 30.02%

In Figure 4.19 bubbly flow, wavy-stratified and annular flow can be observed.

Figure 4.20 Flow patterns p_r=0.4 G=600 kg/(m2·s) Quality respectively: 2.54% 31.11% 38.15%

In Figure 4.20 bubbly flow, wavy-stratified and annular flow can be observed.

Figure 4.21 Flow patterns p_r=0.6 G=600 kg/(m2·s) Quality respectively: 3.17% 8.91% 30.23% 49.73%

In Figure 4.21 bubbly flow, wavy-stratified and annular flow can be observed.

Figure 4.22 Flow patterns p_r=0.7 G=600 kg/(m2·s) Quality respectively: 2.45% 15.86% 45.10%.

In Figure 4.22 bubbly flow, wavy-stratified and annular flow can be observed.

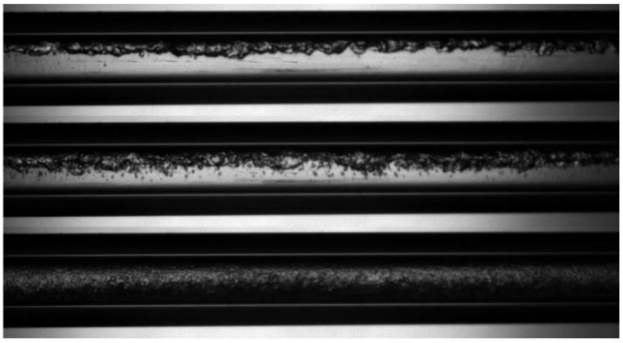

Figure 4.23 Flow patterns p_r=0.8 G=600 kg/(m2·s) Quality respectively: 1.65% 10.74% 97.10%.

In Figure 4.23 bubbly flow, wavy-stratified and annular flow can be observed.

5. FLOW CONDENSATION MODELLING RESULTS BY CONVENTIONAL METHODS

This chapter presents results of modelling of condensation heat transfer coefficient on the basis of collected database which was presented in Table 2.1. Results of modelling for turbulent flow are presented in Table 5.1. The best method for the whole database is Shah 2022 [60] with MAPE= 23.21%. Second best is Shah 2019 [57] with MAPE=24.45% and the third is the modified Mikielewicz correlation with MAPE=24.95%. Cavallini 2006 [26] and Dorao and Fernandino [59] models achieved slightly worse results. Mikielewicz model is recommended for turbulent flow.

Table 5.1 Results of modelling of for consolidated database

Model	MAPE	Number of datapoints below 30%	Percent of data points below 30%
Mikielewicz [51]	35.95%	2220	53.61%
Present work	24.95%	2800	67.62%
Bohdal [58]	85.93%	1050	25.36%
Dorao Fernandino [59]	26.80%	2948	71.19%
Shah 79 [55]	62.22%	1757	37.38%
Cavallini 2006 [26]	28.61%	3162	67.28%
Shah 09 [56]	30.39%	2938	70.95%
Shah 19 [56]	24.45%	2938	70.95%
Shah 22 [60]	23.21%	3014	72.78%

Figure 5.1 presents the graph comparing experimental heat transfer coefficient and prediction results using the original Mikielewicz model [51]. Figure 5.4 present graph for modified Mikielewicz correlation. Figure 5.7 presents graph for Bohdal et al. correlation [58]. Figure 5.10 presents the graph for Dorao and Fernandino correlation [59] whereas Figure 5.13 presents the graph for Shah 1979 correlation [55], Figure 5.16 for Shah 2009 correlation [56], Figure 5.19 for Shah 2019 correlation [57], Figure 5.22 for Shah 2022 correlation [60] and Figure 5.25 present graph for Cavallini et al. correlation [26]. Figure 5.2 presents the graph comparing experimental heat transfer coefficient to prediction results for original Mikielewicz model [51] for databases from Macdonald and Garimella [23,24], Jiang et al. [33], Keinatch [22], Zhuang [28], Longo [39], Milkie [21] and present work experiment. Figure 5.5, Figure 5.8, Figure 5.11, Figure 5.14, Figure 5.17, Figure 5.20, Figure 5.23, Figure 5.26, presents those graphs for subsequent prediction methods. Figure 5.3 present histogram with number of experimental points in given MAPE range for original Mikielewicz correlation [51]. Figure 5.6 presents histogram for the present work modified in-house model. Figure 5.9, Figure 5.12, Figure 5.15, Figure 5.18, Figure 5.21 Figure 5.24, Figure 5.27 present histograms for given prediction methods. These histograms present how many experimental data point fall a in given MAPE range.

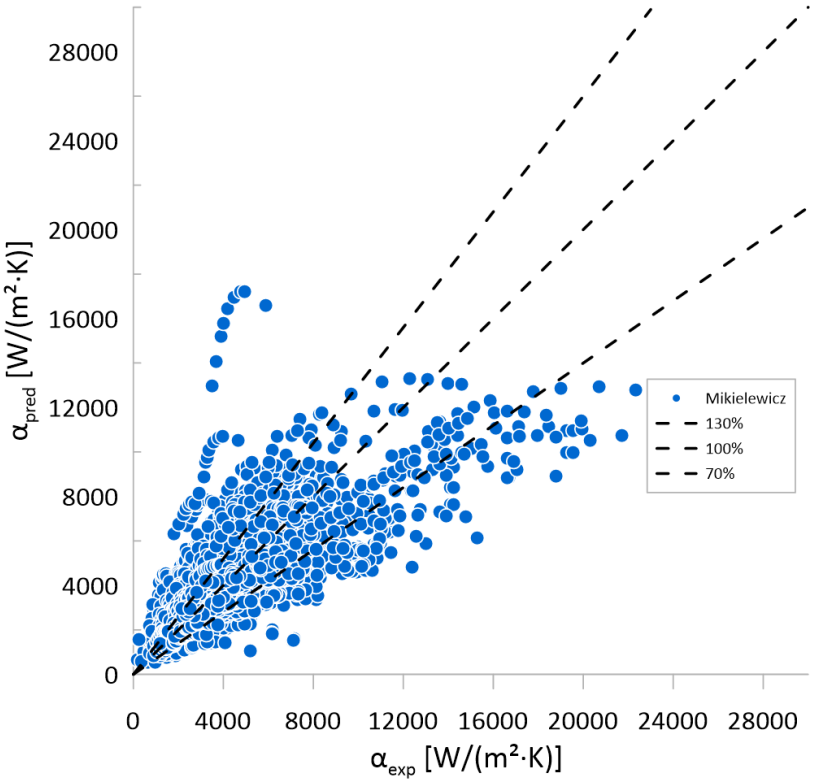

Figure 5.1 Results of modelling with original Mikielewicz correlation [51]

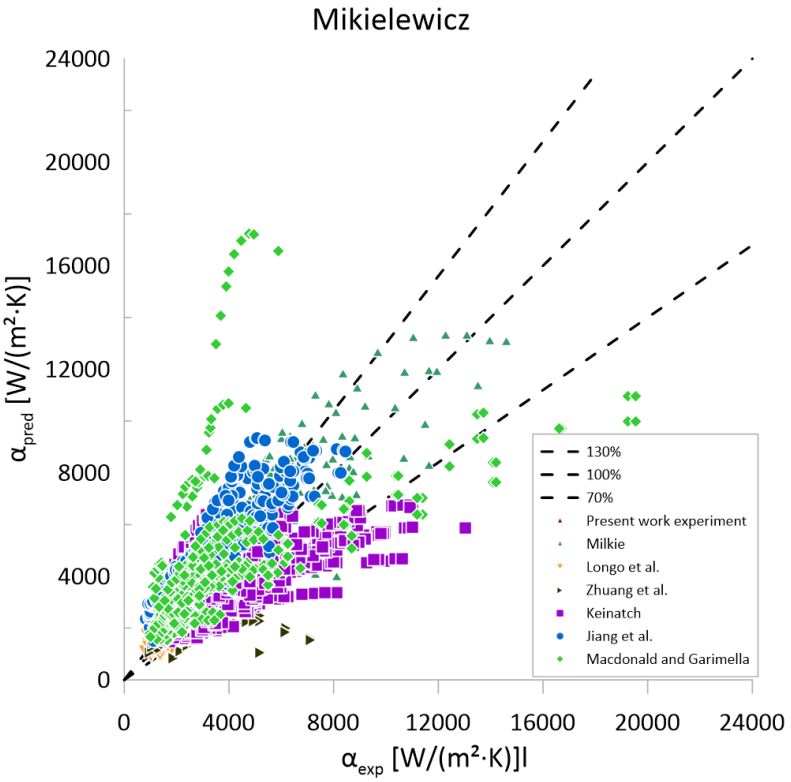

Figure 5.2 Results of modelling with original Mikielewicz correlation [51] for selected databases [21–24,28,33,39] and present work

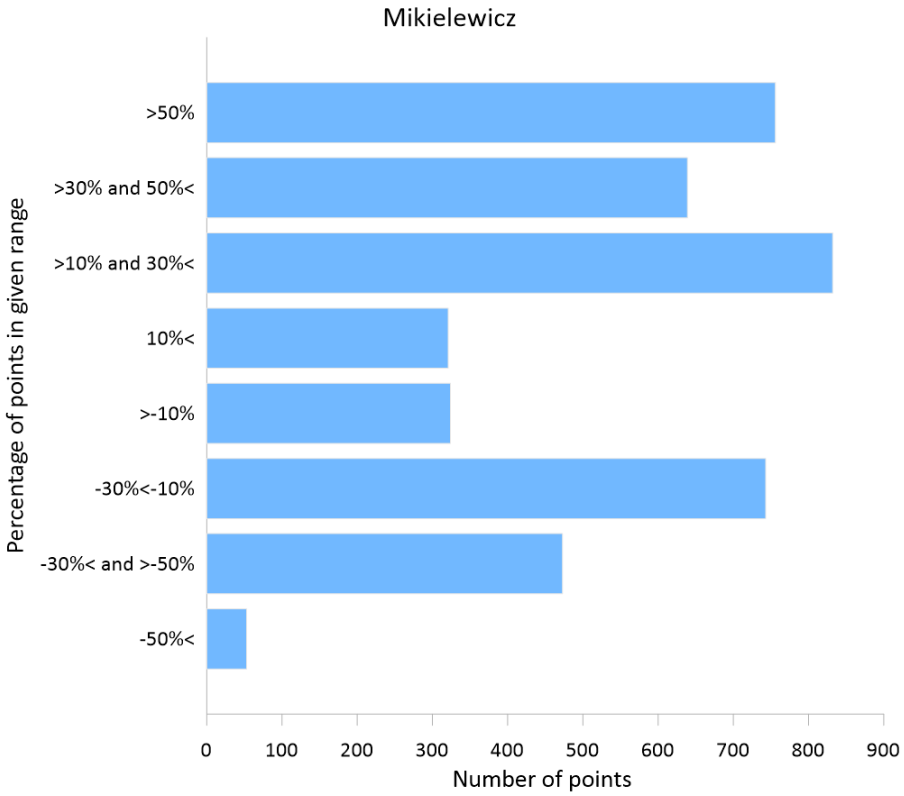

Figure 5.3 Histogram with number of experimental points in given MAPE range for original Mikielewicz correlation [51]

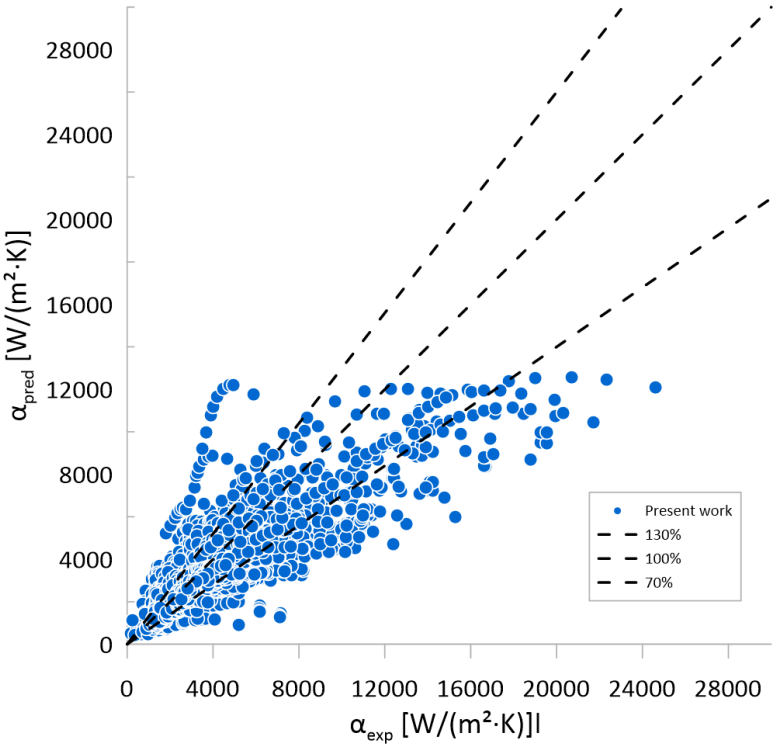

Figure 5.4 Results of modelling with modified Mikielewicz correlation

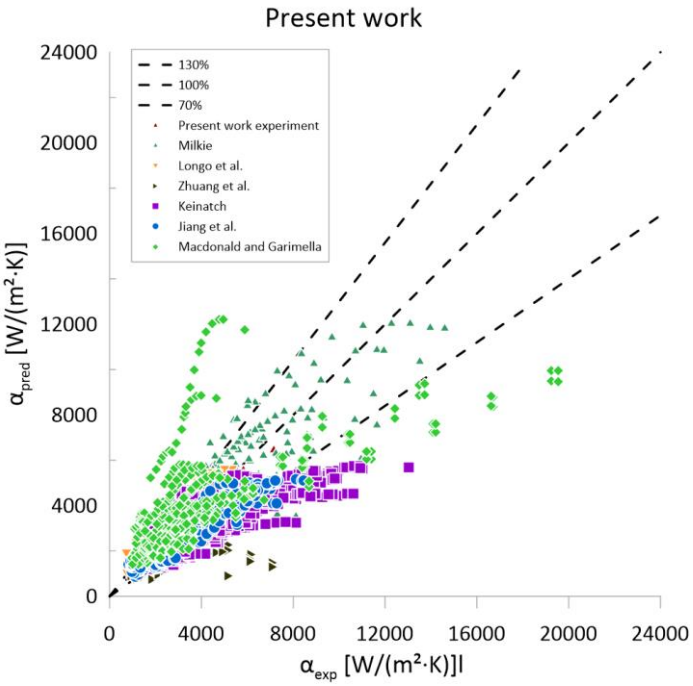

Figure 5.5 Results of modelling with modified Mikielewicz correlation for selected databases [21–24,28,33,39] and present work

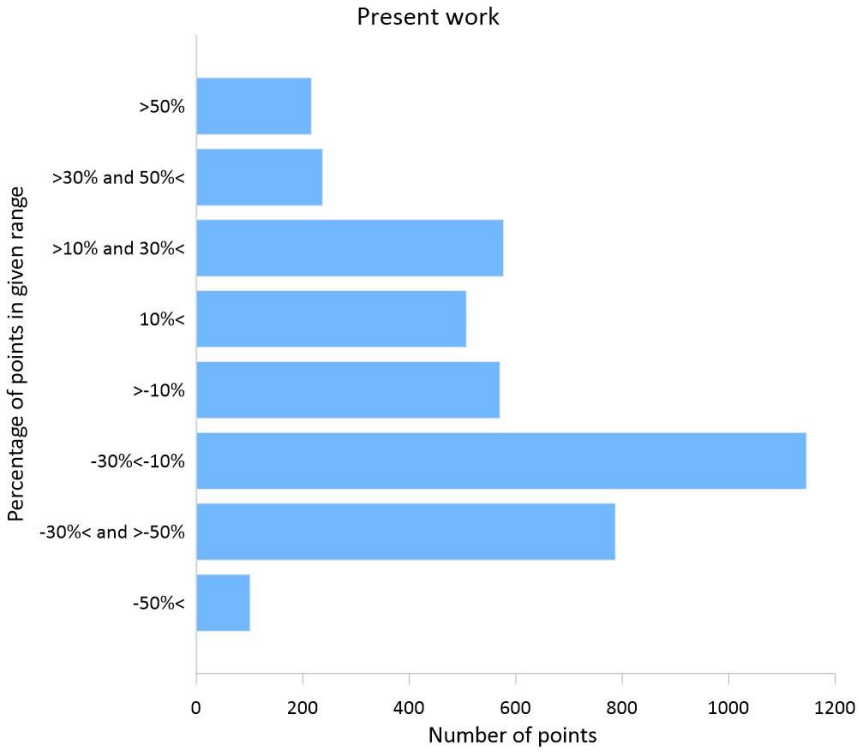

Figure 5.6 Histogram with number of experimental points in given MAPE range for modified Mikielewicz correlation

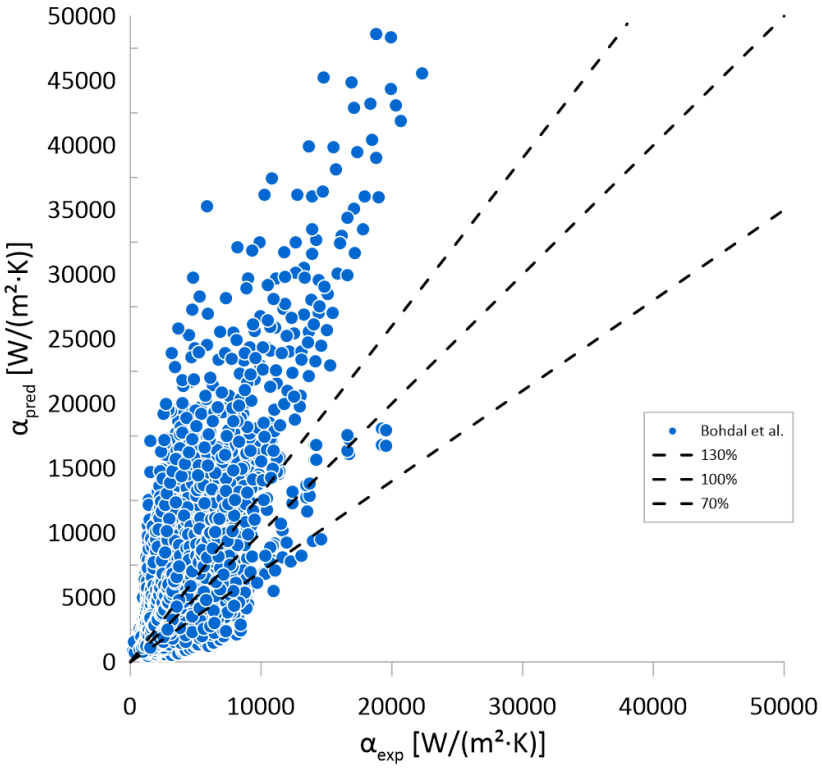

Figure 5.7 Results of modelling with Bohdal et al. correlation [58]

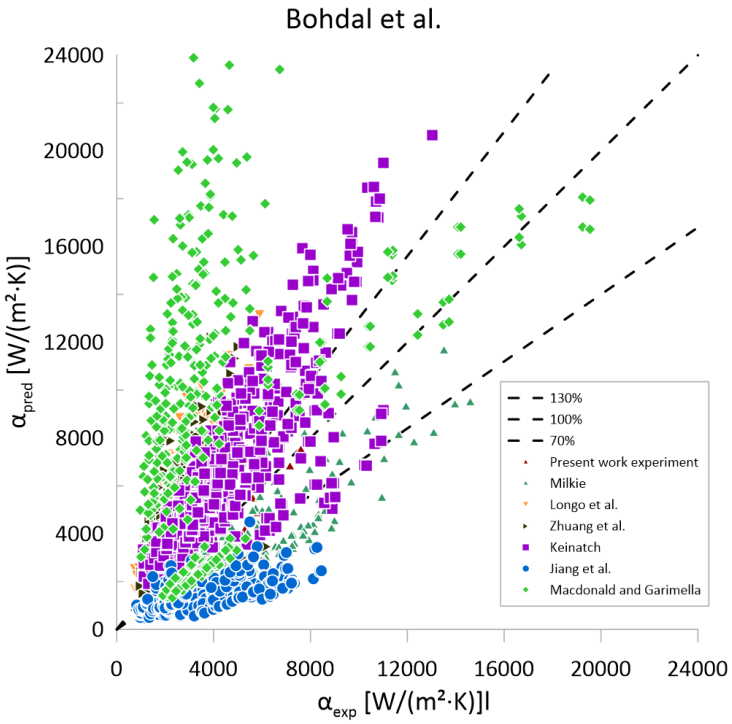

Figure 5.8 Results of modelling with Bohdal et al. correlation [58] for selected databases [21–24,28,33,39] and present work

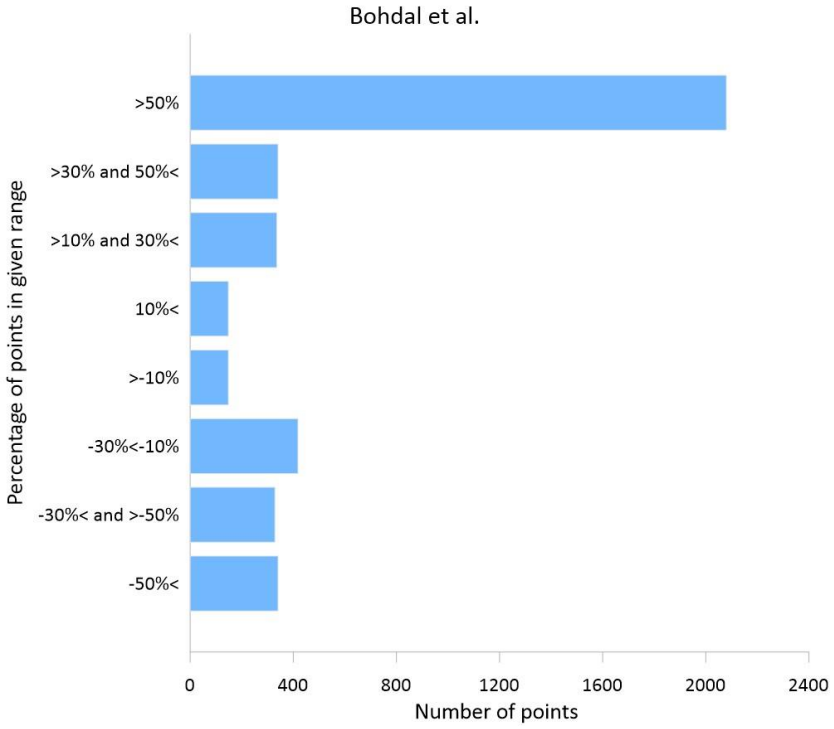

Figure 5.9 Histogram with number of experimental points in given MAPE range for Bohdal et al. correlation[58]

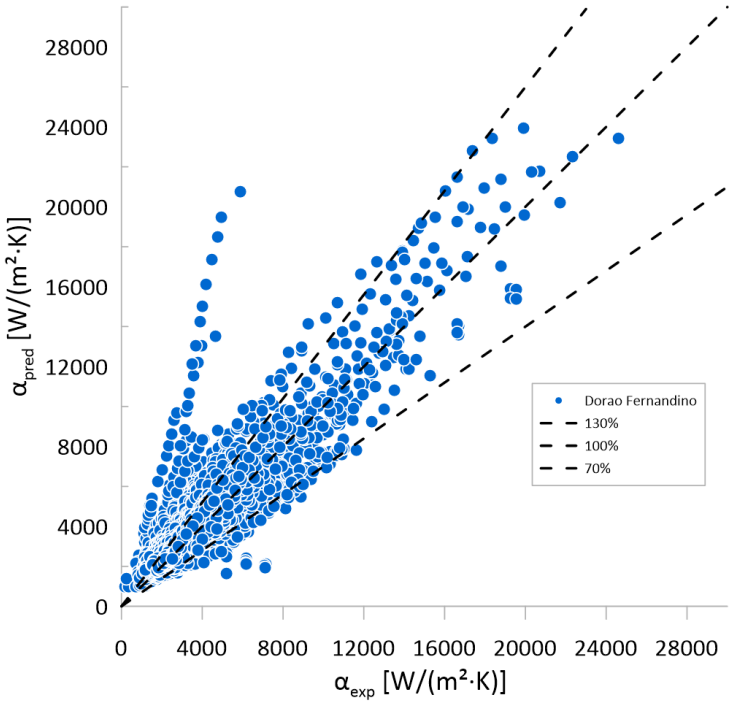

Figure 5.10 Results of modelling with Dorao and Fernandino. correlation [59]

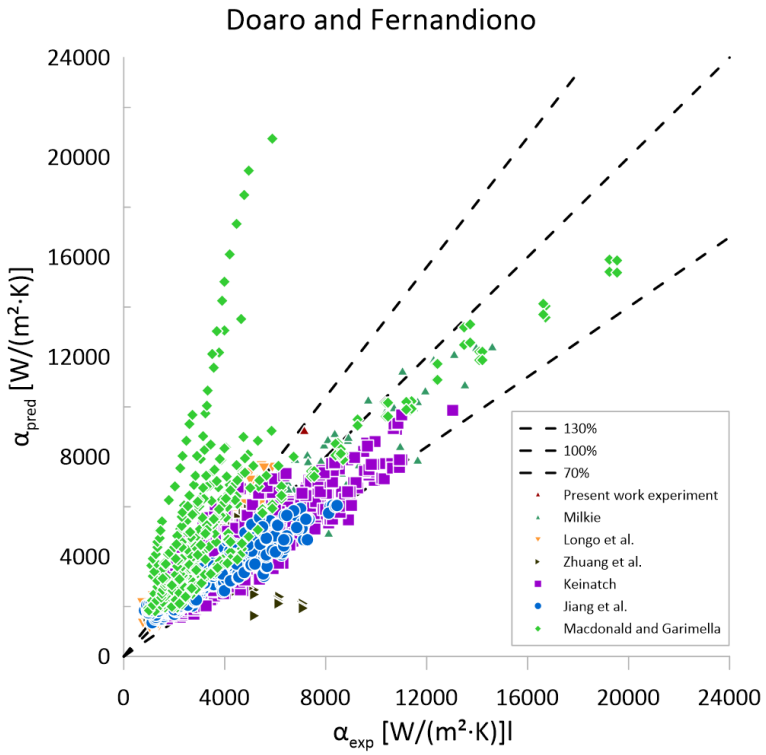

Figure 5.11 Results of modelling with Dorao and Fernandino. correlation [59] for selected databases [21–24,28,33,39] and present work

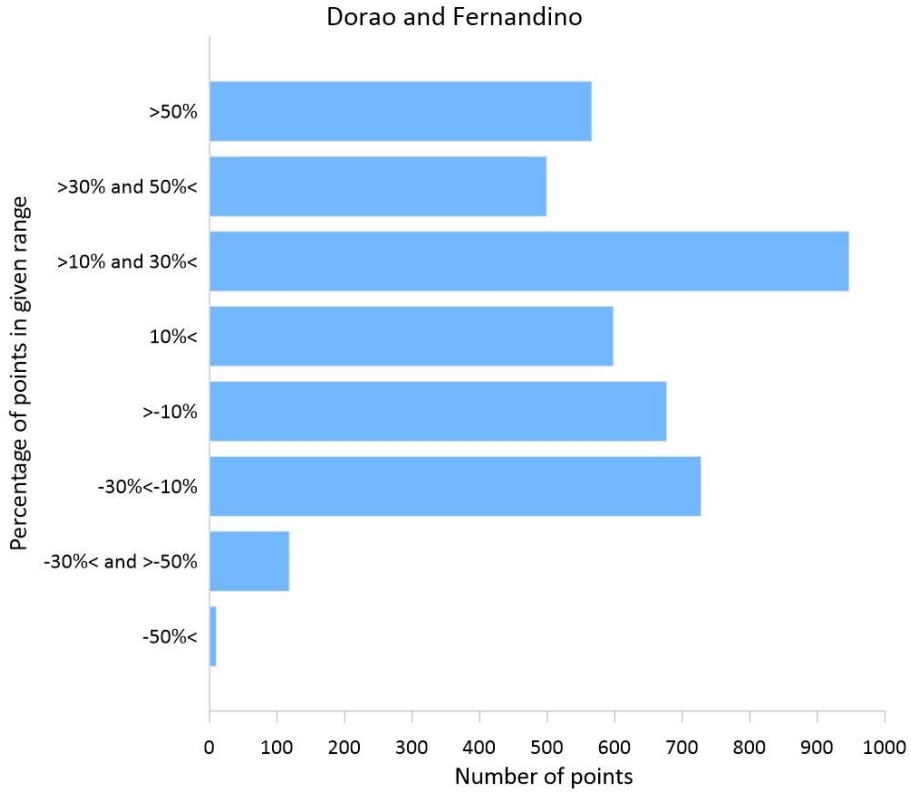

Figure 5.12 Histogram with number of experimental points in given MAPE range for Dorao and Fernandino. correlation [59]

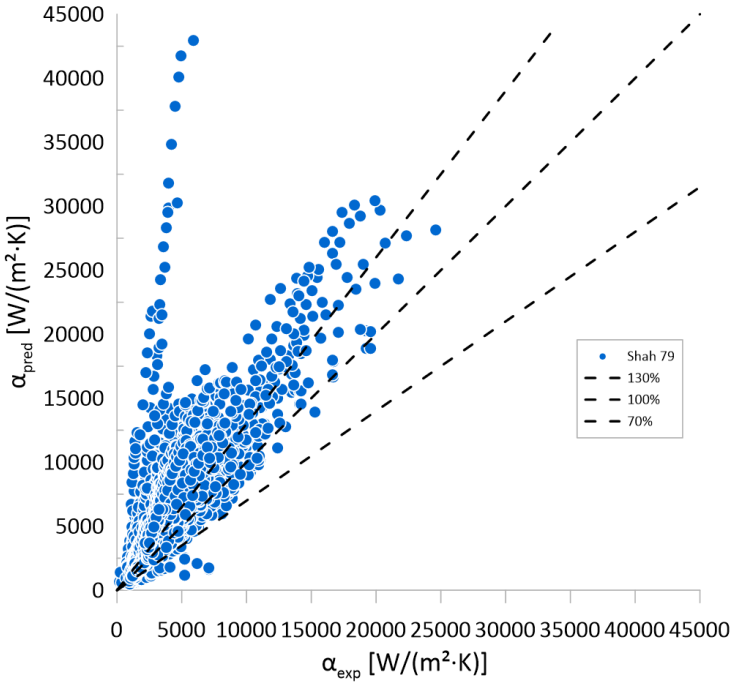

Figure 5.13 Results of modelling with Shah 79 et al. correlation [55]

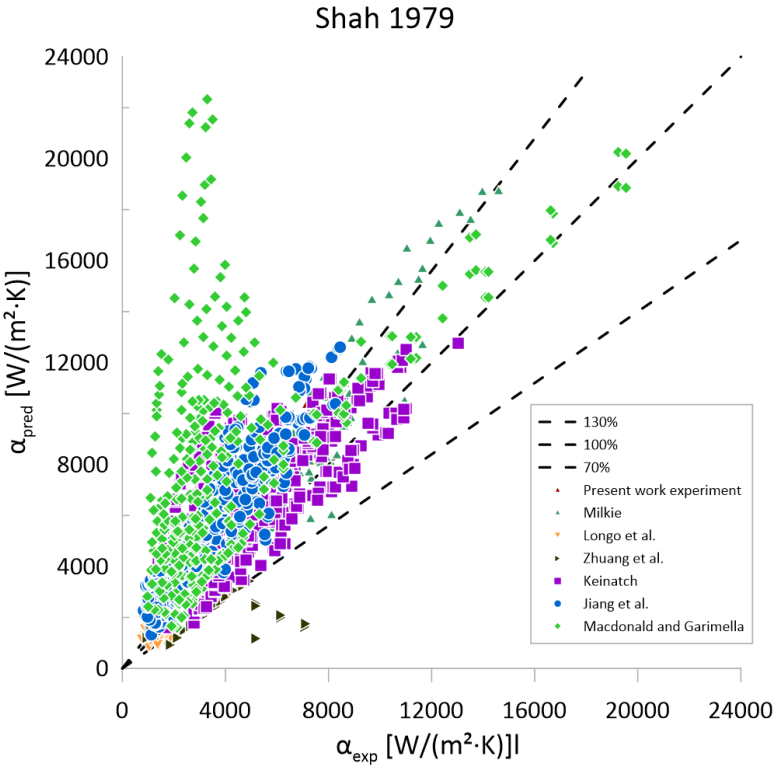

Figure 5.14 Results of modelling with Shah 79 et al. correlation [55] for selected databases [21–24,28,33,39] and present work

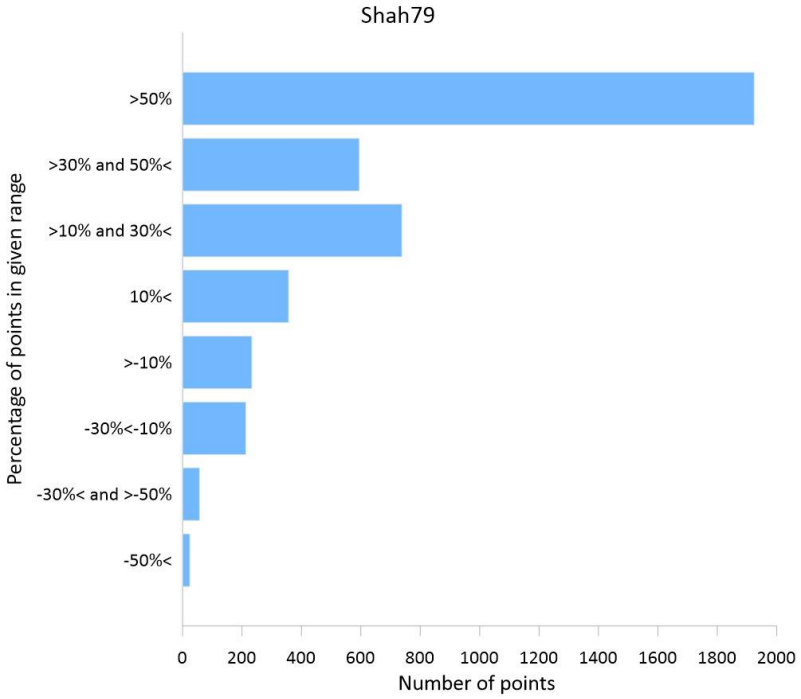

Figure 5.15 Histogram with number of experimental points in given MAPE range for Shah 79 et al. correlation [55]

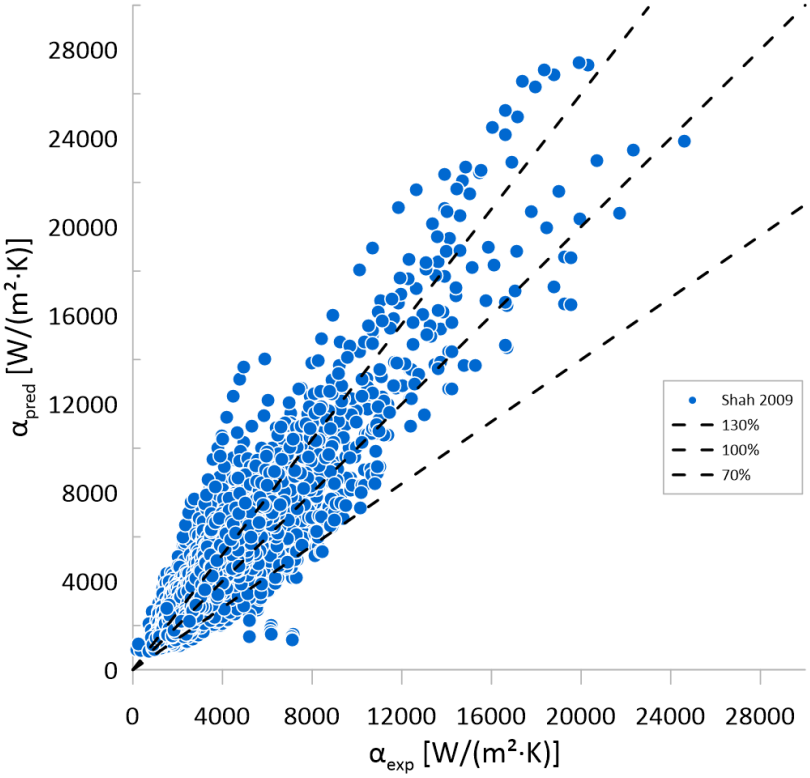

Figure 5.16 Results of modelling with Shah 2009 correlation [56]

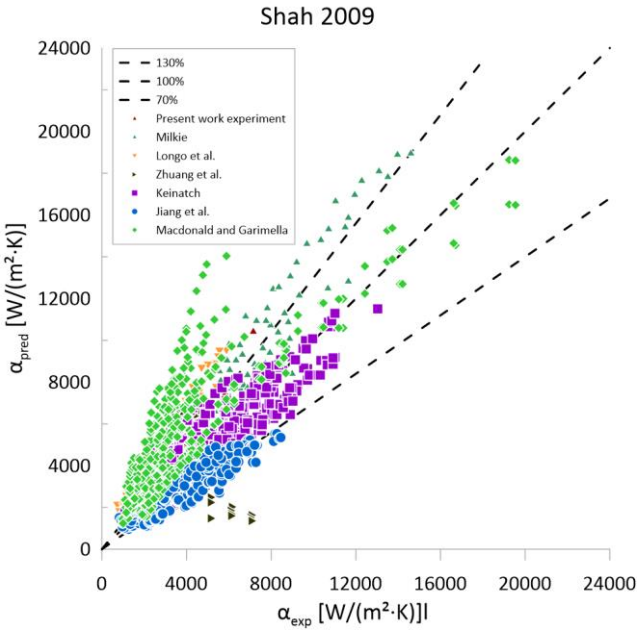

Figure 5.17 Results of modelling with Shah 2009 correlation [56] for selected databases [21–24,28,33,39] and present work

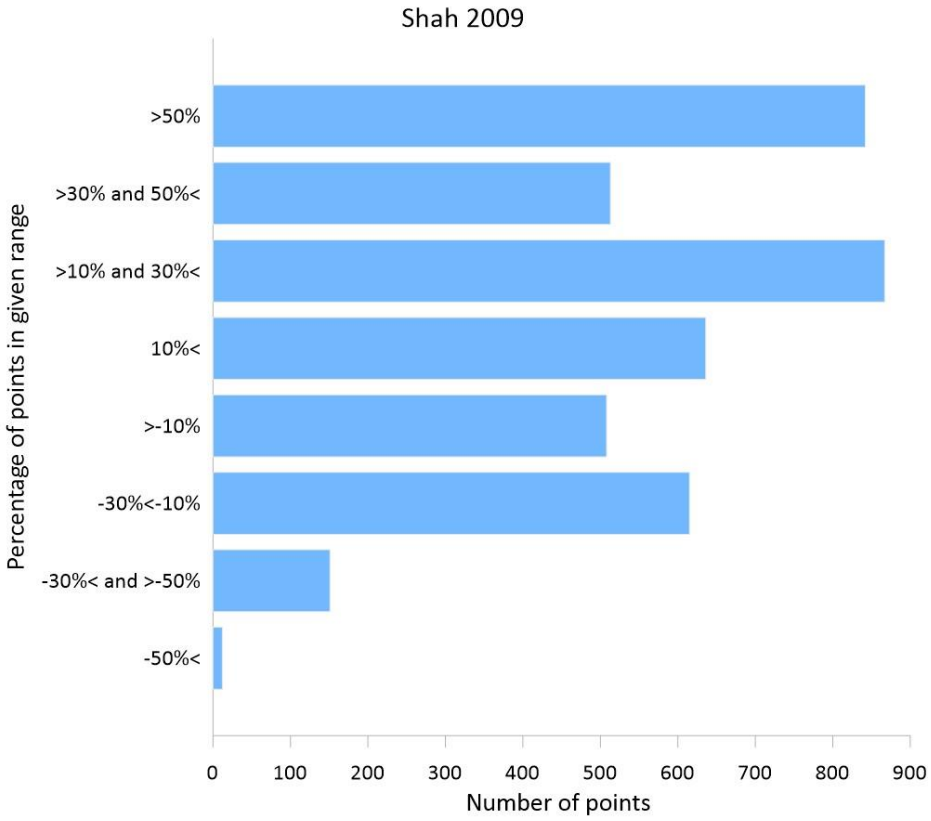

Figure 5.18 Histogram with number of experimental points in given MAPE range for Shah 2009 correlation [56]

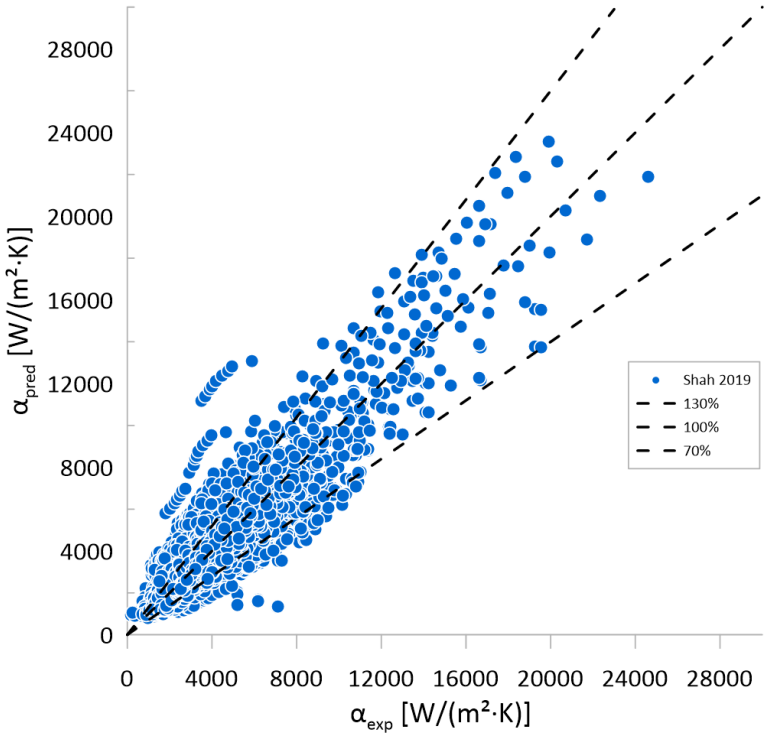

Figure 5.19 Results of modelling with Shah 2019 correlation [57]

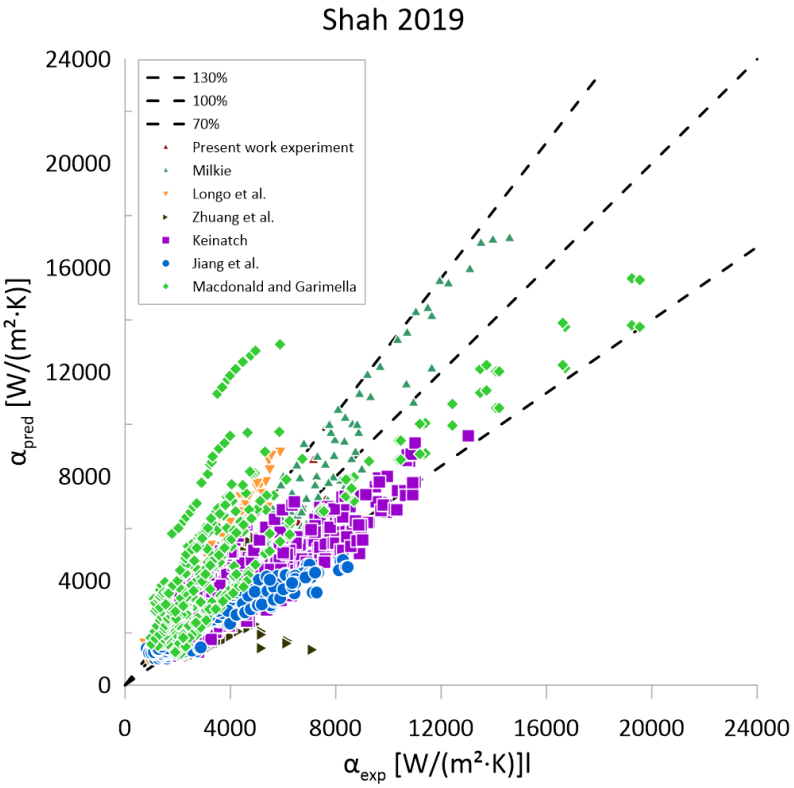

Figure 5.20 Results of modelling with Shah 2019 correlation [57] for selected databases [21–24,28,33,39] and present work

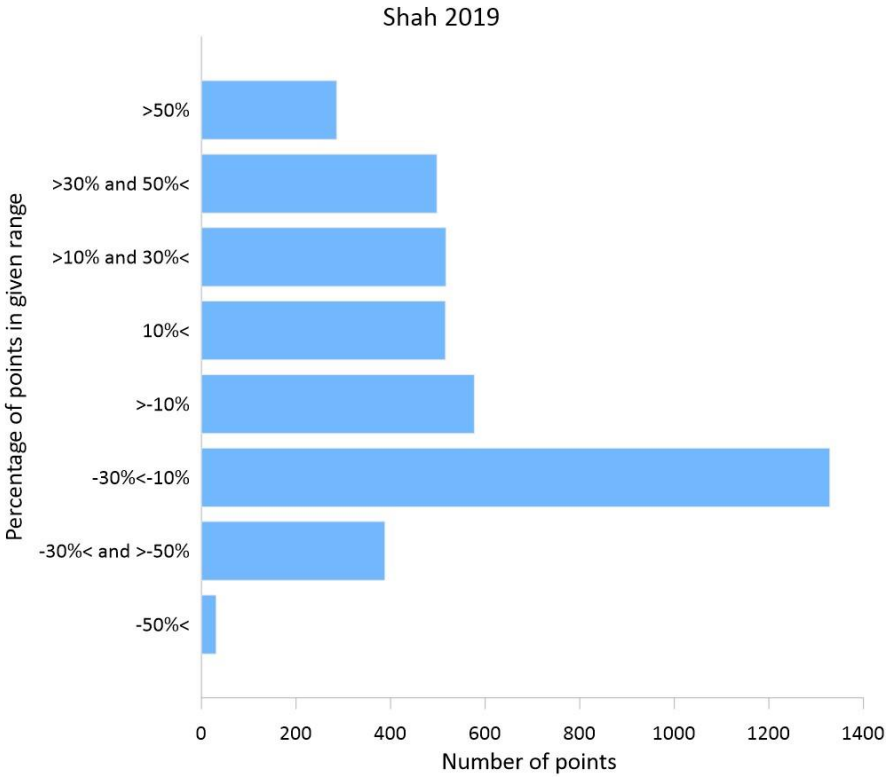

Figure 5.21 Histogram with number of experimental points in given MAPE range for Shah 2019 correlation [57]

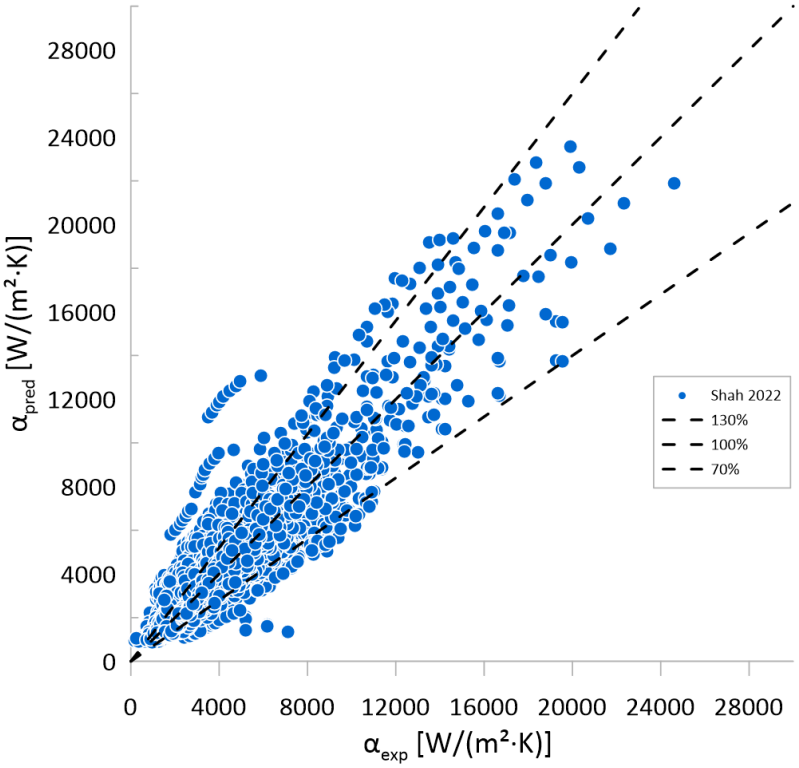

Figure 5.22 Results of modelling with Shah 2022 correlation [60]

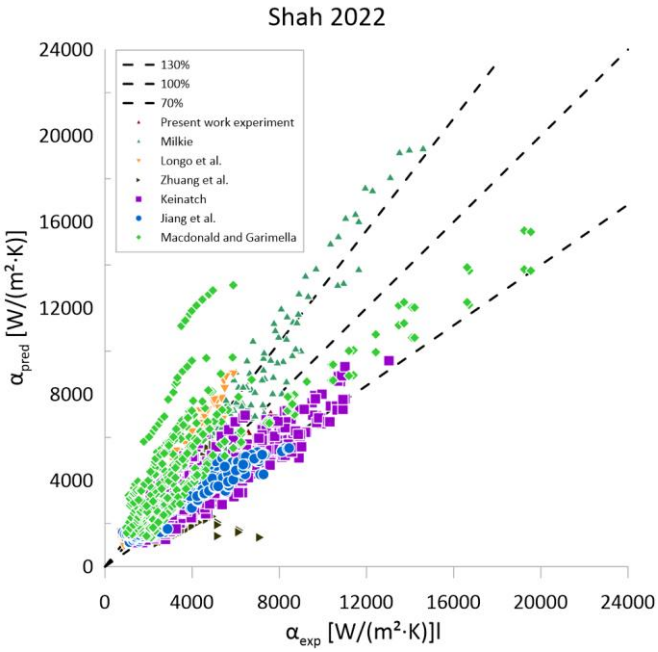

Figure 5.23 Results of modelling with Shah 2022 correlation [60] for selected databases [21–24,28,33,39] and present work

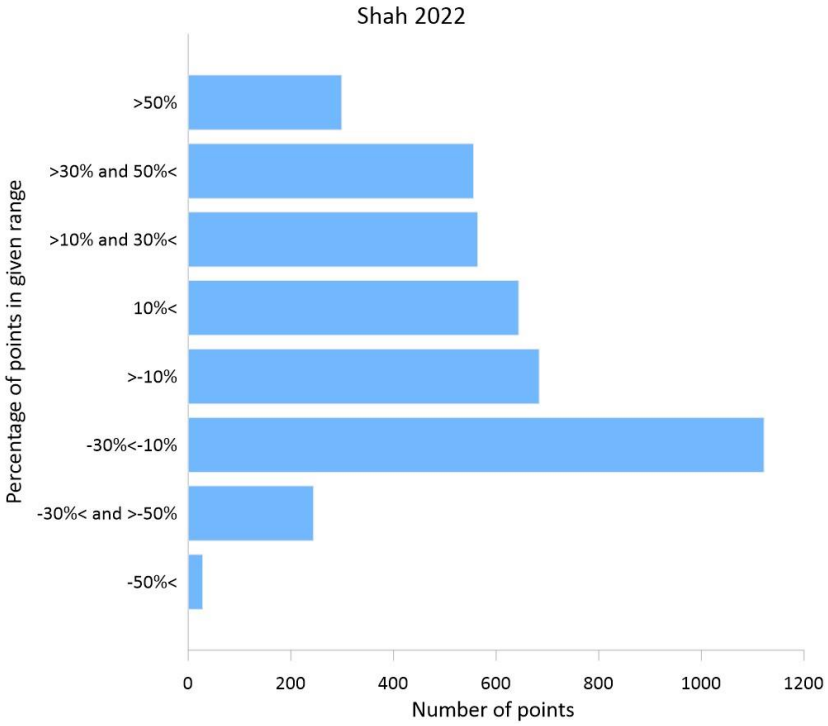

Figure 5.24 Histogram with number of experimental points in given MAPE range for Shah 2022 correlation [60]

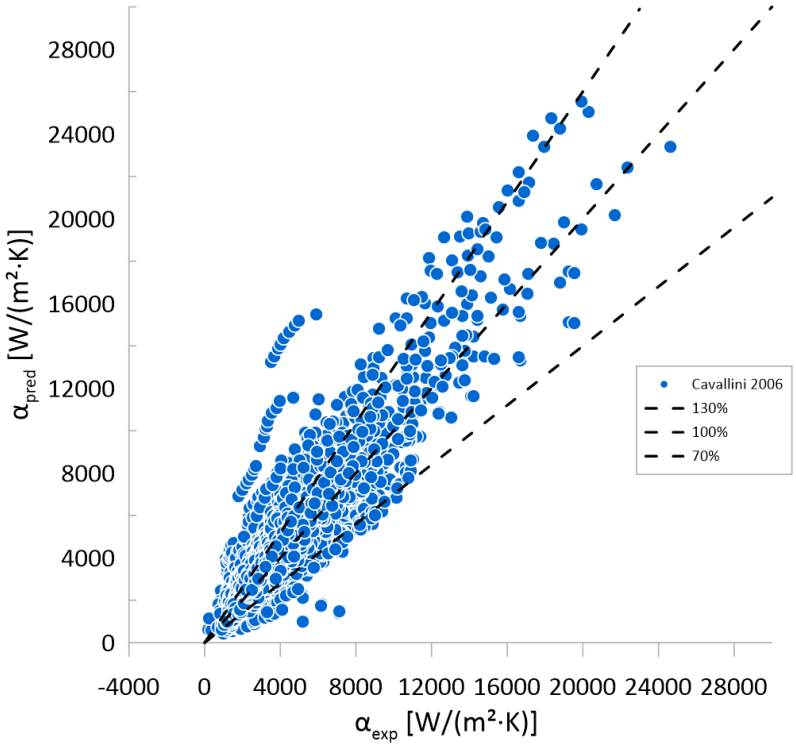

Figure 5.25 Results of modelling with Cavallini et al. correlation [26]

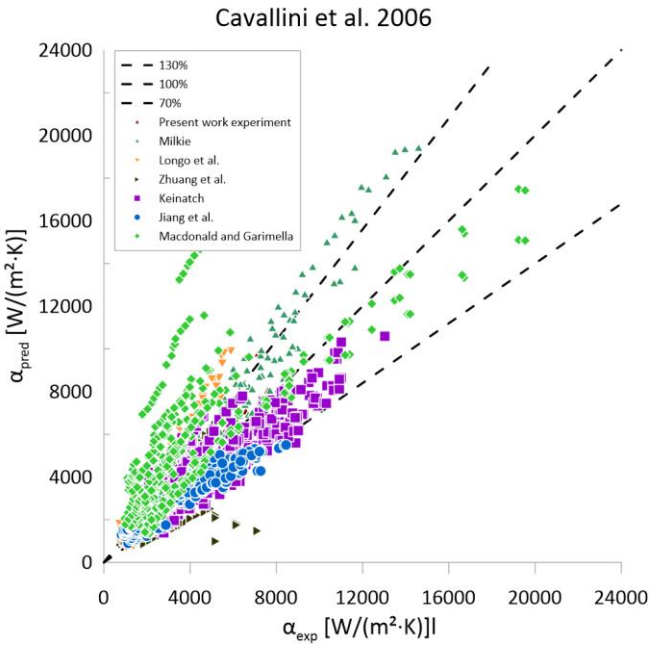

Figure 5.26 Results of modelling with Cavallini et al. correlation [26] for selected databases [21–24,28,33,39] and present work

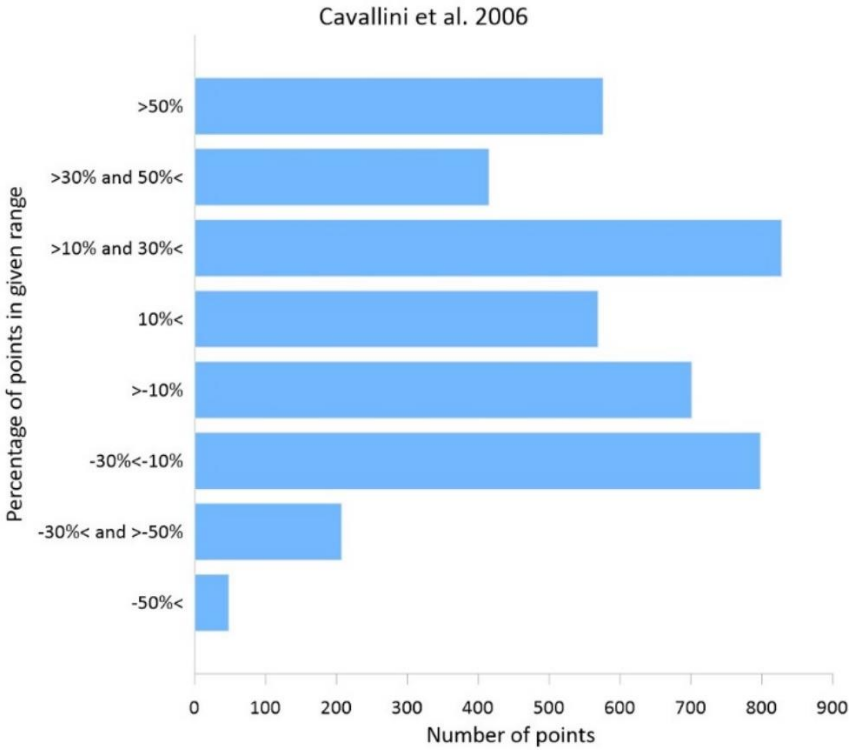

Figure 5.27 Histogram with number of experimental points in given MAPE range for Cavallini et al. correlation [26]

As can be deduced from presented distributions accomplished for selected databases in all cases the bigger scheme of data due to Macdonald et al. [23,24] is not properly predicted by the considered models. The databases due to other considered authors do not exhibit such consistent discrepancies. Those datapoints represent measurements for very high values of reduced pressure (p_r=0.8 and p_r=0.9) of R290. They were left as part of the database because they did not exhibit signs of gross error. They were flowing trends on graphs.

5.1. Results for saturation pressure above 50% of critical pressure

For the sake of examination of models at higher and lower reduced pressures, the acquired database was examined at reduced pressures above p_r>0.5 and below that threshold. For reduced pressure p_r>0.5 a new modified in-house model achieved the best MAPE=23.33%. The second best method is Shah 2022 with MAPE=24.31%. The database for this test consisted of 1547 points.

Table 5.2 Results for saturation pressure above 50% of critical pressure

Model	MAPE	Number below 30%	Percent below 30%
Mikielewicz [51]	47.89%	651	42.08%
present work	23.33%	1158	74.85%
Bohdal [58]	85.44%	408	26.37%
Dorao Fernadino [59]	32.19%	1115	72.07%
Shah 79 [55]	104.29%	203	13.12%
Cavallini 2006 [26]	28.91%	1139	73.63%
Shah 09 [56]	29.45%	1099	71.04%
Shah 19 [56]	26.56%	1099	71.04%
Shah 22 [60]	24.31%	1169	75.57%

5.2. Results for saturation pressure below 50% of critical pressure

For reduced pressure p_r<0.5 the model due to Shah 2022 achieved the best MAPE=22.55% Second best method is Shah 2019 with MAPE=23.20%. Postulated in the work model achieved MAPE=25.91%. The database for this test consisted of 2594 points.

Table 5.3 Results for saturation pressure below 50% of critical pressure

Model	MAPE	Number of datapoints below 30%	Percent of data points below 30%
Mikielewicz [51]	28.83%	1569	60.49%
present work	25.91%	1642	63.30%
Bohdal [58]	86.22%	642	24.75%
Dorao Fernandino [59]	23.58%	1833	70.66%
Shah 79 [55]	39.26%	1338	51.58%
Cavallini 2006 [26]	24.92%	1756	67.69%
Shah 09 [56]	30.95%	1839	70.89%
Shah 19 [56]	23.20%	1839	70.89%
Shah 22 [60]	22.55%	1845	71.13%

5.3. Results for synthetics refrigerants

In order to examine in greater detail the performance of the considered models the available database was scrutinised for synthetic and natural refrigerants. For synthetic refrigerants, Shah 2022 achieved the best result MAPE=20.81% MAPE. Modification of Mikielewicz correlation achieved a result with MAPE=24.90%. Sources containing data for synthetic refrigerants were marked in Table 2.1. The database for this test consisted of 2893 points.

Table 5.4 Results for synthetic refrigerants

Model	MAPE	Number of datapoints below 30%	Percent of data points below 30%
Mikielewicz [51]	35.94%	1535	53.06%
present work	24.90%	1858	64.22%
Bohdal [58]	63.85%	827	28.59%
Dorao Fernandino [59]	21.17%	2236	77.29%
Shah 79 [55]	51.34%	1273	44.00%
Cavallini 2006 [26]	21.67%	2137	73.87%
Shah 09 [56]	24.37%	2088	72.17%
Shah 19 [56]	22.60%	2088	72.17%
Shah 22 [60]	20.81%	2183	75.46%

5.4. Results for natural refrigerants

For natural refrigerants, the method developed in the present work achieved the best MAPE=25.05%. The second best method is Shah 2019. Sources containing data for natural refrigerants were marked in Table 2.1. The database for this test consisted of 1248 points.

Table 5.5 Results for natural refrigerants

Model	MAPE	Number of datapoints below 30%	Percent of data points below 30%
Mikielewicz [51]	35.99%	685	54.89%
present work	25.05%	942	75.48%
Bohdal [58]	137.11%	223	17.87%
Dorao Fernandino [59]	39.84%	712	57.05%
Shah 79 [55]	91.86%	268	21.47%
Cavallini 2006 [26]	37.40%	758	60.74%
Shah 09 [56]	44.34%	850	68.11%
Shah 19 [56]	28.74%	850	68.11%
Shah 22 [60]	28.75%	831	66.59%

5.5. Summary

Developed in the present work modification of the in-house model achieved the best results for reduced pressures above p_r>0.5 and the case of natural refrigerants. The intention of the new model was to improve the predictions, especially at high saturation pressure region. Without a doubt the models due to Shah (2022) [60], Doaro and Fernadino [59] and Cavallini (2006) [26] perform very well in predicting the available database of condensation in flow data. In this company, the modified in-house model does not fall far away from these methods, in fact only the model due to Shah (2022) performed better for the whole database. In the overall judgement of the considered models, it must be remembered the

versatility of the in-house model and its theoretical foundations. Also stressed must be the issue of the correctness of experimental data due to Macdonald et al. [23,24].

6. FEEDFORWARD ARTIFICIAL NEURAL NETWORK PREDICTION METHOD

As mentioned earlier the alternative method to predict heat transfer coefficient is an implementation of the Machine Learning approach. That is a new approach to predictions of heat transfer coefficient in fluid with the phase change, which has recently seen a lot of attention. The author also embraced that approach. In the initial tests, three methods were examined:

- Feedforward Neural Networks (FNN),
- Convolutional Neural Networks (CNN),
- k-means clustering algorithm.

The Python code was utilised for the development of the models. The FNN results were the most promising, leading the authors to focus on this method. A Feedforward Neural Network is a type of Artificial Neural Network where the nodes are connected in a non-circular manner. Unlike Recurrent Neural Networks, which have cycles, a Feedforward Neural Network processes input in a single direction only. This model represents the most fundamental type of neural network, as data consistently flows forward and never moves backward. A multi-layer neural network was developed to predict the heat transfer coefficient during flow condensation, with the network's schematic shown in Figure 6.1. This model was published by Głuch et al. [88] This approach introduced an improved data curation. Firstly data was logarithmized. Next the data was scaled from -5 to 5. Scaling in machine learning aims to bring the range of features to a common scale, ensuring that each feature contributes fairly to the model training process. This prevents some features from overpowering others due to their differing scales, which is important because algorithms such as gradient descent are sensitive to feature magnitudes. By scaling, the convergence speed and stability of the model are improved, especially for distance-based models. Additionally, scaling aids in effective regularization by ensuring that the regularization terms affect all features uniformly. Scaling and logarithmization help achieve consistent model performance across a variety of features and enhance the overall efficiency of machine learning algorithms. Those features allowed enhancement of the performance of Feedforward neural networks. For tests, output data was rescaled and relogarithmized.

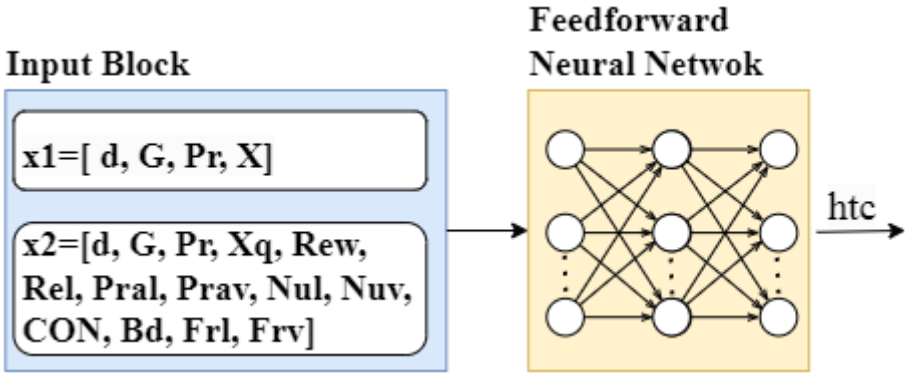

Figure 6.1 Scheme of designed neural network

The applied neural network employs activation functions, such as ReLu (fR) $fR(x) = \max(0, x)$ and Linear $fL(x) = x$. ReLu is a non-linear activation function that is used in multi-layer neural networks or deep neural networks. ReLu is applied to the first four layers, while the last layer uses the linear function. The author aimed to design the network architecture to be as simple as possible while achieving optimal results. Consequently, the network consists of five hidden layers with 50 neurons in the first layer (M=50), 50 neurons in the second layer (N=50), 50 neurons in the fourth layer (D=50), 100 neurons in the fifth layer (P=100), and 1 neuron in the last layer (Q=1). The output (y_{out}) signal from the network is described by the relation:

$$y_{out}(x,\omega) = fL\left(\sum_{i=1}^{Q} \omega_{ji}^{I} \cdot x_i \left(\sum_{l=1}^{P} \omega_{out} fL\left(\sum_{k=1}^{D} \omega_{lk}^{III} fR\left(\sum_{j=1}^{N} \omega_{kj}^{II} fR\left(\sum_{i=1}^{M} \omega_{ji}^{I} \cdot x_i + \omega_{j0}^{I}\right) + \omega_{k0}^{II}\right) + \omega_{l0}^{III}\right) + \omega_{0utO}^{iv}\right) + \omega_{l0}^{V}\right) \quad (6.1)$$

The input signals $x(k) = [x_1, \ldots, x_M]$ provided to neuron *k* are multiplied by sets of weights $\omega(k)$ are passed to the next fully connected layer. The vector of initial weights $\omega(k) = [\omega_1, \ldots, \omega_M]$ is randomized from the range (0,1). The purpose of random initialization is to make sure each neuron in the network begins with a unique initial weight. If all neurons start with identical weights, they would learn the same features, preventing the network from learning complex patterns. Based on the research findings detailed in [89], the Adam algorithm [89] was employed to train the networks under study. The network's performance error was calculated as the difference between the expected output y and the actual output $\hat{y}$ based on the Mean Squared Error (MSE) and Mean Absolute Error (MAE) for all n observations i;i = 1.. n;

$$MSE(y, \hat{y}) = 1/n \sum_{i}^{n} (y(i) - \hat{y}(i))^2 \quad (6.2)$$

The Feedforward Neural Network (FNN) was trained using two configurations of input data. The first configuration included in the learning process only basic thermodynamic parameters: diameter, flow rate, quality, and reduced pressure (relative to critical pressure). The second configuration was much more extended and included these basic parameters along with a set of non-dimensional criteria numbers. Through Pearson's correlation analysis, 17 dimensionless numbers and parameters are identified as the most crucial input parameters. The first configuration aimed to test the potential ability to predict heat transfer coefficients without the use of fluid property databases. Complete data of fluid physical properties for new refrigerants is often not available. Operations without the availability of physical properties would also enable predictions when a user does not have access to programs such as EES or REFPROP. A simpler model is also much cheaper regarding computational power. The second configuration was aimed to produce the most accurate results.

6.1. Test on data randomly selected from the learning database

From the learning database of 3940 experimental points, 30% of measurements were randomly selected for testing. A comparison of these two input configurations is presented in Table 6.1 Both configurations

produced good results for the test dataset. Configuration 1, with only the four basic parameters, yielded accurate outputs despite its limited input data. The second configuration achieved significantly better results, with errors lower than the measurement errors in most experiments. Typically, experiments measuring the heat transfer coefficient (HTC) during condensation have measurement errors ranging from 5 to 20%. It is noteworthy that the ANN presented here is much smaller and simpler than those discussed in studies [72–74,76]. The achieved values of Mean Absolute Error (MAE) and Mean Absolute Percentage Error (MAPE) are a result of careful data preparation and curation for the FNN. The expected values were converted to logarithmic values and rescaled, which enabled the FNN to achieve high quality results. For both configurations values of MAPE are lower than typical two phase condensation measurement uncertainty. ANN learned also the prediction of systematic errors. Because of that test on the excluded database is needed.

Table 6.1 FNN evaluations on the test dataset for different input combinations

Case	Number of input parameters	Input parameters	MAE	MAPE
1	4	d, G, Pr, x	466.52	11.76%
2	17	d, G, Pr, x, Re_v, Re_l, Pr_l, Pr_v, Nu_l, Nu_v, Con, Bd, Fr_l, Fr_v, Fr_{lo}, Fr_{lo}, We_{lo}	386.28	10.12%

Histograms displaying the distribution of input parameters are shown in the Figure 6.2. Vertical axis represent number of points and horizontal axis represent value of parameter. These parameters are detailed in the nomenclature section, with the most significant ones being diameter, mass velocity, reduced pressure, and quality, all measured during the experiment. The remaining parameters are criteria numbers, calculated using fluid properties and the mentioned experimental parameters. The learning process of the first dataset is illustrated in Figure 6.3. Figure 6.4 and Figure 6.5 present the comparison between experimental and calculated values of the heat transfer coefficient (HTC). The expected and output values for the training dataset indicate good results for sparse input data. Both variants were trained for 100 epochs. Epoch, in machine learning numenclature, refers to the one entire passing of training data through the algorithm.

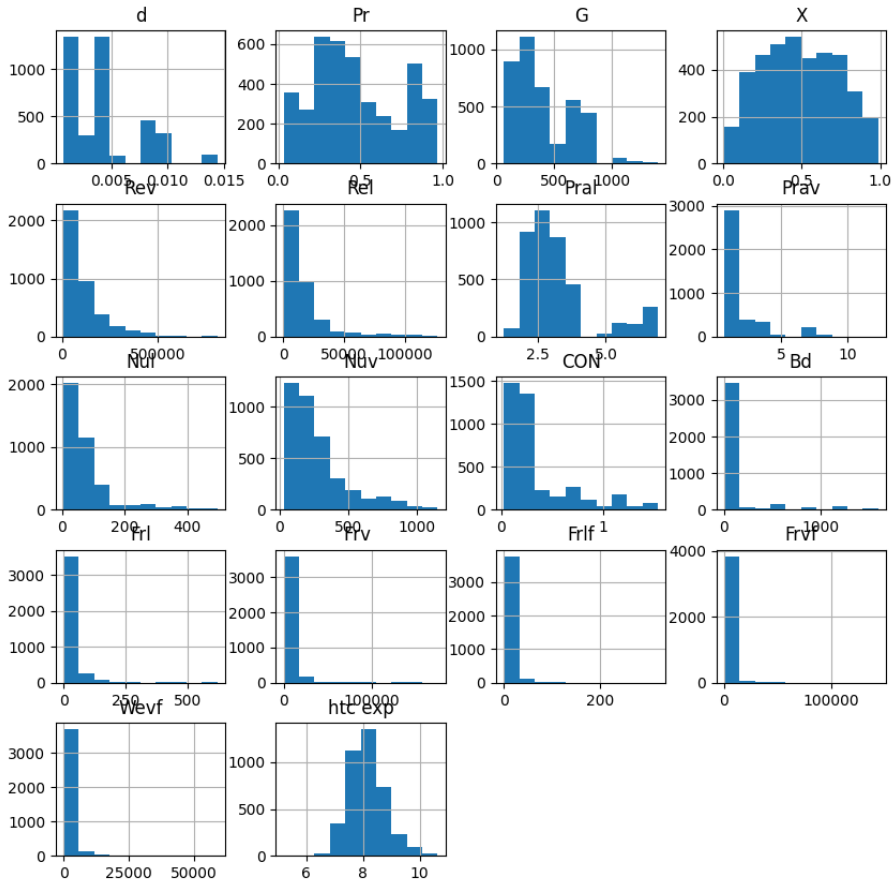

Figure 6.2 Histograms that present the distribution of input parameters

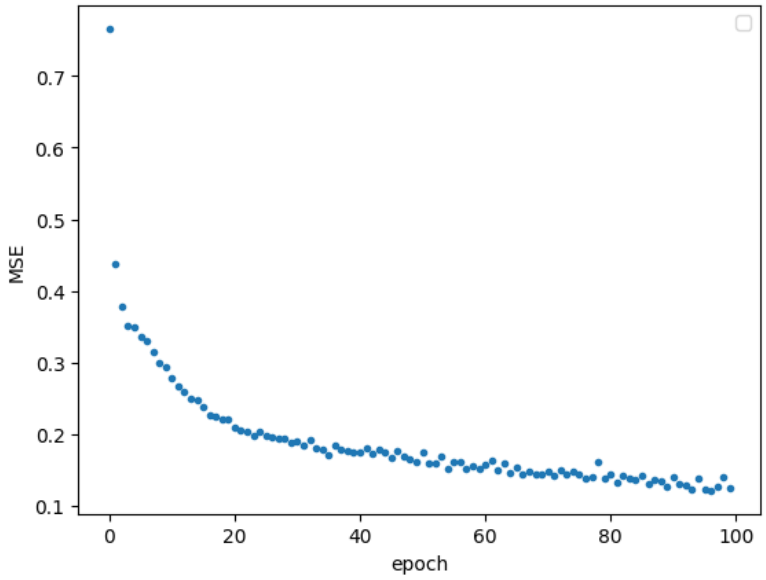

Figure 6.3 Learning graph for the first input configuration

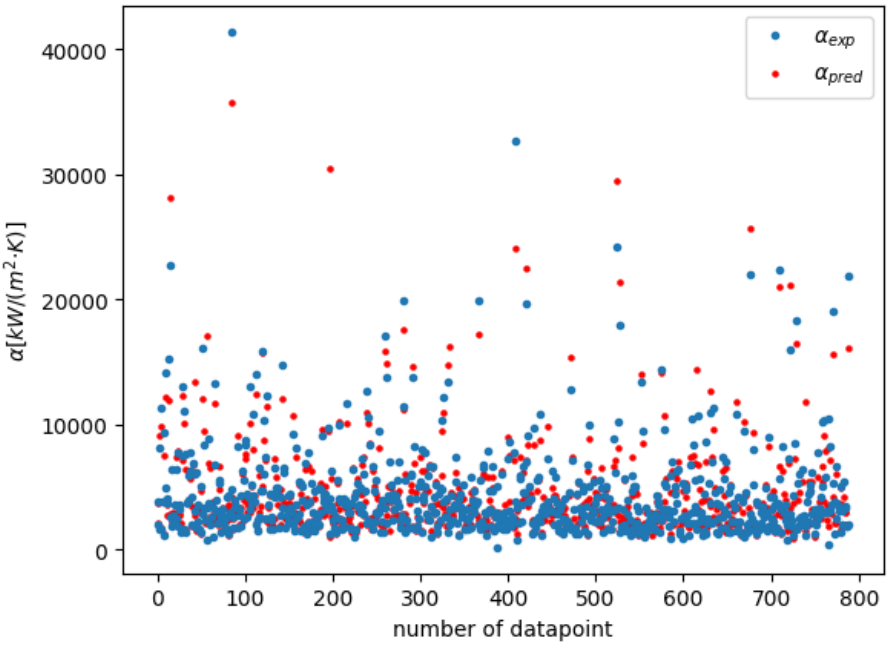

Figure 6.4 Comparison of experimental heat transfer coefficient and results for the first input configuration

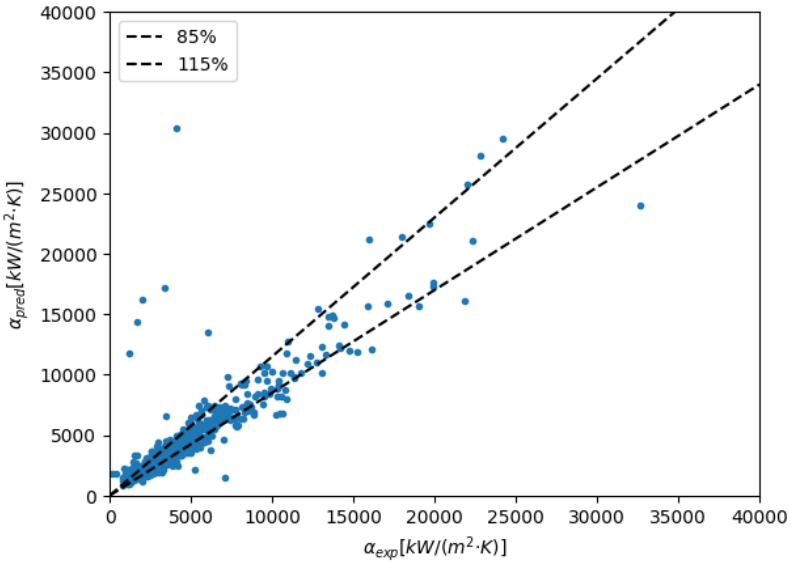

Figure 6.5 Comparison of HTC value measured during the experiment and ANN output data for the first input configuration

The learning process of the second dataset can be observed in Figure 6.6. Comparison of experimental and calculated values of HTC can be observed in the Figure 6.7 and Figure 6.8. Better results can be observed for the second configuration. Learning process is significantly faster for the second

configuration. It can be seen that consistency between experimental and predicted values is much better.

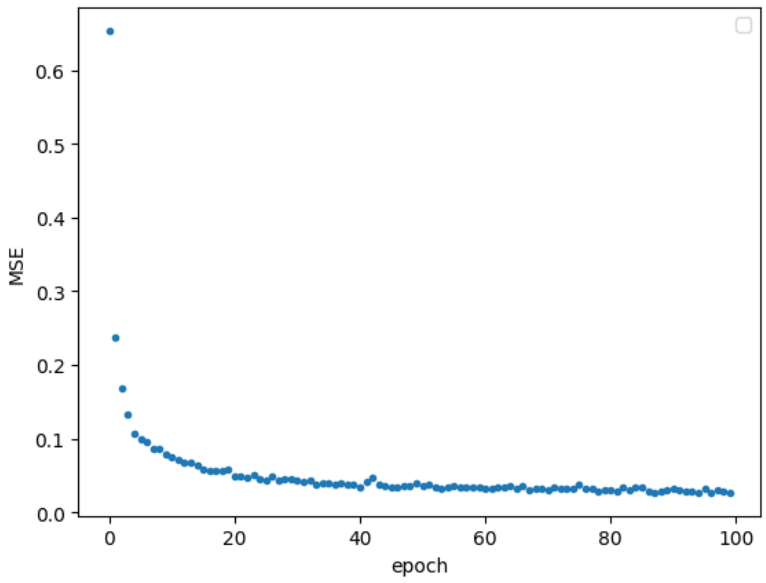

Figure 6.6 Learning graph for the second input configuration

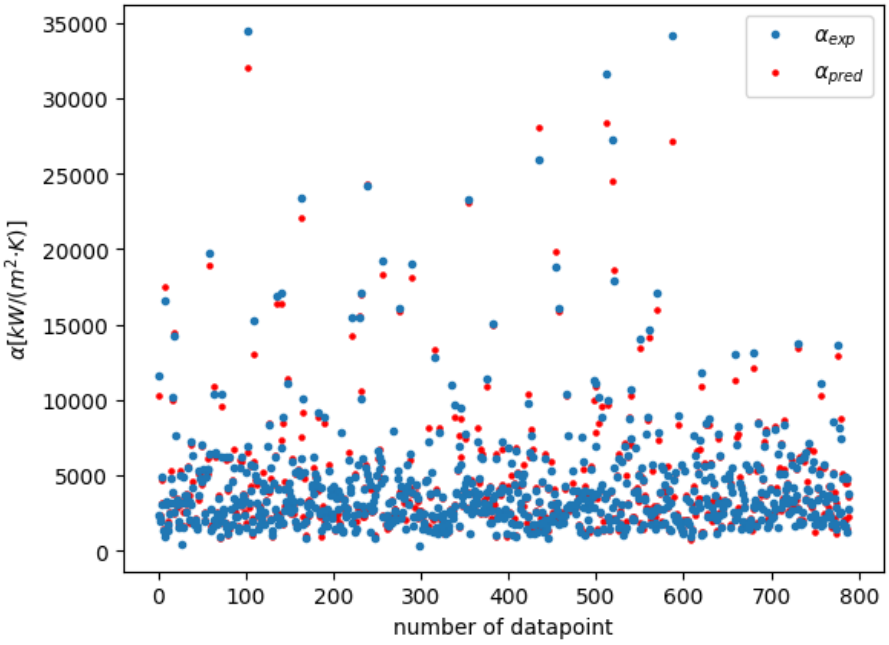

Figure 6.7 Comparison of experimental heat transfer coefficient and results in for the second input configuration

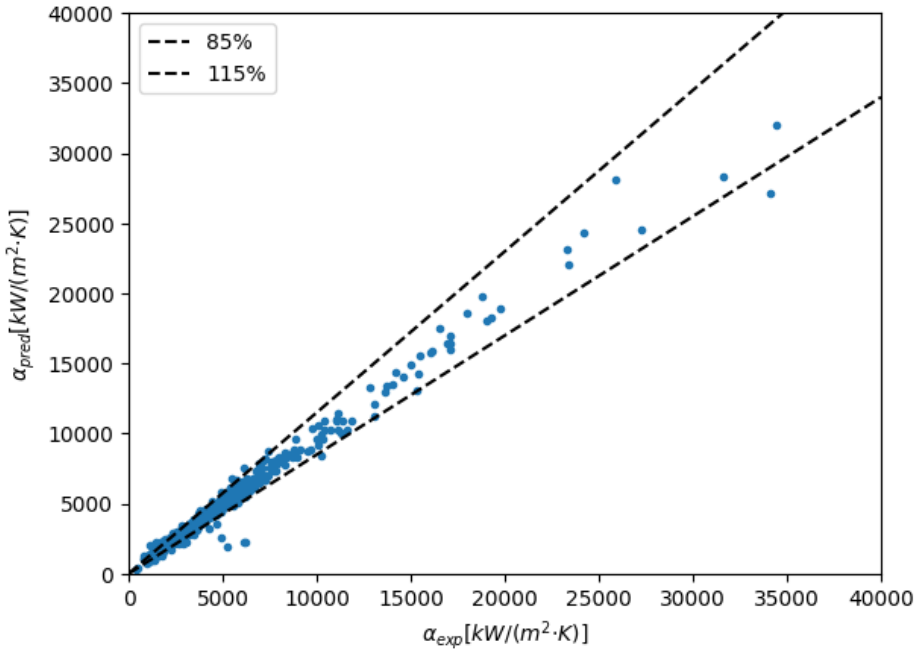

Figure 6.8 Comparison of HTC value measured during the experiment and ANN output data for the second input configuration

6.2. Test on data excluded validation database

The convincing strategy to the test the realiability of the model is to perform tests on data, from experiments, which do not take part in the learning process. Excluded database is composed form 6 data sources excluded from the learning database. The same excluded database is used by Nie [76]. First configuration which does not have access to criterial numbers and thermophysical properties failed in this case. Second configuration achieved satisfactory result of MAPE=21.19% which is better than typical value of MAPE obtained in the case of classical correlation which is usually higher than 30%. Value of MAPE is in range of typical experimental uncertainty which is around 20-30% for the two phase condensation measurements. Results of modelling are presented in Table 6.2. Excluded database consist of 367 data points collected by Cavallini et al. (only R410a) [30], Keinar and Garimella [44], Moreira et al. [45] and Huang et al. [46].

Table 6.2 FNN evaluations on the excluded testing dataset for different input combinations.

Case	Number of input parameters	Input parameters	MAE	MAPE
1	4	d, G, Pr, x	4601.9	136.84%
2	17	d, G, Pr, x, Re_v, Re_l, Pr_l, Pr_v, Nu_l, Nu_v, Con, Bd, Fr_l, Fr_v, Fr_{lo}, Fr_{lo}, We_{lo}	703.47	21.19%

Figure 6.9 and Figure 6.10 present results for the first configurations while Figure 6.11 and Figure 6.12 show result for the second configuration. In the Figure 6.9 can be observed that the first configuration managed to accurately predict most of database, but failed to a significant extent at some points. Second configuration manged to predict heat transfer coefficient much better what can be seen in Figure 6.11. Data point number in Figure 6.9 and Figure 6.11 represent data for Cavallini et al. [30] for points 1-40, for Keinar and Garimella [44] 41-190, for Moreira et al. [45] 191-331 and Huang et al. [46] 332-367.

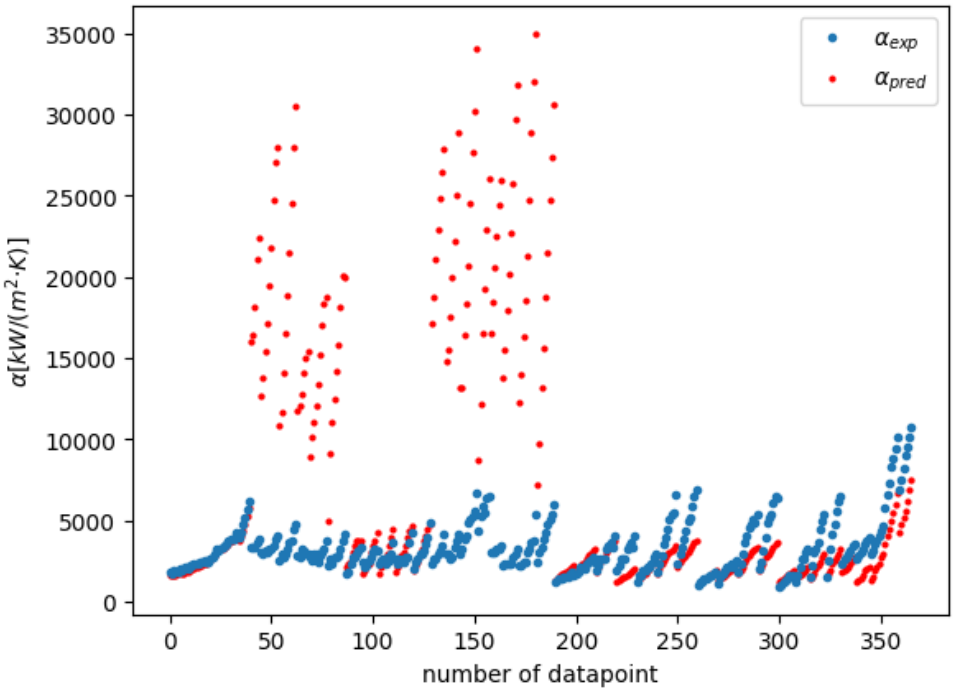

Figure 6.9 Comparison of experimental heat transfer coefficient and results for the first input configuration for validation dataset

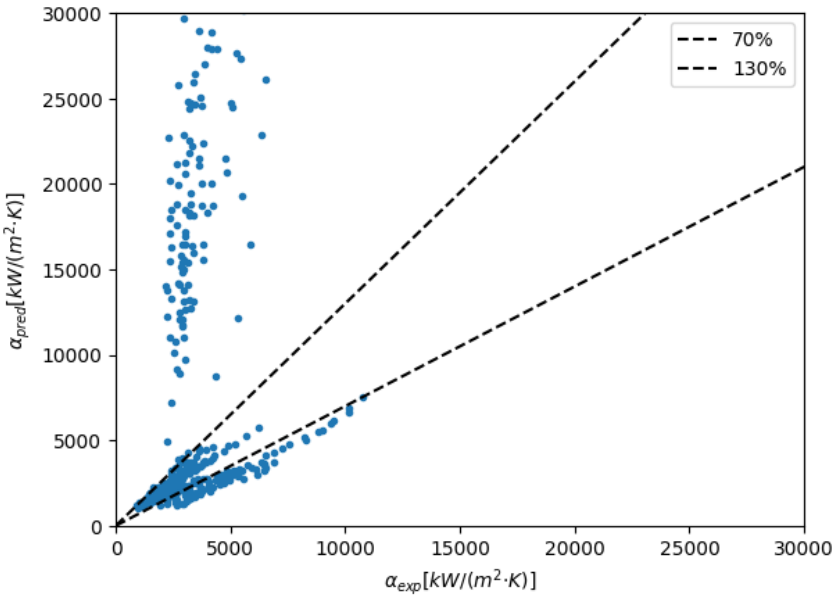

Figure 6.10 Comparison of HTC value measured during the experiment and ANN output data for the first input configuration for validation dataset

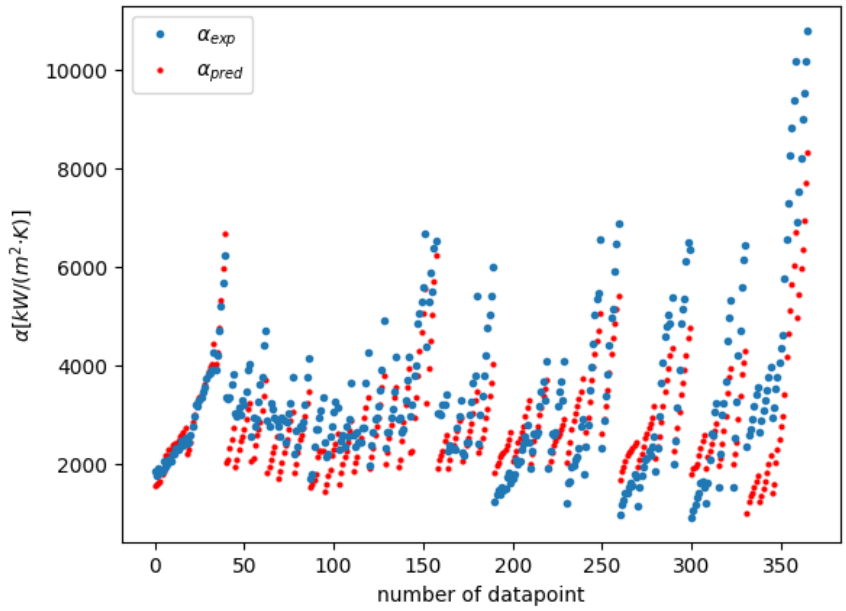

Figure 6.11 Comparison of experimental heat transfer coefficient and results in for the second input configuration for validation dataset

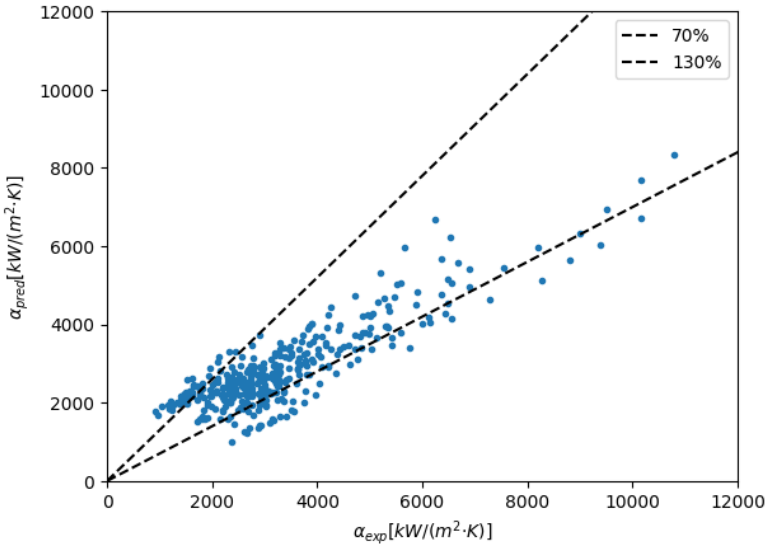

Figure 6.12 Comparison of HTC value measured during the experiment and ANN output data for the second input configuration for validation dataset

6.3. Summary

Machine learning prediction methods presented previously in the state of the art chapter are compared in Table 6.3. These methods cannot be directly compared between themselves because of differences in learning/testing and validation databases. Furthermore, some methods predict Nusselt number, while others predict heat transfer coefficient. Validation database is defined as data collected on the laboratory testing stand which was not used for learning purposes. Test on validation dataset "real case scenario test" is crucial, because Machine Learning methods do learn how to predict systematic errors which usually leads to standard test giving results lower than typical uncertainty of two phase heat transfer experiment. Validation dataset allows to exclude ability of ML models of prediction of uncertainty of learning dataset. Hughes et al. [78] and Mattiuzzo et al. [77] methods were trained only for data collected in the one laboratory that does not give "real case scenario" results. Feedforward Neural Network (FNN) developed in this work was compared against the same validation dataset as Nie et al.[76] and achieved MAPE=21.19%. The excluded database consists of 366 data points collected by Cavallini et al. [30], Keinar and Garimella [44], Moreira et al. [45] and Huang et al. [46]. Nie et al. [76] developed XGboost model which achieved a slightly better result with MAPE=19.64%, but their model is much more complex and demanding in the case of computation resources. Furthermore, this work learning dataset included experimental data for a much wider range of reduced pressure up to 0.9 while Nie et al. learning data focused on typical HVAC parameters range, which limit their ML method applicability. Results of the prediction of excluded datasets for all presented methods span from 12% to 197%. Worst results were achieved for fluids which were not part of the training dataset. The best results were achieved for fluids which were part of training datasets and had similar properties range to those used in the training

dataset. The best result for their validation dataset was achieved by Moradkhani et al. [75] MAPE=12.63%. The novelty of the present work is its focus on the prediction of heat transfer coefficient in increased reduced pressure conditions. Created Feedforward Neural Network (FNN) is simpler and less demanding in case of computational power than all analysed methods which conducted tests on proper validation datasets.

Table 6.3 Comparison of Machine Learning heat transfer prediction methods

Author	Type of ML method	Hyper-parameter values	Modelled process	Predicted parameter	Result for randomly selected test data MAPE	Result for data from excluded validation experiments MAPE
Hughes et al. [78]	SVR	Kernel = rbf, C = 3000, ε = 0.00007	Condensation heat transfer	Nusselt number	4.9% (data from one laboratory)	-
Mattiuzzo et al. [77]	ANN	1 hidden layer 12 neurons	Condensation heat transfer	Nusselt number	-	MAPE 5.4% (data from one laboratory)
Moradkhani et al.[75]	GPR	lack of information	Condensation heat transfer	Nusselt number	4.5%	12.63%
Moradkhani et al. [74]	GPR	lack of information	Boiling heat transfer inside coiled tube	Nusselt number	5.93%	-
Nie et al. [76]	XGboost	lack of information	Condensation heat transfer	heat transfer coefficient α	6.16%	19.64%
Qiu et al. [72]	ANN	(75,70,60,50,30,20,10) hidden layers	Boiling heat transfer	heat transfer coefficient α	14.3%	15.2%, 20.3% and 197.3% for different datasets
Zhou et al. [73]	ANN	(150,140,130,120,110,100,90,80,70,60,50,40,30,20,10) hidden layers	Condensation heat transfer	heat transfer coefficient α	6.8%	16.8%, 14.8%, 37.6%
present work	FNN	(50, 50, 50, 50, 100) hidden layers	Condensation heat transfer	heat transfer coefficient α	10.12%	21.19%

7. FLOW PATTERNS TRANSITION PREDICTION METHOD

Flow patterns during condensation in horizontal channel have been captured with high speed camera inside a 3 mm diameter horizontal tube. In the previous study published by Głuch et al. [18] boiling flow patterns inside a 3 mm diameter vertical channel have been recorded. In this chapter the flow maps are presented. In Figure 7.1 flow structures in horizontal channel are presented at reduced pressure p_r=0.2. The first flow pattern is a bubbly flow, the second is a wavy-stratified flow and the third one is an annular flow. An example of flow patterns inside vertical channel are presented in Figure 7.2. The first photo presents bubbly flow, the second elongated slug, the third is intermittent flow, and the last two are annular flows. Flow patterns in horizontal channel were captured in this study experiment after condensation test section. All flow patterns for horizontal channel are presented in chapter 4. Flow patterns in vertical channel were captured in study [18] after boiling test section. Patterns were recorded in the adiabatic visualization test section. Photos of all patterns for vertical channel are presented in the Appendix 6. While phase change with heat transfer process affect flow patterns, main effect on them have inertia forces and gravitation force in most cases. During boiling process more small bubbles, which does not coalesce into bigger slugs or churns could be observed, while during condensation process amount of small bubbles in fluid flow is lower. However transition from separate small bubbles to coalescing bubbles is an inertia driven process [90]. In case of occurrence of critical heat transfer during boiling all liquid film evaporate from wall surface, but this phenomenon was not examined in the study [18].

Figure 7.1 Flow structures of R1233zd(E) in 3mm horizontal pipe under saturation temperature 83°C, saturation pressure 0.71 MPa, reduced pressure p_r=0.2, and mass velocity 1000 kg/(m²s)

Figure 7.2 Flow patterns p_r=0,6 G=265 kg/(m2·s), quality respectively: 19,6%, 27%, 35,2%, 55,6%[18]

Bubbly flow is defined as discrete portions of vapour phase which do not coalesce into other forms. Slug flow is defined as much bigger portion of vapour which coalesce into slug/plug. Group of flow patterns between slug flow and annular flow as described as intermittent flow or transitional flow [14–16]. In horizontal channels intermittent flows are usually form of wavy-stratified flows and slugs. In vertical channel it is the froth flow, or elongated slugs with bubbles. Annular flow occurs when there is a liquid film on all walls and in the middle of flow there is an uninterrupted vapour core. In horizontal channel early annular flow usually have thicker portion of liquid on the bottom of the channel.

7.1. New model of flow patterns transition determination

Ability to accurately predict flow maps during two phase flows is helpful on understanding of dominant heat transfer mechanism. Multiple heat transfer predictions methods utilise different types of equations for corresponding flow regimes such as Cavallini et al. [26], Kim and Mudawar [16], El Hajal et al.[62] or Costa Party and Thome [61]. A new prediction method for determining the transition from bubbly flow to intermittent regime and from intermittent to annular flow is proposed. This method modifies the correlation developed by Revellin et al. [67]. The original correlation provided accurate predictions at lower reduced pressure values of 0.3 and 0.4, as shown in the results. This is a noteworthy result, considering the method was developed for a different fluid and test section diameter. The original correlation was based on two fluids namely R134a and R245fa at saturation temperatures 26, 30, and 35 °C with diameters of within glass tubes of 0.5 mm and 0.8 mm. However, the method proposed by Revellin does not accurately follow the trend of the annular transition line for varying reduced pressures. In fact, it suggests that annular flow occurs quicker at higher reduced pressures, which contradicts experimental data indicating the opposite trend. To address this, the Confinement number was introduced into the equation (7.1). The Confinement number accounts for the effect of gravitational forces relative to surface tension forces in liquid movement. When the significance of surface tension is higher, this criterial number decreases. Surface tension decreases with higher saturation temperatures. This adjustment allowed the transition line to adapt for all reduced pressures. Correlation for annular flow transition line was published by Głuch et al. [18]. In this work prediction method for bubbly and

intermittent flow transition has been additionally developed. Bubbly to intermittent flow transition is also modification of method propose by Revellin et al. [67]. Original form has been created only for flow boiling patterns prediction and contains Boiling number Bo. Boiling number contain heat flux in its form. When data on heat flux is not available or flow is after condensation whole equation would be equal to 0. In modification Boiling number was replaced with specific latent heat of evaporation h_{lv} and mass velocity G. Bubbly to intermittent flow transition prediction method has different form for vertical channel and horizontal channel. For vertical channel Confinement number is also added into equation (7.3) to adjust transition line to reduced pressure. For horizontal channel reduced pressure has minimal effect on transition line between bubbly and intermittent flow, and equation (7.2) for horizontal channel does not include Confinement number.

The formula developed in the present study for the transition line between bubbly flow and intermittent flow for vertical channel yields:

$$x_{b/i} = 0.028 \cdot \left(\frac{Re_{lo}}{We_{vo} * G * hlv}\right)^{0.41} \cdot Con^{-2.8} \tag{7.1}$$

The formula developed in the present study for the transition line between bubbly flow and intermittent flow for horizontal channel yields:

$$x_{b/i} = 2 \cdot \left(\frac{Re_{lo}}{We_{vo} * G * hlv}\right)^{0.41} \tag{7.2}$$

The formula developed in the present study for the transition line between intermittent flow and annular for horizontal and vertical flow yields:

$$x_{i/a} = 3.5 \cdot 10^{-7} \cdot {Re_{lo}}^{1.47} / {We_{lo}}^{1.23} \cdot Con^{-3.8} \tag{7.3}$$

7.2. Flow patterns for horizontal channel

Flow maps for 3 mm horizontal channel are presented in this section. New prediction method of intermittent/annular flow transition line is compared with 7 established methods from literature presented earlier in the state of the art chapter. These methods are due to Ong and Thome [7], Revellin and Thome [67], El Hajal et al. [62], Cheng et al. [66], Kim and Mudawar [16] and Cavallini et al. [63]. Figure 7.3 present results for the reduced pressure p_r=0.2 and two mass velocities whereas Figure 7.4 presents the flow map for mass velocity G=600 [kg/(m²·s)] and reduced pressure ranging from p_r=0.2 to p_r=0.8. New method of annular flow prediction initially developed for vertical channel is able to predict also the annular flow in a horizonal channel. Flow pattern for condensation in horizontal channel differs from patterns for boiling in a vertical channel. The most significant change is in the bubbly flow regime. For vertical channel this flow pattern is much more prominent. In horizontal channel bubbles tend to coalesce and form wavy- stratified/intermittent flow. Condensation process should also limit amount of bubbles.

New prediction method has proven ability to correctly predict annular flow transition also in horizontal channel.

7.2.1. Intermittent/annular flow transition prediction method

Comparison of correlations which predict transition from intermittent to annular flow for collected database for R1233zd(e) for vertical channel is presented in Table 7.1. Prediction method developed in this work achieved 90% accuracy. The best method which correctly predicted 100% experimental data for horizontal channel is Cavallini [63]. The second best method for collected data is Cheng et al. [66], but his method does not correctly predict data for varying mass velocity what is presented in vertical channel data in the Table 7.3.

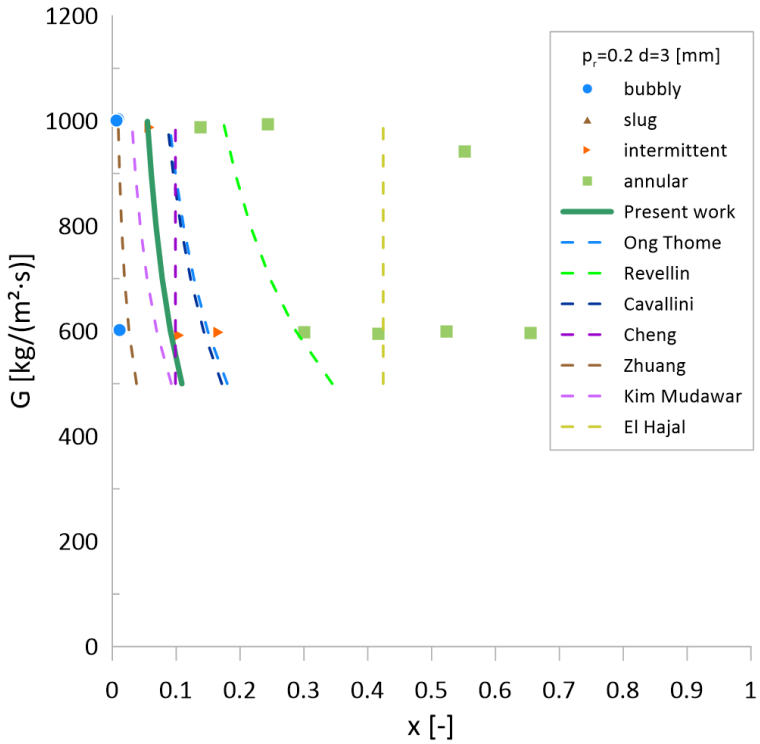

Figure 7.3 Flow map for reduced pressure p_r=0.2 with intermittent/annular transition prediction methods

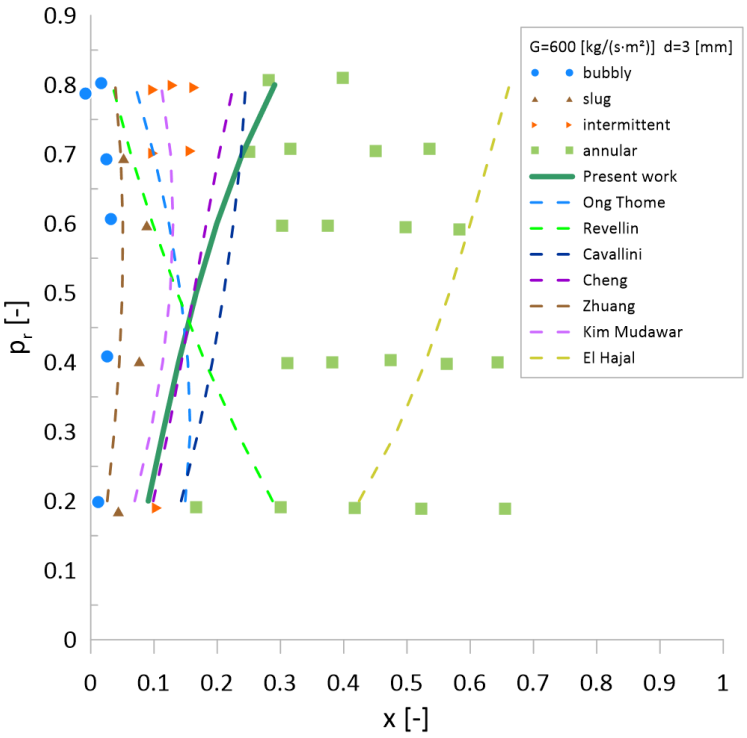

Figure 7.4 Flow map for mass velocity G=600 [kg/(m²·s)] with intermittent/annular transition prediction methods

Table 7.1 Comparison of correlations which predict transition from intermittent to annular flow for collected database for R1233zd(e) for vertical channel

Prediction method	Number of experimental data points correctly predicted	Percentage of experimental data points correctly predicted
Present work	27	90.00%
Ong and Thome [7]	26	86.67%
Revellin Thome [90]	23	76.67%
Cavallini [63]	30	100.00%
Cheng et al. [66]	104	63.80%
El Hajal et al. [62]	17	56.67%
Zhuang et al. [14]	19	63.33%
Kim and Mudawar [16]	25	83.33%

7.2.2. Bubbly/intermittent flow transition prediction method

Figure 7.5 and Figure 7.6 present comparison of bubbly/intermittent transition prediction methods. Method presented in the present work and original Revellin and Thome [67] prediction method preforms best for horizontal channel. Prediction method developed in this work is only suitable only for vertical channel. Ong and Thome [7] and Revellin and Thome [67] methods were created for flow boiling. Both of this methods incorporate Boiling number, which contains heat flux, q – without this value they would

be equal to 0. To test them against data for flow after condensation tests section small heat flux q=10 [W/m^2] was assumed.

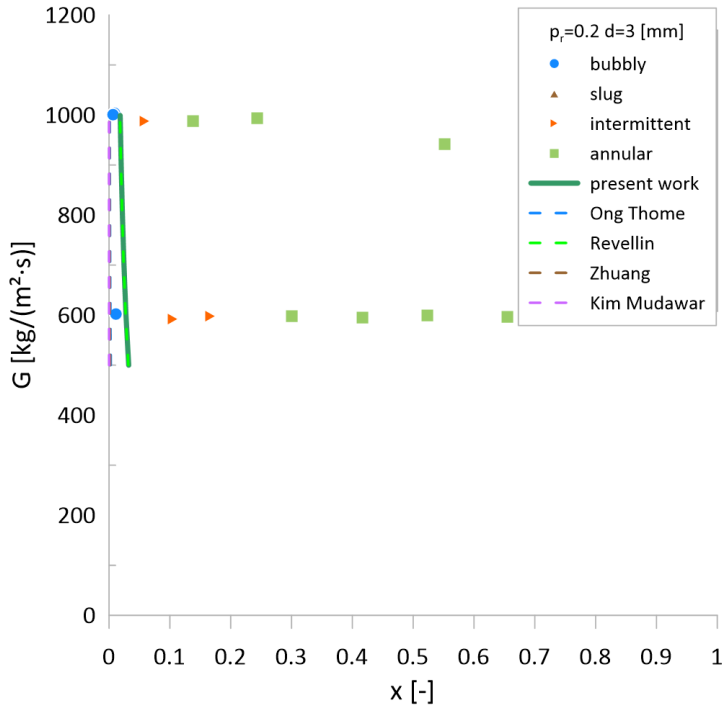

Figure 7.5 Flow map for reduced pressure p_r=0.2 with bubbly/intermittent transition prediction methods

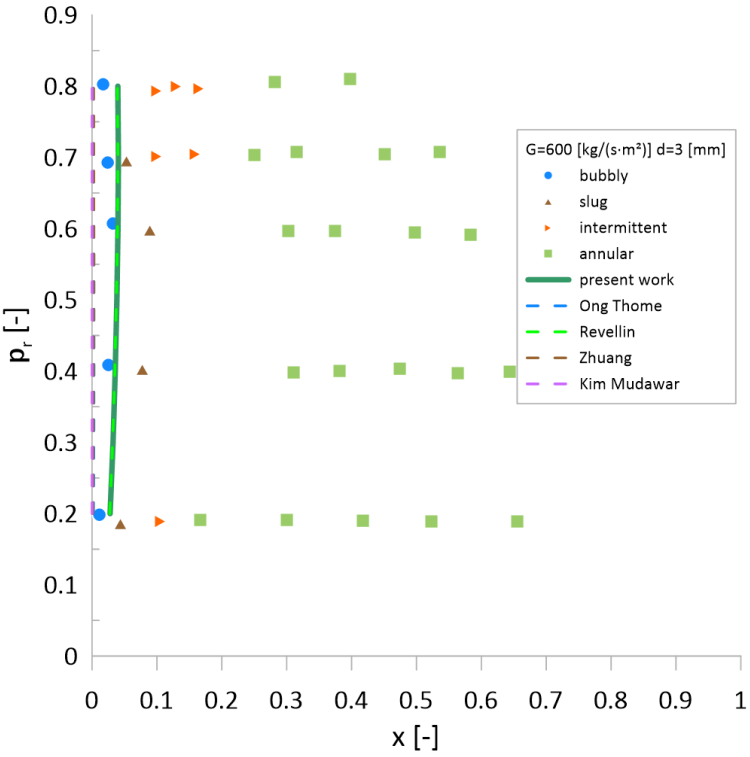

Figure 7.6 Flow map for mass velocity G=600 [kg/(m²·s)] with bubbly/intermittent transition prediction methods

7.2.3. Summary

Figure 7.7 presents a flow map with prediction methods for bubbly/intermittent and intermittent/annular transitions for horizontal channel developed in this work. Prediction method for bubbly/intermittent and method for intermittent/annular transition are developed in this work. New prediction method of intermittent/annular flow transition managed to predict flow patterns with high accuracy 90%, although Cavallini method [63] achieved a better result. 3 points which were not correctly predicted were missed only by small margin of a few percentage points what can be observed in the figures above. Prediction method for bubbly/intermittent transition achieved the same result as original Revellin and Thome [67] method, but it should be remembered that Revellin and Thome method incorporate heat flux which had to be assumed as 10 [kW/m^2]. Without this assumption this method would be equal to 0 because it was created for flow boiling. New prediction method for bubbly flow transition line achieved 100% accuracy for collected database. Table 7.3 present comparison of correlations which predict transition from bubbly to intermittent flow for collected R1233zd(e) database for the horizontal channel.

Table 7.2 Comparison of correlations which predict transition from bubbly to intermittent flow for collected R1233zd(e) database for horizontal channel

Prediction method	Number of experimental data points correctly predicted	Percentage of experimental data points correctly predicted
Present work	18	100.00%
Kim and Mudawar [16]	11	61.11%
Ong and Thome [7]	11	61.11%
Revellin and Thome [67]	18	100.00%
Zhuang [14]	11	61.11%

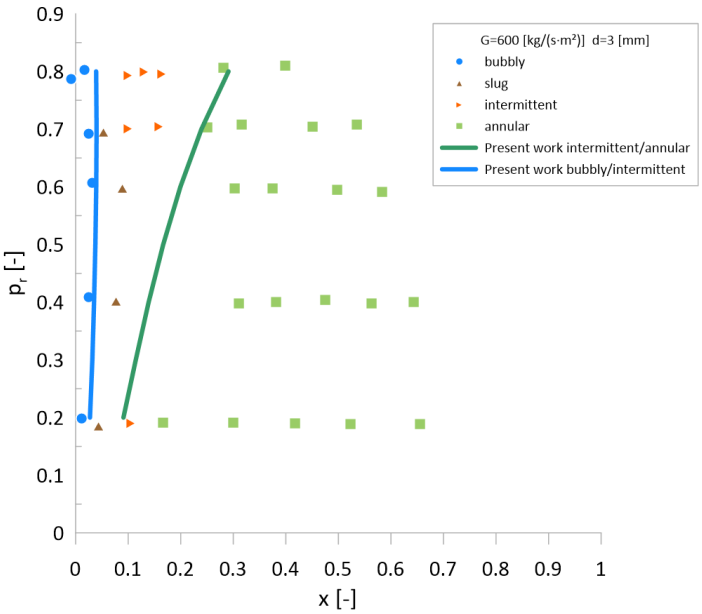

Figure 7.7 Flow map for mass velocity G=600 [kg/(m²·s)] with prediction methods for bubbly/intermittent and intermittent/annular transitions for horizontal channel

7.3. Flow patterns for vertical channel

Data for the flow maps for vertical channel was collected during experiment conducted by Głuch et al. [18] regarding flow boiling.

7.3.1. Intermittent/annular flow transition prediction method

New prediction method of intermittent/annular flow transition line is compared with 7 established methods, the same as for horizontal channel. These methods are due to Ong and Thome [7], Revellin and Thome [67], El Hajal et al. [62], Cheng et al. [66], Kim and Mudawar [16] and Cavallini et al. [63]. Flow maps for mass velocity in function of quality are presented in the Figure 7.8, Figure 7.9, Figure 7.10, Figure 7.11, Figure 7.12, Figure 7.13 and Figure 7.14. Each figure presents different reduced pressure. The most important flow map is presented in the Figure 7.15, which showcase flow patterns for different values of reduced pressure. It can be observed that only new correlation and Cavallini Correlation follow the experimental annular transition line. At low pressure most correlations works correctly, but at near critical pressures only two methods allow for prediction of the annular flow transition. The changes in the physical properties of refrigerants as the saturation temperature rises significantly affect structures and flow patterns. At high reduced pressures, the gas phase density is relatively high, and the liquid phase density is low, resulting in a small specific volume difference between the liquid and gas phases. These characteristics delay the onset of annular flow. For instance, at a reduced pressure of 0.8, annular flow was observed at 45% quality for a mass flux of 355 kg/(m²·s), whereas at a reduced pressure of 0.2, it was seen at 7% quality. Higher reduced pressures cause bubbles to appear at much higher quality levels, making nucleation a more critical heat transfer mechanism during boiling at high saturation temperatures. It is also noteworthy that annular flow occurs later at lower mass velocities. Most existing correlations for predicting annular transition lines have failed to accurately forecast the transition to annular flow at high reduced pressures, often predicting the opposite trend. They incorrectly suggested that annular flow occurs earlier at high reduced pressures, while it actually occurs later at higher saturation pressures.

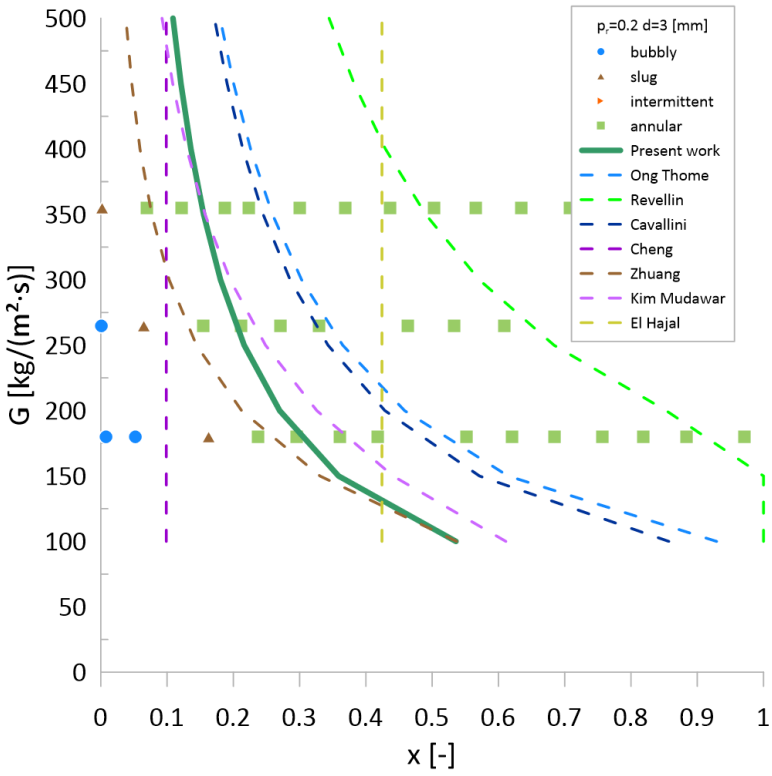

Figure 7.8 Flow map for reduced pressure p_r=0.2 with the transition lines from annular flow to intermittent flow [18]

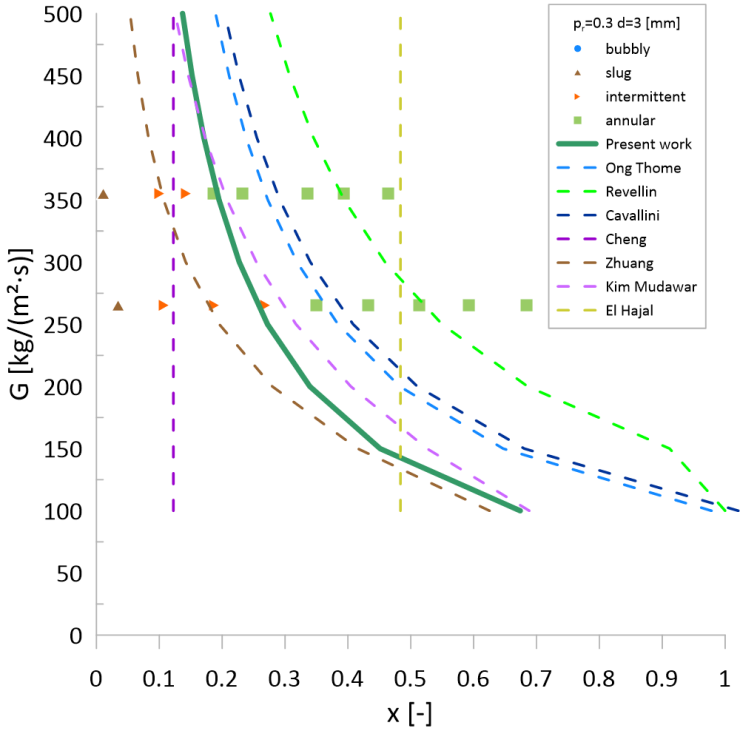

Figure 7.9 Flow map for reduced pressure p_r=0.3 with the transition lines from annular flow to intermittent flow [18]

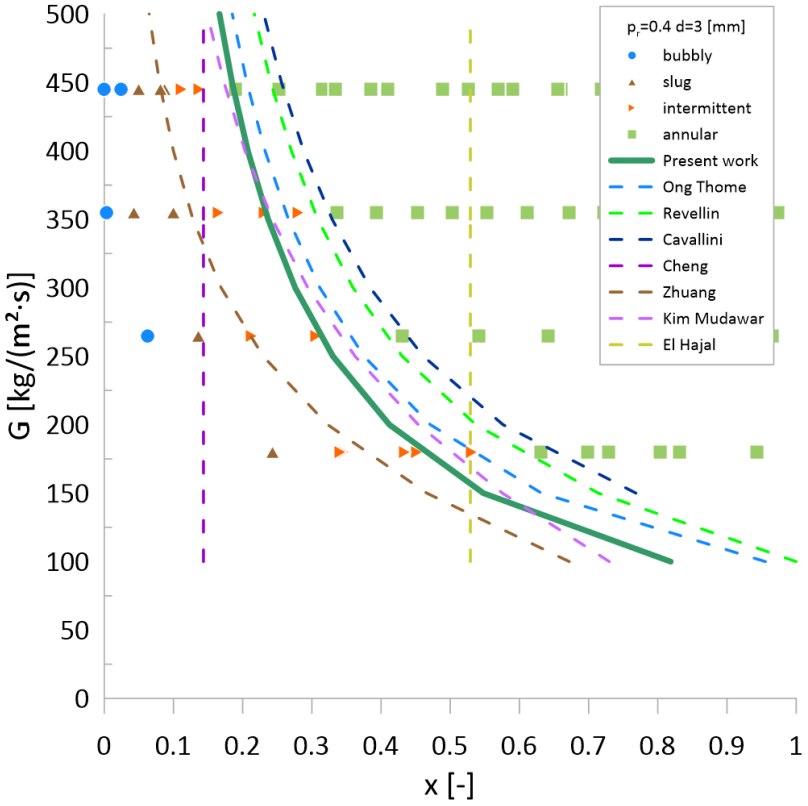

Figure 7.10 Flow map for reduced pressure p_r=0.4 with the transition lines from annular flow to intermittent flow [18]

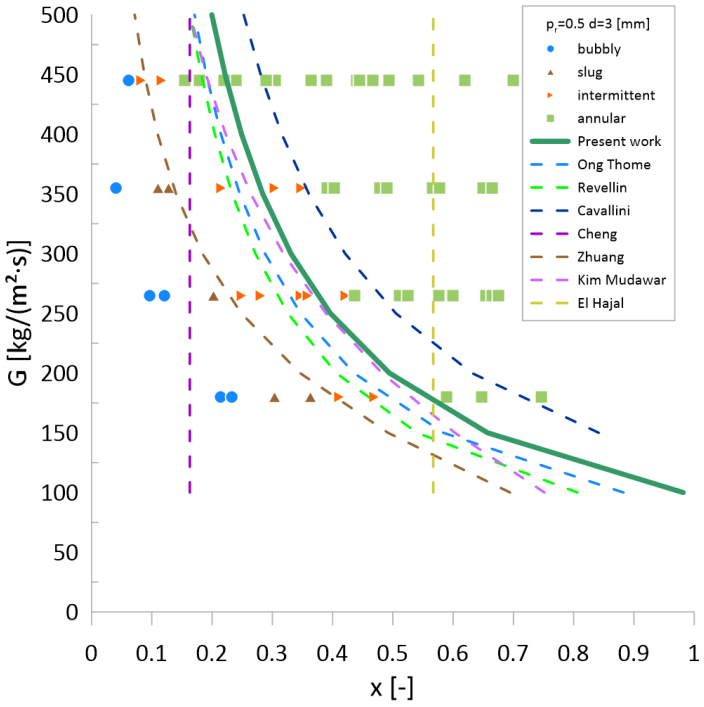

Figure 7.11 Flow map for reduced pressure p_r=0.5 with the transition lines from annular flow to intermittent flow [18]

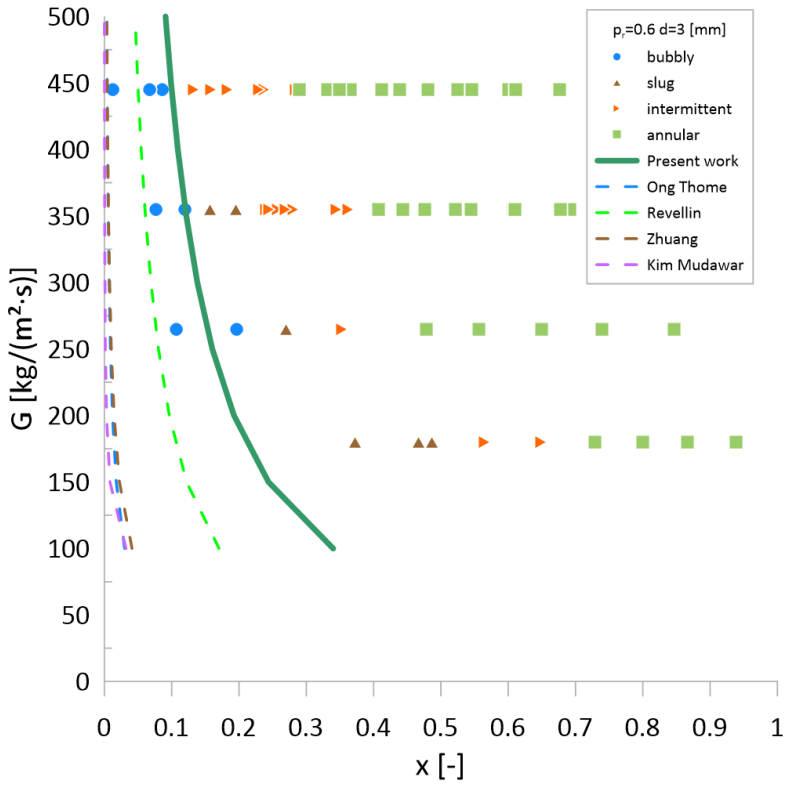

Figure 7.12 Flow map for reduced pressure p_r=0.6 with the transition lines from annular flow to intermittent flow [18]

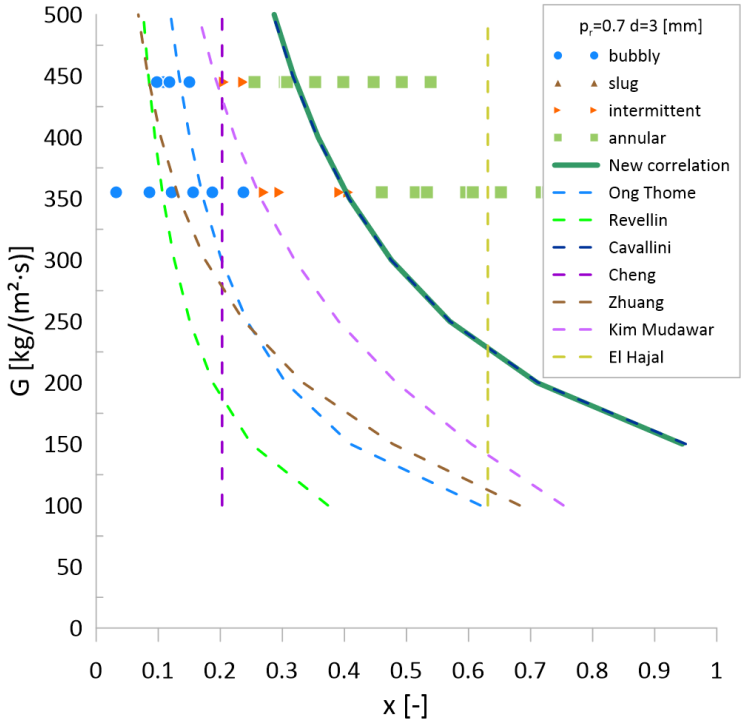

Figure 7.13 Flow map for reduced pressure p_r=0.7 with the transition lines from annular flow to intermittent flow [18]

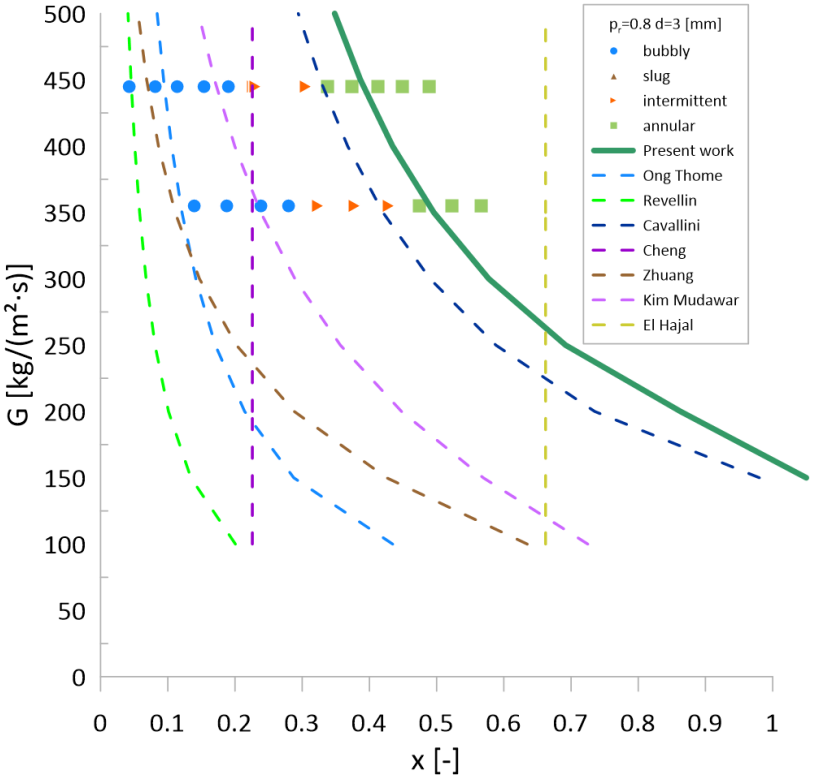

Figure 7.14 Flow map for reduced pressure p_r=0.8 with the transition lines from annular flow to intermittent flow [18]

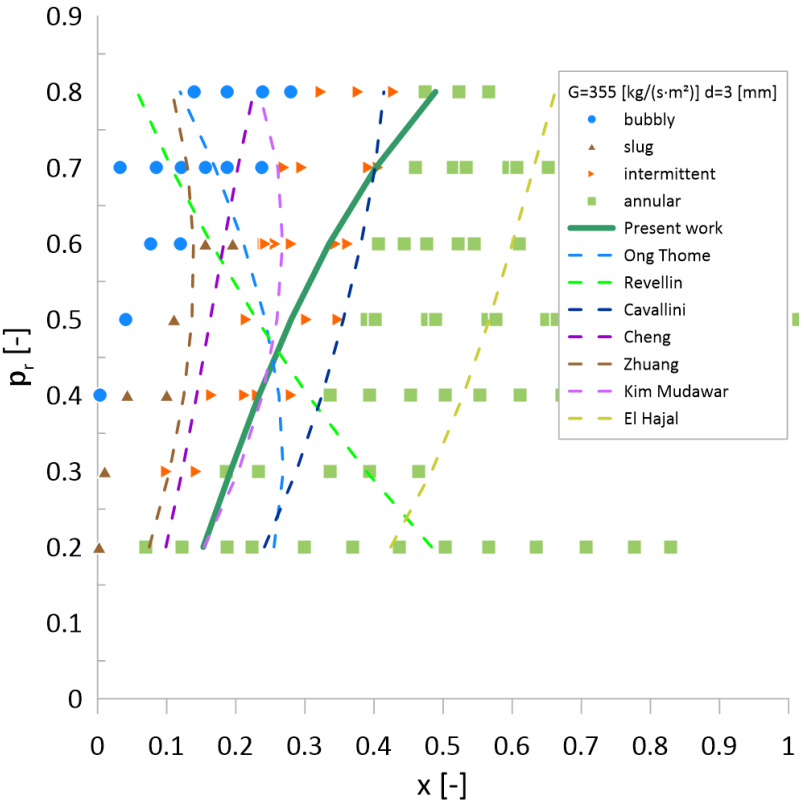

Figure 7.15 Flow map for mass velocity 355 [kg/(m²·s)] and varying reduced pressures [18]

Table 7.3 Comparison of correlations which predict transition from intermittent to annular flow for collected database for R1233zd(e) for vertical channel

Prediction method	Number of experimental data points correctly predicted	Percentage of experimental data points correctly predicted
Present work	137	84.05%
Ong and Thome [7]	105	64.42%
Revellin Thome [90]	99	60.74%
Cavallini [63]	131	80.37%
Cheng et al. [66]	104	63.80%
El Hajal et al. [62]	90	55.21%
Zhuang et al. [14]	98	60.12%
Kim and Mudawar [16]	124	76.07%

Accuracy of each method was calculated. Results are presented in Table 7.3. Database for accuracy calculations of was limited to the point in the vicinity of experimental transition region. Accuracy was defined as a number of correctly predicted experimental flow pattern points in comparison to all data points in the transition area. Developed in the thesis model achieved the best result with 84.05% points correctly predicted. The second best is Cavallini with 80.37% correctly predicted points. Other methods achieved worse results, because they did not follow experimental trends at higher pressures. The third best prediction method was developed by Kim and Mudawar, but their proposal stopped following experimental trend around 0.5 reduced pressure

7.3.2. Bubbly/intermittent flow transition prediction method

New prediction method of bubbly/intermittent flow transition line is compared with 4 methods from literature previously presented in the State of The art chapter. Figure 7.16, Figure 7.17, Figure 7.19 and Figure 7.22 present the flow maps for mass velocity in function of quality. Figure 7.23 present flow map for reduced pressure in function quality.

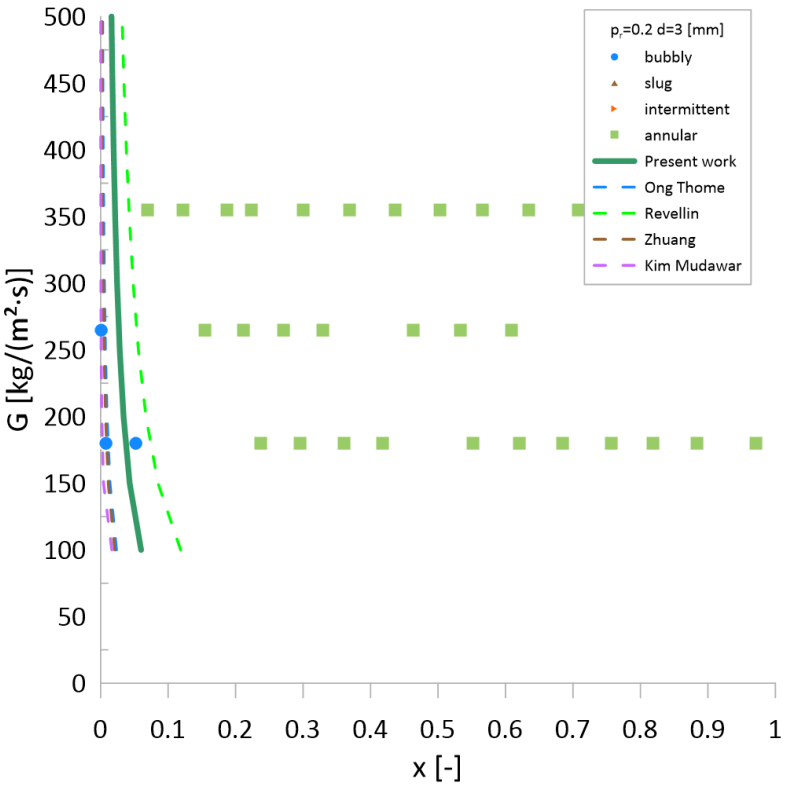

Figure 7.16 Flow map for reduced pressure pr=0.2 with the transition lines from intermittent flow to bubbly flow

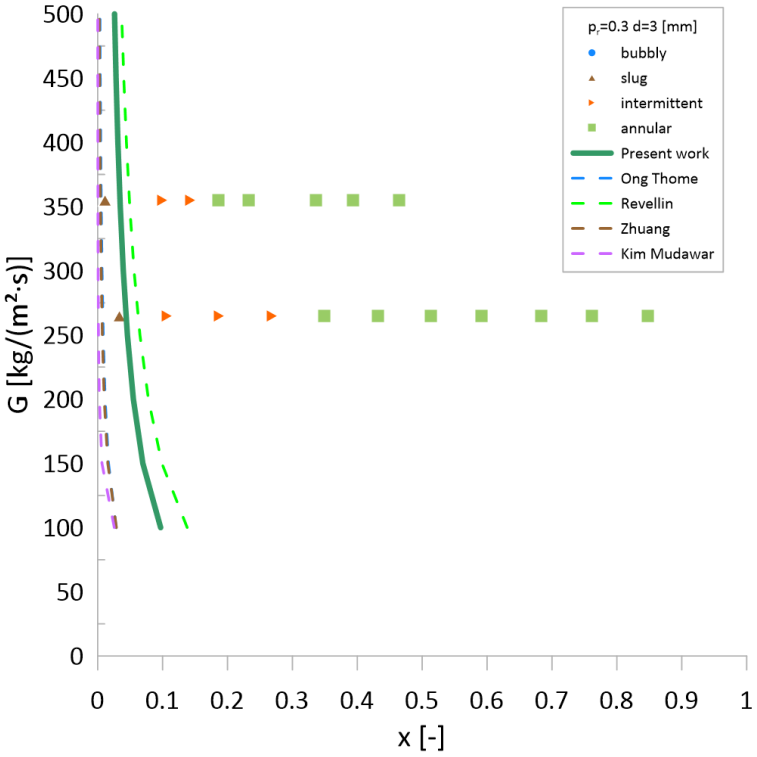

Figure 7.17 Flow map for reduced pressure pr=0.3 with the transition lines from intermittent flow to bubbly flow

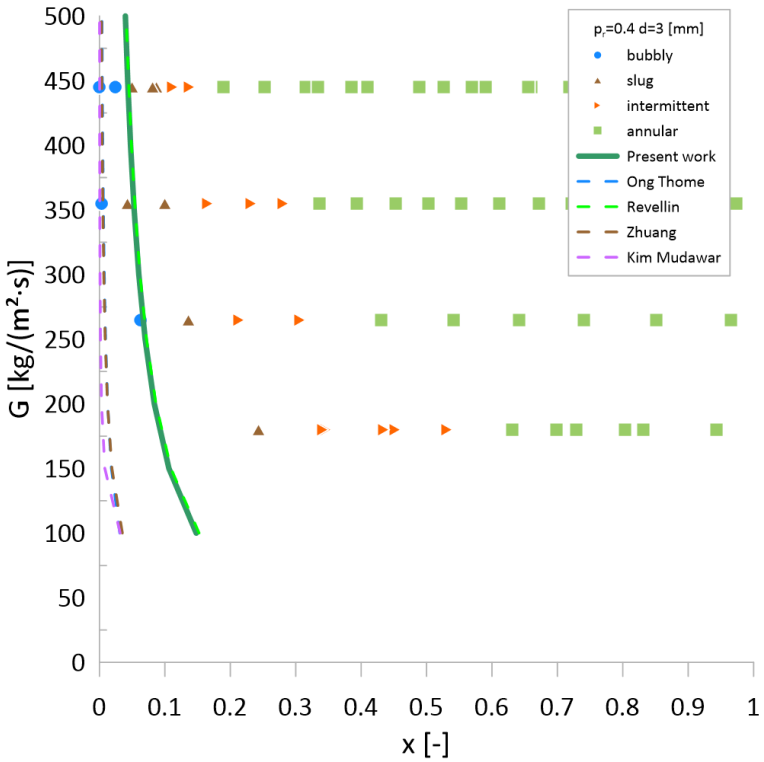

Figure 7.18 Flow map for reduced pressure pr=0.4 with the transition lines from intermittent flow to bubbly flow

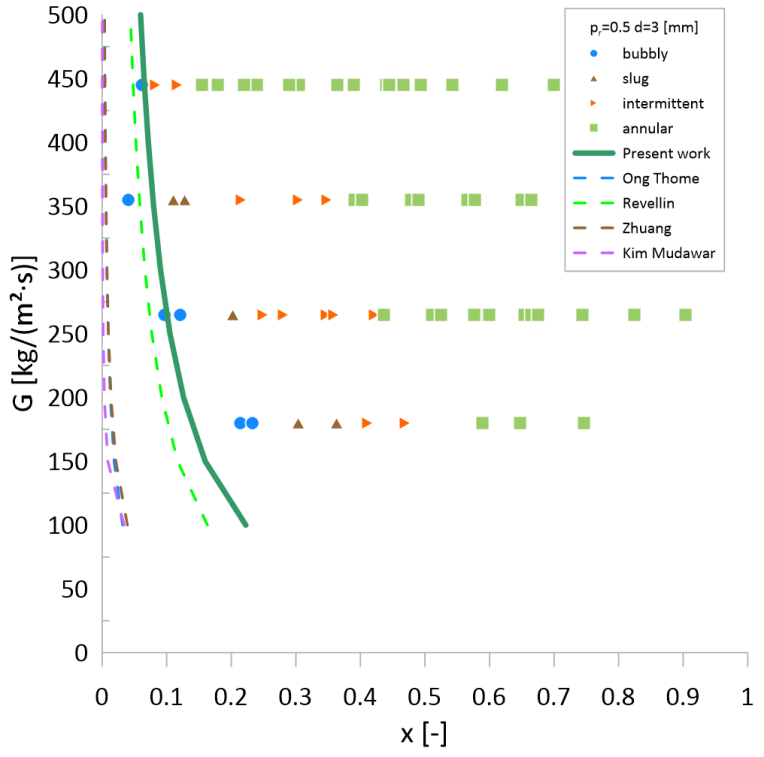

Figure 7.19 Flow map for reduced pressure pr=0.5 with the transition lines from intermittent flow to bubbly flow

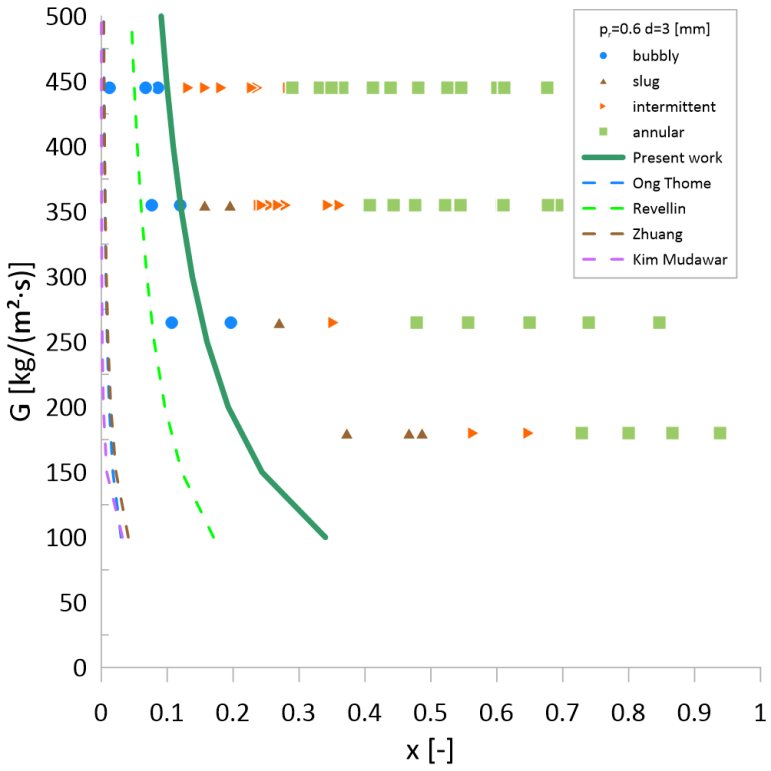

Figure 7.20 Flow map for reduced pressure pr=0.6 with the transition lines from intermittent flow to bubbly flow

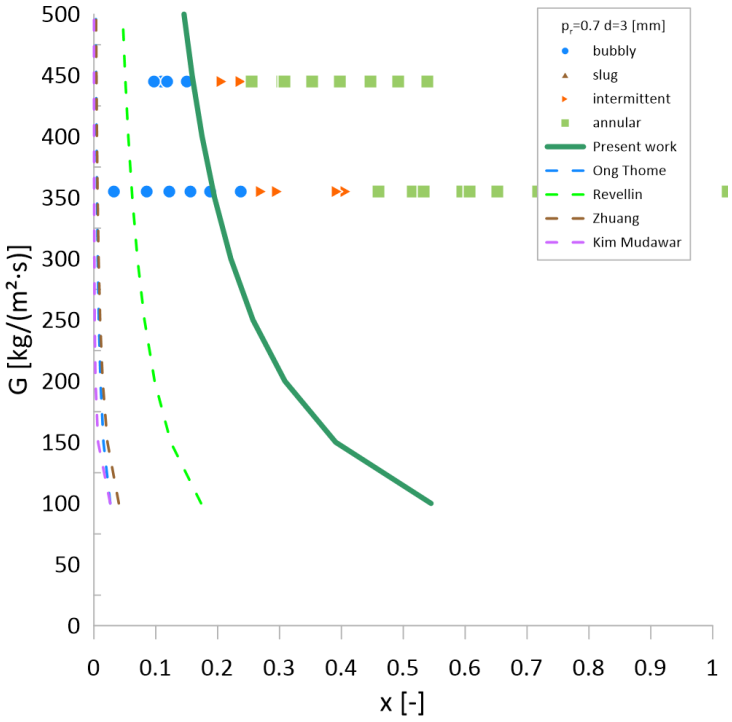

Figure 7.21 Flow map for reduced pressure pr=0.7 with the transition lines from intermittent flow to bubbly flow

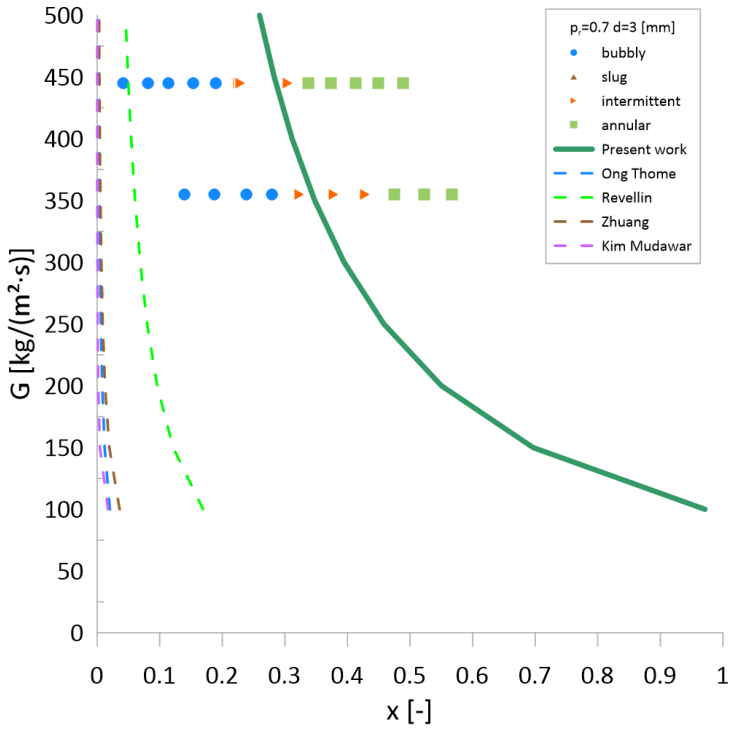

Figure 7.22 Flow map for reduced pressure pr=0.8 with the transition lines from intermittent flow to bubbly flow

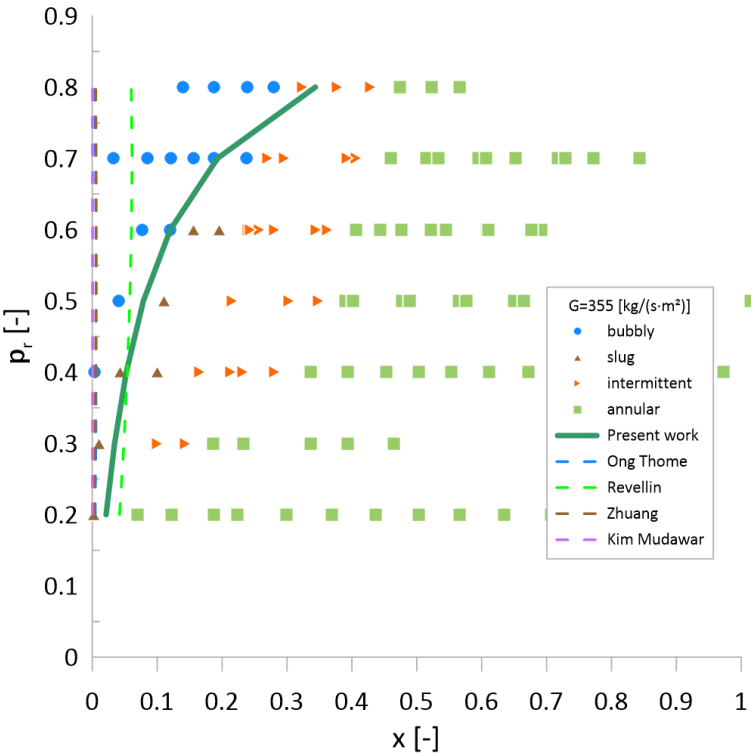

Figure 7.23 Flow map for mass velocity 355 [kg/(m²·s)] and varying reduced pressures with the transition lines from intermittent flow to bubbly flow

Table 7.4 Comparison of correlations which predict transition from bubbly to intermittent flow for collected R1233zd(e) database for vertical channel.

Prediction method	Number of experimental data points correctly predicted	Percentage of experimental data points correctly predicted
Present work	85	86.73%
Kim and Mudawar [16]	66	67.35%
Ong and Thome [7]	68	69.39%
Revellin and Thome [67]	70	71.43%
Zhuang [14]	68	69.39%

Accuracy of each bubbly flow prediction method was evaluated. Results are presented in Table 7.4. Database for accuracy calculations was limited to the points in vicinity of experimental transition region. Accuracy was defined as a number or correctly predicted experimental flow pattern points in comparison to all data points in the transition area. New correlation achieved the best result with 86.73% points correctly predicted. Other methods achieved worse results, because they did not follow experimental trends at higher pressures. All of them were created for horizontal channels.

7.3.3. Summary

Figure 7.24 presents the flow map with the best prediction methods for bubbly/intermittent and intermittent/annular transitions for vertical channel from analysed methods. The best prediction methods for bubbly/intermittent and for intermittent/annular transition are developed in this work what can be observed in the figures and tables above.

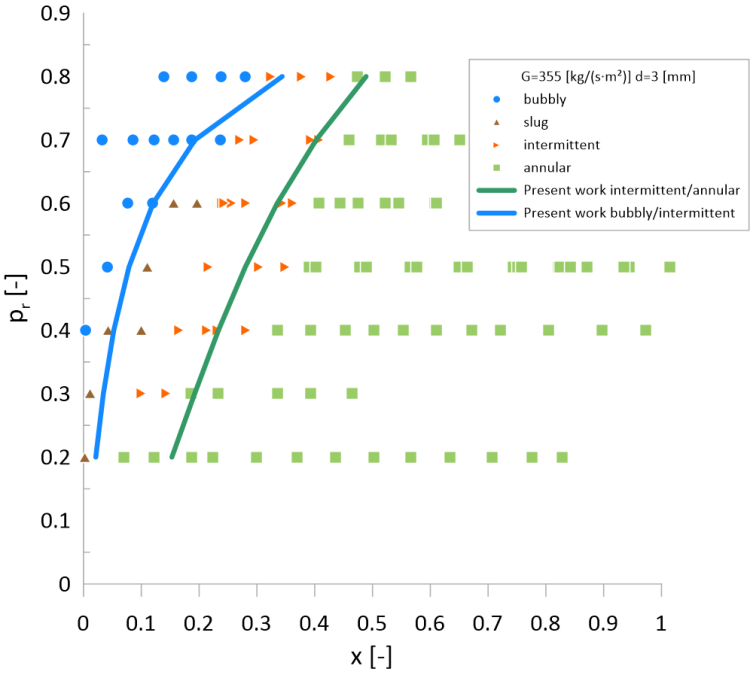

Figure 7.24 Flow map for mass velocity G=355 [kg/(m²·s)] with the best prediction methods for bubbly/intermittent and intermittent/annular transitions for horizontal channel

7.4. Validation of transition between intermittent and annular flow prediction method on flows maps collected from literature

Key feature on a new prediction method of annular flow transition is the ability to predict transition line in varying values of saturation pressure. Three data sources have been collected, namely due to Charnay et al. [15] for R245fa, Billet et al.[69] for R245fa. and Zhuang et al. [14] for ethene-R170. New annular flow prediction method developed in this thesis is able to follow experimental trends for collected database. The best compatibility is observed for Charnay et al. flow map. Cavallini [63] prediction method and Kim and Mudawar [16] method also are able to predict annular flow transition. All three collected flow maps were collected for horizontal channel. Charnay et al. [15] and Billet et al.[69] collected data only for two flow regions – intermittent flow and annular flow. Because of that only the method for intermittent/annular flow transition is compared against experimental data collected by Charnay et al. [15] and Billet et al.[69]. For Zhuang et al. [14] prediction method of bubbly/intermittent flow transition presented in this work achieved equally good to method proposed by Revellin and Thome [67], but their method required assumption of heat flux q=10 [kW/m^2], because Zhuang et al. created flow map for flow condensation.

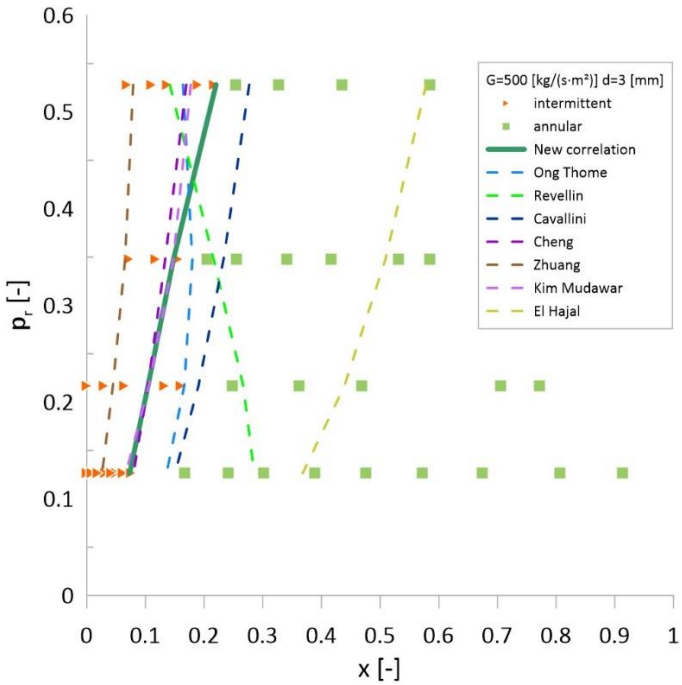

Figure 7.25 Flow map for mass velocity G=500 [kg/(m²·s)] flowing in horizontal channel for R245fa Charnay et al. [15,91] with intermittent/annular flow transition prediction methods

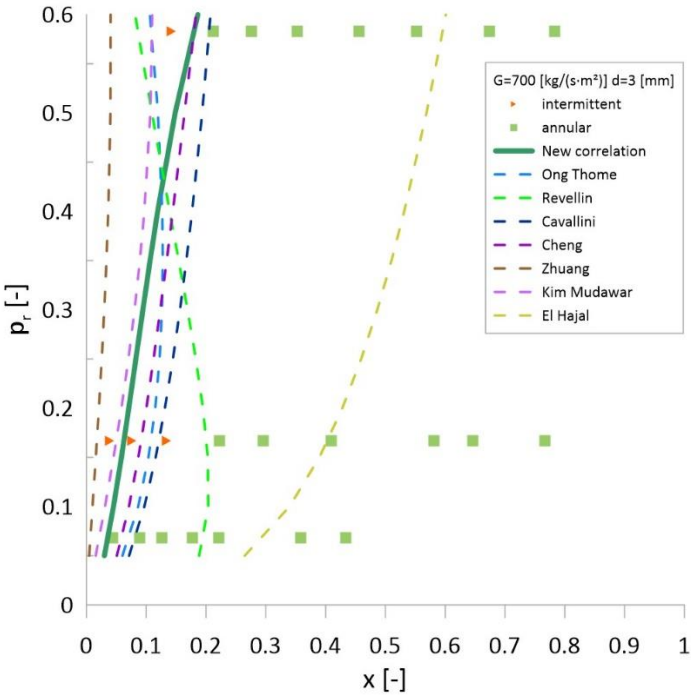

Figure 7.26 Flow map for mass velocity G=700 [kg/(m²·s)] in horizontal channel R245fa Billiet et al.[69] with intermittent/annular flow transition prediction methods

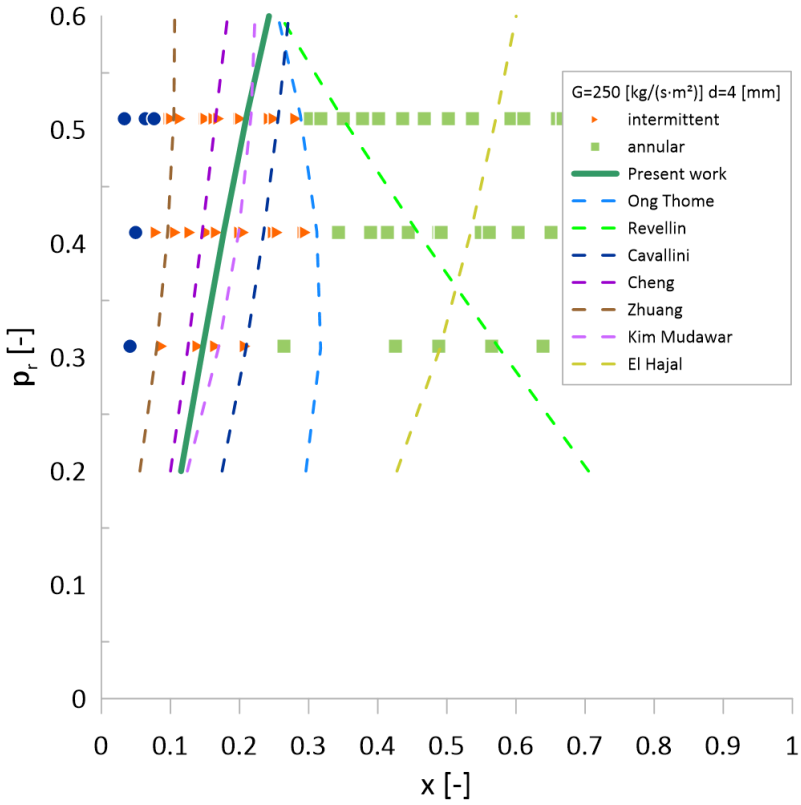

Figure 7.27 Flow map for mass velocity G=250 [kg/(m²·s)] in horizontal channel R170 Zhuang et al. [14] with intermittent/annular flow transition prediction methods

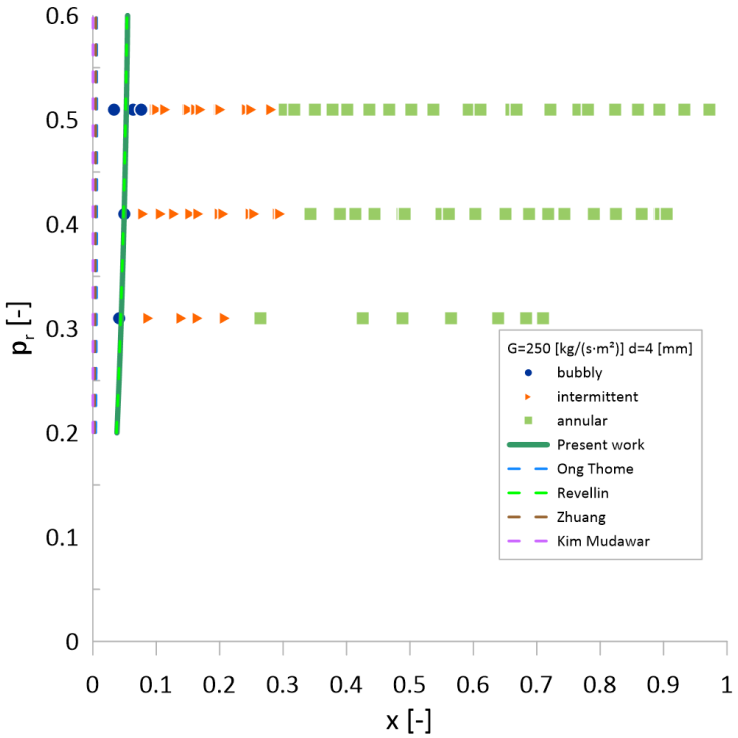

Figure 7.28 Flow map for mass velocity G=250 [kg/(m²·s)] in horizontal channel R170 Zhuang et al. [14] with bubbly/intermittent flow transition prediction methods

7.5. Summary

New prediction method for bubbly/intermittent flow and intermittent/annular flow transitions are presented in equations (7.1), (7.2) and (7.3). Method for prediction of bubbly/intermittent transition has distinct forms for vertical and horizontal channel whereas prediction of intermittent/annular flow transition is suitable for both vertical and horizontal channel. Summary for prediction of annular flow transition inside horizontal and vertical channel is presented in Table 7.5. Summary for prediction of bubbly flow transition inside horizontal and vertical channel is presented in Table 7.6. Overall the best method for prediction of intermittent/annular flow transition is the one developed in this work. The best prediction method for bubbly/intermittent flow transition is the one developed in this work. Revellin and Thome [90] prediction method of bubbly/intermittent transition in horizontal channel achieved equally good results as the one presented in this work. It should be remembered that for this prediction method heat flux is q=10 [kW/m^2], had to be assumed because without this values results given by correlation would be equal to 0. Cavallini [63] prediction method of annular flow transition achieved slightly worse result than the one presented in this work.

Table 7.5 Comparison of correlations which predict transition from intermittent to annular flow for collected database for R1233zd(e) for horizontal and vertical channel

Prediction method	Number of experimental data points correctly predicted	Percentage of experimental data points correctly predicted
Present work	164	84.97%
Ong and Thome [7]	131	67.88%
Revellin Thome [90]	122	63.21%
Cavallini [63]	161	83.42%
Cheng et al. [66]	133	68.91%
El Hajal et al. [62]	107	55.44%
Zhuang et al. [14]	117	60.62%
Kim and Mudawar [16]	149	77.20%

Table 7.6 Comparison of correlations which predict transition from bubbly to intermittent flow for collected database for R1233zd(e) for horizontal and vertical channel

Prediction method	Number of experimental data points correctly predicted	Percentage of experimental data points correctly predicted
Present work	103	88.79%
Ong and Thome [7]	79	68.10%
Revellin Thome [90]	88	75.86%
Zhuang et al. [14]	79	68.10%
Kim and Mudawar [16]	77	66.38%

Figure 7.29 and Figure 7.30 present shape of transition lines between bubbly and intermittent flow due to prediction method developed in this work for varying reduced pressure $p_{r,}$ whereas Figure 7.31 presents shape of transition lines between intermittent and annular flow. Effect of reduced pressure can be observed for annular flow transition prediction method and for bubbly flow transition prediction method for horizontal channel, whereas reduced pressure has minimal effect on bubbly flow transition lines inside horizontal channel.

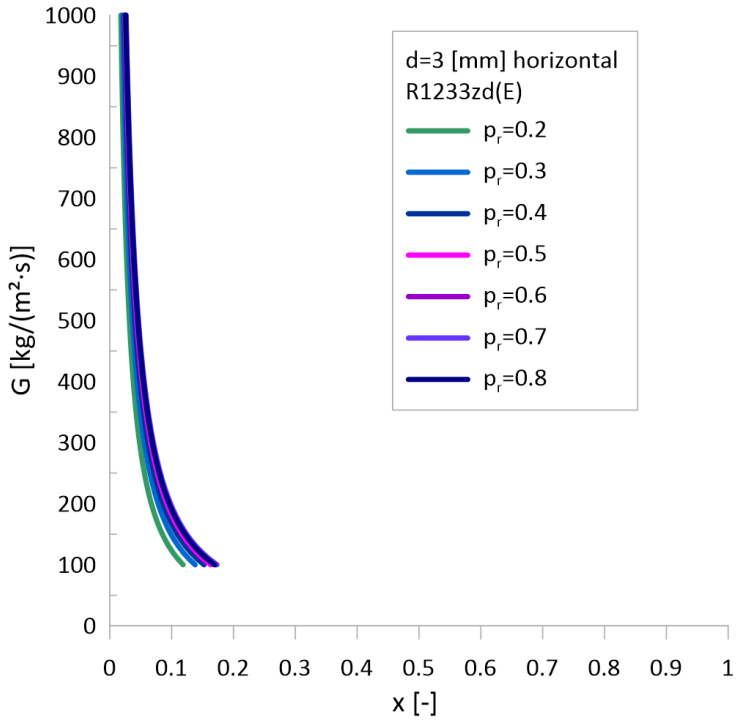

Figure 7.29 Shape of transition lines between bubbly and intermittent flow due to prediction method developed in this work for varying reduced pressure p_r for d=3 [mm] horizontal channel and R1233zd(E)

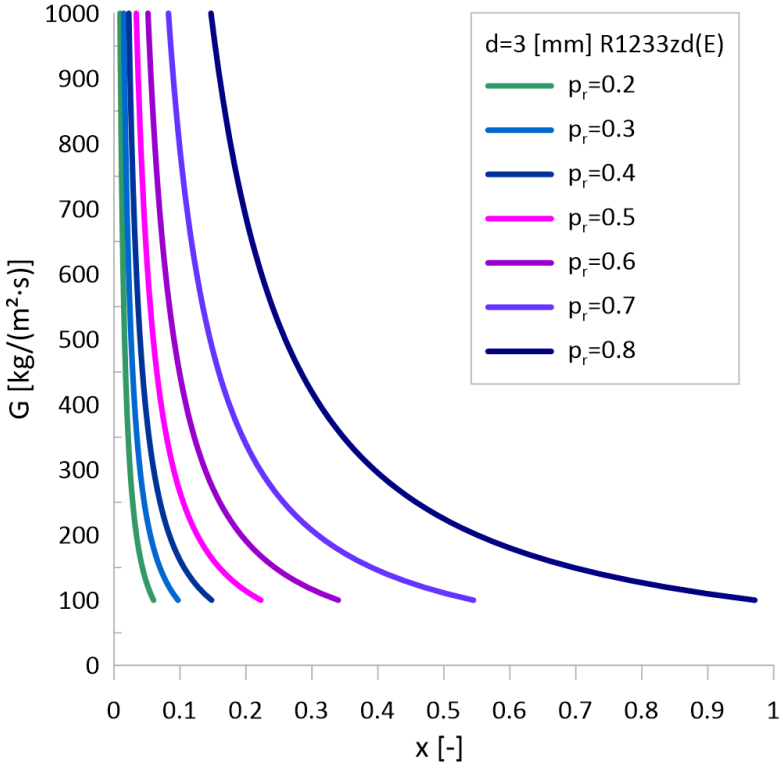

Figure 7.30 Shape of transition lines between bubbly and intermittent flow due to prediction method developed in this work for varying reduced pressure p_r for d=3 [mm] vertical channel and R1233zd(E)

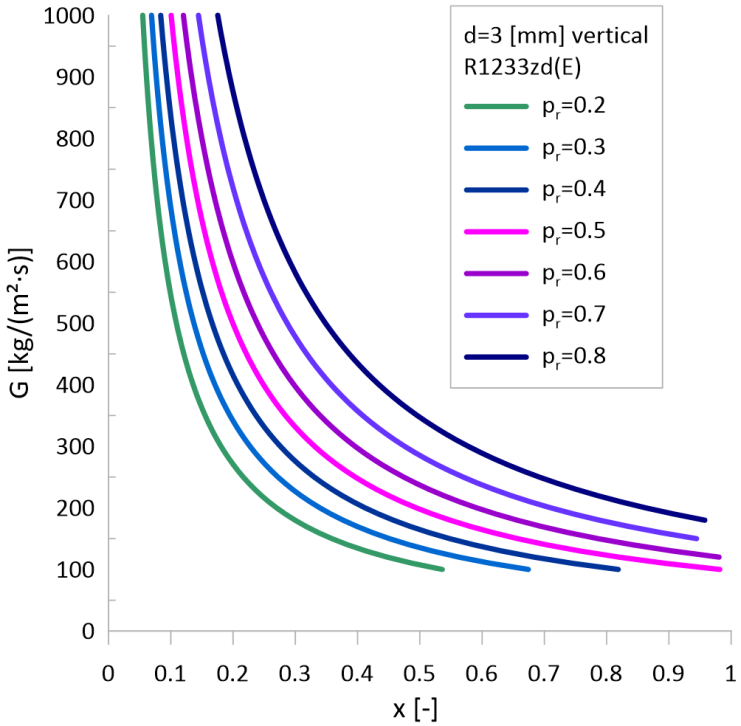

Figure 7.31 Shape of transition lines between intermittent and annular flow due to prediction method developed in this work for varying reduced pressure p_r for d=3 [mm] horizontal and vertical channel and R1233zd(E)

8. Conclusions and recommendations for future work

An extensive study of flow condensation at medium and high reduced pressure has been conducted. In the range of activities accomplished in this work the experimental facility originally developed for flow boiling has been modified to studies of flow condensation, assembled and commissioned. Experimental database for flow condensation of R1233zd(E) for low medium and high values of reduced pressure has been collected. This experiment is a pioneering research which investigated refrigerant condensation process at temperatures higher than 100°C. Range of examined parameters is from 0.2 reduced pressure to 0.8 reduced pressure, what corresponds to saturation temperatures ranging from 82°C to 153°C. Saturation pressures covered range from 7 bar to 28.5 bar. Conduction of experiment as such high parameters renders multiple challenges. Test rig has to be constructed to safely operate at high temperature and high pressure conditions simultaneously. Many elements such as condensation test section and visualization test section have to be designed and custom built from high quality materials to withstand higher than usual operating pressure conditions. Thermal expansion of tubes and other elements has to be accounted at the design process of the experimental facility. Most material used for sealing purpose tend to react with refrigerants at increased temperature conditions. PTFE can safely operate at 40°C, but above 100°C it tends to degrade. Because of that sealants have to be checked and replaced regularly. All heat loses have to be carefully examined, because results are much more prone to be affected by systematic errors when temperature difference between working medium and ambient is very high.

Collected also has been an extensive database from literature on flow condensation heat transfer accounting to 4700 data points for 21 working fluids from 28 data sources covering the range of reduced pressures from 0.1 to 0.9. Mass velocity varies from 75 to 1400 [kg/(s·m²)] for tubes from the range from 0.76 mm to 15 mm. Experiments were conducted for temperatures ranging from -107 to 91°C. This data has been used for modification and validation of the in-house prediction model which has been additionally modified to be capable of considering the effect of reduced pressure. A revised in-house Mikielewicz model for predicting heat transfer coefficients during the condensation of natural refrigerants, with a focus on high reduced pressure values, has been proposed. This model aims to achieve high accuracy while maintaining a simple structure. The modification involves adjusting the two-phase flow multiplier in the in-house model using an updated Confinement number. This has led to significant improvements, especially at high reduced pressure values. The modelling relied on a comprehensive database of experimental measurements, containing 4700 data points for 26 natural and synthetic refrigerants. The database covers reduced pressures from 0.1 to 0.9, channel internal diameters from 0.76 mm to 15 mm, and mass velocities from 75 to 1400 kg/(m²·s). It also considers the full range of quality distribution from 0% to 100%. When compared with 7 other models from the literature, the new method achieved the lowest mean absolute percentage error MAPE for turbulent flows, reduced pressures above 0.5 and for natural refrigerants.

A significant originality of the work comes from the fact of employing Artificial Neural Network (ANN) for the sake of determination of HTC. Model to predict the heat transfer coefficient during flow condensation using a Feedforward Neural Network (FNN) has been developed. This method was trained on a comprehensive experimental database with 3969 data points, encompassing a range of diameters, mass velocities, and reduced pressures from 0.1 to 0.9. Unused sets of data points were scheduled for additional testing and validation. The proposed FNN demonstrated excellent performance on randomly selected data points. The FNN design includes 5 hidden layers and employs ReLu and linear activation functions, trained using the ADAM algorithm. For the first variant, the Mean Absolute Error (MAE) is 466.52, and the Mean Absolute Percentage Error (MAPE) is 11.76%. The second variant achieved MAE 386.28 and an MAPE of 10.12%, with the latter MAPE being lower than the measurement uncertainty in most experiments. Despite its relatively small size, the FNN yielded good results. Developed model was tested on separate database excluded from training data to further validate chosen methodology. In this case first variant failed to accurately predict data, but second variant MAE 703.47 and MAPE 21.19% what is very good result.

The variation in the physical properties of refrigerants with increasing saturation temperature significantly affects structures and flow patterns. At high reduced pressures, the gas phase density is relatively high, and the liquid phase density is low, resulting in a small difference between the liquid and gas phases. These characteristics delay the onset of annular flow. Annular flow occurs later at lower mass velocities for high saturation pressure. A new correlation for the annular flow transition line has been developed, accurately predicting the transition from intermittent to annular flow for all measured reduced pressures and mass velocities. This new correlation correctly predicted 84.97% of the collected experimental data points, outperforming all other tested correlations. Previous correlations for predicting annular transition lines failed to accurately forecast the flow pattern transition to annular flow at high reduced pressures, often predicting the opposite trend by suggesting that annular flow occurs sooner at higher reduced pressures. Developed has been also new correlation for bubbly flow transition line. Predictions using that model achieved 88.79% accuracy for the collected database.

Future research should aim to expand the experimental database for high saturation temperatures. Data for more mass velocities and different channel diameters should be collected. Different channel shapes such as square or minigap should also be tested. Upflow and downflow characteristics in vertical channel could be examined. Experimental data for varying inclination angle also should be collected. Studies on heat transfer intensification methods will be useful for construction of heat pumps, because of smaller heat transfer condensation coefficient at high values of reduced pressure. Same conclusion relates to power engineering condensers operating close to thermodynamic critical point. Methods for flow pattern recognition data could be created as a helpful tool in denoting a proper structure of the flow. Experimental database from literature could be collected to enhance and further validate prediction method based on the Feedforward Neural Network. It must be remembered that data collected from different experimental facilities is prone to systematic errors of those facilities. It happens sometimes

that even in case of the same fluid, same flow conditions, and other distinct parameters the obtained pressure drop data and heat transfer data may differ substantially. In such situation training of the neural network is not very reliable.

BIBLIOGRAPHY

[1] Ghiaasiaan, S. M. (2008). *Two-phase flow, boiling and condensation in conventional and miniature systems*. Cambridge University Press.

[2] Shah, M. M. (2018). Applicability of Correlations for Boiling/Condensing in Macrochannels to Minichannels. *Heat and Mass Transfer Research Journal*, *2*(1). http://cansrg.com/journals/hmtrj/

[3] Kandlikar, S. G. (2002). Fundamental issues related to flow boiling in minichannels and microchannels. *Experimental Thermal and Fluid Science*, *26*(2–4), 389–407. https://doi.org/10.1016/S0894-1777(02)00150-4

[4] Mehendafe, S. S., Jacobi, A. M., & Shah, R. K. (2000). Fluid flow and heat transfer at micro- and meso-scales with application to heat exchanger design. *Applied Mechanics Reviews*, *53*(7), 175–193. https://doi.org/10.1115/1.3097347

[5] Kew, P. A., & Cornwell, K. (1997). Correlations for the prediction of boiling heat transfer in small-diameter channels. *Applied Thermal Engineering*, *17*(8–10), 705–715. https://doi.org/10.1016/s1359-4311(96)00071-3

[6] Ong, C. L., & Thome, J. R. (2011). Macro-to-microchannel transition in two-phase flow: Part 2 - Flow boiling heat transfer and critical heat flux. *Experimental Thermal and Fluid Science*, *35*(6), 873–886. https://doi.org/10.1016/j.expthermflusci.2010.12.003

[7] Ong, C. L., & Thome, J. R. (2011). Macro-to-microchannel transition in two-phase flow: Part 1 - Two-phase flow patterns and film thickness measurements. *Experimental Thermal and Fluid Science*, *35*(1), 37–47. https://doi.org/10.1016/j.expthermflusci.2010.08.004

[8] Triplett, K. A., Ghiaasiaan, S. M., Abdel-Khalik, S. I., & Sadowski, D. L. (1999). Gas-liquid two-phase flow in microchannels part I: Two-phase flow patterns. *International Journal of Multiphase Flow*, *25*(3), 377–394. https://doi.org/10.1016/S0301-9322(98)00054-8

[9] Harirchian, T., & Garimella, S. V. (2010). A comprehensive flow regime map for microchannel flow boiling with quantitative transition criteria. *International Journal of Heat and Mass Transfer*, *53*(13–14), 2694–2702. https://doi.org/10.1016/j.ijheatmasstransfer.2010.02.039

[10] Li, W., & Wu, Z. (2010). A general criterion for evaporative heat transfer in micro/mini-channels. *International Journal of Heat and Mass Transfer*, *53*(9–10), 1967–1976. https://doi.org/10.1016/j.ijheatmasstransfer.2009.12.059

[11] Ullmann, A., & Brauner, N. (2007). The prediction of flow pattern maps in minichannels. *Multiphase Science and Technology*, *19*(1), 49–73. https://doi.org/10.1615/MultScienTechn.v19.i1.20

[12] Thome, J. R., & Cioncolini, A. (2015). *Encyclopedia of Two-Phase Heat Transfer and Flow* (J. R. Thome, Ed.; I, Issue October, pp. 47–84). World Scientific Publishing. Chapter. https://doi.org/10.1142/9789814623216_0020

[13] Soliman, H. M. (1982). On the annular-to-wavy flow pattern transition during condensation inside horizontal tubes. *The Canadian Journal of Chemical Engineering*, *60*(4), 475–481. https://doi.org/10.1002/cjce.5450600405

[14] Zhuang, X., Gong, M., Chen, G., Zou, X., & Shen, J. (2016). Two-phase flow pattern map for R170 in a horizontal smooth tube. *International Journal of Heat and Mass Transfer*, *102*, 1141–1149. https://doi.org/10.1016/j.ijheatmasstransfer.2016.06.094

[15] Charnay, R., Bonjour, J., & Revellin, R. (2014). Experimental investigation of R-245fa flow boiling in minichannels at high saturation temperatures: Flow patterns and flow pattern maps. *International Journal of Heat and Fluid Flow*, *46*, 1–16. https://doi.org/10.1016/j.ijheatfluidflow.2013.12.002

[16] Kim, S. M., & Mudawar, I. (2012). Flow condensation in parallel micro-channels - Part 2: Heat transfer results and correlation technique. *International Journal of Heat and Mass Transfer*, *55*(4), 984–994. https://doi.org/10.1016/j.ijheatmasstransfer.2011.10.012

[17] Da Silva Lima, R. J. (2011). *Experimental and Visual Study on Flow Patterns and Pressure Drops in U-Tubes* [EPFL]. https://doi.org/https://doi.org/10.5075/epfl-thesis-5038

[18] Głuch, S., Pysz, M., & Mikielewicz, D. (2023). Flow maps and flow patterns of R1233zd(E) in a circular minichannel at low, medium and high values of saturation pressure. *36th International Conference on Efficiency, Cost, Optimization, Simulation and Environmental Impact of Energy Systems, ECOS 2023*, 402–413. https://doi.org/10.52202/069564-0037

[19] Garimella, S., & Bandhauer, T. (2001). *Measurement of Condensation Heat Transfer Coefficients in Microchannel Tubes*. 243–249. https://doi.org/10.1115/IMECE2001/HTD-24221

[20] Jiang, Y. (2004). *Heat transfer and pressure drop of refrigerant R404A at near-critical and supercritical pressures*. Iowa State University. https://dr.lib.iastate.edu/server/api/core/bitstreams/2fabe648-4a38-47e9-abd9-18931473f76b/content

[21] Milkie, J. A. (2014). *Condensation of hydrocarbons and zeotropic hydrocarbon/refrigerant mixtures in horizontal tubes*.

[22] Keinath, B. (2012). *Void Fraction, Pressure Drop, and Heat Transfer in High Pressure Condensing Flows through Microchannels*. *December*, 1–353.

[23] Macdonald, M., & Garimella, S. (2016). Hydrocarbon condensation in horizontal smooth tubes: Part i - Measurements. *International Journal of Heat and Mass Transfer*, *93*, 75–85. https://doi.org/10.1016/j.ijheatmasstransfer.2015.09.018

[24] Macdonald, M., & Garimella, S. (2016). Hydrocarbon condensation in horizontal smooth tubes: Part II - Heat transfer coefficient and pressure drop modeling. *International Journal of Heat and Mass Transfer*, *93*, 1248–1261. https://doi.org/10.1016/j.ijheatmasstransfer.2015.09.019

[25] Cavallini, A., Bortolin, S., Del Col, D., Matkovic, M., & Rossetto, L. (2011). Condensation heat transfer and pressure losses of high- and low-pressure refrigerants flowing in a single circular minichannel. *Heat Transfer Engineering*, *32*(2), 90–98. https://doi.org/10.1080/01457631003769104

[26] Cavallini, A., Del Col, D., Doretti, L., Matkovic, M., Rossetto, L., Zilio, C., & Censi, G. (2006). Condensation in horizontal smooth tubes: A new heat transfer model for heat exchanger design. *Heat Transfer Engineering*, *27*(8), 31–38. https://doi.org/10.1080/01457630600793970

[27] Del Col, D., Bortolin, S., Cavallini, A., & Matkovic, M. (2011). Effect of cross sectional shape during condensation in a single square minichannel. *International Journal of Heat and Mass Transfer*, *54*(17–18), 3909–3920. https://doi.org/10.1016/j.ijheatmasstransfer.2011.04.035

[28] Zhuang, X. R., Gong, M. Q., Zou, X., Chen, G. F., & Wu, J. F. (2016). Experimental investigation on flow condensation heat transfer and pressure drop of R170 in a horizontal tube. *International Journal of Refrigeration*, *66*, 105–120. https://doi.org/10.1016/j.ijrefrig.2016.02.010

[29] Aroonrat, K., & Wongwises, S. (2017). Experimental study on two-phase condensation heat transfer and pressure drop of R-134a flowing in a dimpled tube. *International Journal of Heat and Mass Transfer*, *106*, 437–448. https://doi.org/10.1016/j.ijheatmasstransfer.2016.08.046

[30] Cavallini, A., Censi, G., Col, D. Del, Doretti, L., Longo, G. A., & Rossetto, L. (2001). *Experimental investigation on condensation heat transfer and pressure drop of new HFC refrigerants in a horizontal smooth tube Â rimentale sur le transfert de chaleur lors de la Etude expe condensation et sur la chute de pression des nouveaux frigorige da*. *24*.

[31] Cavallini, A., Del Col, D., Doretti, L., Matkovic, M., Rossetto, L., & Zilio, C. (2005). Condensation heat transfer and pressure gradient inside multiport minichannels. *Heat Transfer Engineering*, *26*(3), 45–55. https://doi.org/10.1080/01457630590907194

[32] Garimella, S., Andresen, U. C., Mitra, B., Jiang, Y., & Fronk, B. M. (2016). Heat Transfer During Near-Critical-Pressure Condensation of Refrigerant Blends. *Journal of Heat Transfer*, *138*(5). https://doi.org/10.1115/1.4032294

[33] Jiang, Y., & Garimella, S. (2003). Heat Transfer and Pressure Drop for Condensation of Refrigerant R-404A at Near-Critical Pressures. In *ASHRAE Winter Meetings CD, Technical and Symposium Papers* (Vol. 2003).

[34] Andresen, U. C. (2006). *Supercritical gas cooling and near-critical-pressure condensation of refrigerant blends in microchannels*.

[35] Del Col, D., Torresin, D., & Cavallini, A. (2010). Heat transfer and pressure drop during condensation of the low GWP refrigerant R1234yf. *International Journal of Refrigeration*, *33*(7), 1307–1318. https://doi.org/10.1016/j.ijrefrig.2010.07.020

[36] Del Col, D., Bortolato, M., & Bortolin, S. (2014). Comprehensive experimental investigation of two-phase heat transfer and pressure drop with propane in a minichannel. *International Journal of Refrigeration*, *47*, 66–84. https://doi.org/10.1016/j.ijrefrig.2014.08.002

[37] Longo, G. A., Mancin, S., Righetti, G., & Zilio, C. (2017). Saturated vapour condensation of HFC404A inside a 4 mm ID horizontal smooth tube: Comparison with the long-term low GWP substitutes HC290 (Propane) and HC1270 (Propylene). *International Journal of Heat and Mass Transfer*, *108*, 2088–2099. https://doi.org/10.1016/j.ijheatmasstransfer.2016.12.087

[38] Longo, G. A., Mancin, S., Righetti, G., & Zilio, C. (2018). Saturated vapour condensation of R410A inside a 4 mm ID horizontal smooth tube: Comparison with the low GWP substitute R32. *International Journal of Heat and Mass Transfer*, *125*, 702–709. https://doi.org/10.1016/j.ijheatmasstransfer.2018.04.109

[39] Longo, G. A., Mancin, S., Righetti, G., & Zilio, C. (2019). Saturated vapour condensation of R134a inside a 4 mm ID horizontal smooth tube: Comparison with the low GWP substitutes R152a, R1234yf and R1234ze(E). *International Journal of Heat and Mass Transfer*, *133*, 461–473. https://doi.org/10.1016/j.ijheatmasstransfer.2018.12.115

[40] Ghim, G., & Lee, J. (2017). Condensation heat transfer of low GWP ORC working fluids in a horizontal smooth tube. *International Journal of Heat and Mass Transfer*, *104*, 718–728. https://doi.org/10.1016/j.ijheatmasstransfer.2016.08.090

[41] Patel, T., Parekh, A. D., & Tailor, P. R. (2020). Experimental analysis of condensation heat transfer and frictional pressure drop in a horizontal circular mini channel. *Heat and Mass Transfer/Waerme-Und Stoffuebertragung*, *56*(5), 1579–1600. https://doi.org/10.1007/s00231-019-02798-5

[42] Song, Q., Chen, G., Xue, H., Zhao, Y., & Gong, M. (2019). R14 flow condensation heat transfer performance: Measurements and modeling based on two-phase flow patterns. *International*

Journal of Heat and Mass Transfer, *136*, 298–311. https://doi.org/10.1016/j.ijheatmasstransfer.2019.02.105

[43] Zhuang, X. R., Chen, G. F., Zou, X., Song, Q. L., & Gong, M. Q. (2017). Experimental investigation on flow condensation of methane in a horizontal smooth tube. *International Journal of Refrigeration*, *78*, 193–214. https://doi.org/10.1016/j.ijrefrig.2017.03.021

[44] Keniar, K., & Garimella, S. (2021). Experimental investigation of refrigerant condensation in circular and square micro- and mini- channels. *International Journal of Heat and Mass Transfer*, *176*, 121383. https://doi.org/10.1016/j.ijheatmasstransfer.2021.121383

[45] Moreira, T. A., Ayub, Z. H., & Ribatski, G. (2021). Convective condensation of R600a, R290, R1270 and their zeotropic binary mixtures in horizontal tubes. *International Journal of Refrigeration*, *130*(July), 27–43. https://doi.org/10.1016/j.ijrefrig.2021.06.031

[46] Huang, X., Ding, G., Hu, H., Zhu, Y., Peng, H., Gao, Y., & Deng, B. (2010). Influence of oil on flow condensation heat transfer of R410A inside 4.18 mm and 1.6 mm inner diameter horizontal smooth tubes. *International Journal of Refrigeration*, *33*(1), 158–169. https://doi.org/10.1016/j.ijrefrig.2009.09.008

[47] Illán-Gómez, F., López-Belchí, A., García-Cascales, J. R., & Vera-García, F. (2015). Experimental two-phase heat transfer coefficient and frictional pressure drop inside mini-channels during condensation with R1234yf and R134a. *International Journal of Refrigeration*, *51*, 12–23. https://doi.org/10.1016/j.ijrefrig.2014.11.014

[48] Del Col, D., Azzolin, M., Bortolin, S., & Berto, A. (2017). Experimental results and design procedures for minichannel condensers and evaporators using propylene. *International Journal of Refrigeration*, *83*(January 2015), 23–38. https://doi.org/10.1016/j.ijrefrig.2017.07.012

[49] Azzolin, M., Bortolin, S., & Del Col, D. (2019). Convective condensation at low mass flux: Effect of turbulence and tube orientation on the heat transfer. *International Journal of Heat and Mass Transfer*, *144*, 118646. https://doi.org/10.1016/j.ijheatmasstransfer.2019.118646

[50] Berto, A., Lavieille, P., Azzolin, M., Bortolin, S., Miscevic, M., & Del Col, D. (2021). Liquid film thickness and heat transfer measurements during downflow condensation inside a small diameter tube. *International Journal of Multiphase Flow*, *140*, 103649. https://doi.org/10.1016/j.ijmultiphaseflow.2021.103649

[51] Mikielewicz, D., & Mikielewicz, J. (2011). A common method for calculation of flow boiling and flow condensation heat transfer coefficients in minichannels with account of nonadiabatic effects. *Heat Transfer Engineering*, *32*(13–14), 1173–1181. https://doi.org/10.1080/01457632.2011.562728

[52] Mikielewicz, D., Wajs, J., Andrzejczyk, R., & Klugmann, M. (2016). Pressure drop of HFE7000 and HFE7100 during flow condensation in minichannels. *International Journal of Refrigeration*, *68*, 226–241. https://doi.org/10.1016/j.ijrefrig.2016.03.005

[53] Jakubowska, B., & Mikielewicz, D. (2019). an Improved Method for Flow Boiling Heat Transfer With Account of the Reduced Pressure Effect. *Thermal Science*, *23*, S1261–S1272. https://doi.org/10.2298/TSCI19S4261J

[54] Mikielewicz, D., & Mikielewicz, J. (2022). An improved Müller-Steinhagen and Heck model for two phase pressure drop modelling at high reduced pressures. *Journal of Power Technologies*, *102*(3), 81–87.

[55] Shah, M. M. (1979). A general correlation for heat transfer during film condensation inside pipes. *International Journal of Heat and Mass Transfer*, *22*(4), 547–556. https://doi.org/10.1016/0017-9310(79)90058-9

[56] Shah, M. M. (2009). An improved and extended general correlation for heat transfer during condensation in plain tubes. *HVAC and R Research*, *15*(5), 889–913. https://doi.org/10.1080/10789669.2009.10390871

[57] Shah, M. M. (2019). Improved correlation for heat transfer during condensation in conventional and mini/micro channels. *International Journal of Refrigeration*, *98*, 222–237. https://doi.org/10.1016/j.ijrefrig.2018.07.037

[58] Bohdal, T., Charun, H., & Sikora, M. (2011). Comparative investigations of the condensation of R134a and R404A refrigerants in pipe minichannels. *International Journal of Heat and Mass Transfer*, *54*(9–10), 1963–1974. https://doi.org/10.1016/j.ijheatmasstransfer.2011.01.005

[59] Dorao, C. A., & Fernandino, M. (2018). Simple and general correlation for heat transfer during flow condensation inside plain pipes. *International Journal of Heat and Mass Transfer*, *122*, 290–305. https://doi.org/10.1016/j.ijheatmasstransfer.2018.01.097

[60] Shah, M. M. (2022). Improved correlation for heat transfer during condensation in mini and macro channels. *International Journal of Heat and Mass Transfer*, *194*, 123069. https://doi.org/10.1016/j.ijheatmasstransfer.2022.123069

[61] Costa-Patry, E., & Thome, J. R. (2013). Flow pattern-based flow boiling heat transfer model for microchannels. *International Journal of Refrigeration*, *36*(2), 414–420. https://doi.org/10.1016/j.ijrefrig.2012.12.006

[62] El Hajal, J., Thome, J. R., & Cavallini, A. (2003). Condensation in horizontal tubes, part 1: two-phase flow pattern map. *International Journal of Heat and Mass Transfer*, *46*(18), 3349–3363. https://doi.org/10.1016/S0017-9310(03)00139-X

[63] Cavallini, A., Censi, G., Del Col, D., Doretti, L., Longo, G. A., & Rossetto, L. (2002). Condensation of halogenated refrigerants inside smooth tubes. *HVAC and R Research*, *8*(4), 429–451. https://doi.org/10.1080/10789669.2002.10391299

[64] Coleman, J. W., & Garimella, S. (2003). Two-phase flow regimes in round, square and rectangular tubes during condensation of refrigerant R 134a. *International Journal of Refrigeration*, *26*(1), 117–128. https://doi.org/10.1016/S0140-7007(02)00013-0

[65] Kattan, N., Thome, J. R., & Favrat, D. (1998). Flow boiling in horizontal tubes: Part 1-development of a diabatic two-phase flow pattern map. *Journal of Heat Transfer*, *120*(1), 140–147. https://doi.org/10.1115/1.2830037

[66] Cheng, L., Ribatski, G., Wojtan, L., & Thome, J. R. (2006). New flow boiling heat transfer model and flow pattern map for carbon dioxide evaporating inside horizontal tubes. *International Journal of Heat and Mass Transfer*, *49*(21–22), 4082–4094. https://doi.org/10.1016/j.ijheatmasstransfer.2006.04.003

[67] Revellin, R., & Thome, J. R. (2007). A new type of diabatic flow pattern map for boiling heat transfer in microchannels. *Journal of Micromechanics and Microengineering*, *17*(4), 788–796. https://doi.org/10.1088/0960-1317/17/4/016

[68] Kim, S. M., Kim, J., & Mudawar, I. (2012). Flow condensation in parallel micro-channels - Part 1: Experimental results and assessment of pressure drop correlations. *International Journal of Heat and Mass Transfer*, *55*(4), 971–983. https://doi.org/10.1016/j.ijheatmasstransfer.2011.10.013

[69] Billiet, M., Ameel, B., Charnay, R., Revellin, R., & De Paepe, M. (2018). Flow regime based heat transfer correlation for R245fa in a 3 mm tube. *International Journal of Heat and Mass Transfer*, *117*, 1304–1311. https://doi.org/10.1016/j.ijheatmasstransfer.2017.10.062

[70] Pysz, M., Głuch, S., & Mikielewicz, D. (2023). Experimental study of flow boiling pressure drop and heat transfer of R1233zd(E) at moderate and high saturation temperatures. *International Journal of Heat and Mass Transfer*, *204*. https://doi.org/10.1016/j.ijheatmasstransfer.2023.123855

[71] Sikora, M. (2021). Flow structure investigations during novec refrigerant condensation in minichannels. *Materials*, *14*(22). https://doi.org/10.3390/ma14226889

[72] Qiu, Y., Garg, D., Zhou, L., Kharangate, C. R., Kim, S. M., & Mudawar, I. (2020). An artificial neural network model to predict mini/micro-channels saturated flow boiling heat transfer coefficient based

on universal consolidated data. *International Journal of Heat and Mass Transfer*, *149*. https://doi.org/10.1016/j.ijheatmasstransfer.2019.119211

[73] Zhou, L., Garg, D., Qiu, Y., Kim, S. M., Mudawar, I., & Kharangate, C. R. (2020). Machine learning algorithms to predict flow condensation heat transfer coefficient in mini/micro-channel utilizing universal data. *International Journal of Heat and Mass Transfer*, *162*, 120351. https://doi.org/10.1016/j.ijheatmasstransfer.2020.120351

[74] Moradkhani, M. A., Hosseini, S. H., & Karami, M. (2022). Forecasting of saturated boiling heat transfer inside smooth helically coiled tubes using conventional and machine learning techniques. *International Journal of Refrigeration*, *143*(May), 78–93. https://doi.org/10.1016/j.ijrefrig.2022.06.036

[75] Moradkhani, M. A., Hosseini, S. H., & Song, M. (2022). Robust and general predictive models for condensation heat transfer inside conventional and mini/micro channel heat exchangers. *Applied Thermal Engineering*, *201*(PA), 117737. https://doi.org/10.1016/j.applthermaleng.2021.117737

[76] Nie, F., Wang, H., Zhao, Y., Song, Q., Yan, S., & Gong, M. (2023). A universal correlation for flow condensation heat transfer in horizontal tubes based on machine learning. *International Journal of Thermal Sciences*, *184*(November 2022), 107994. https://doi.org/10.1016/j.ijthermalsci.2022.107994

[77] Mattiuzzo, N., Azzolin, M., Berto, A., Bortolin, S., & Del Col, D. (2023). Condensation heat transfer and pressure drop of R1234yf/HFC mixtures inside small diameter channels. *International Journal of Thermal Sciences*, *189*. https://doi.org/10.1016/j.ijthermalsci.2023.108258

[78] Hughes, M. T., Chen, S. M., & Garimella, S. (2022). Machine-learning-based heat transfer and pressure drop model for internal flow condensation of binary mixtures. *International Journal of Heat and Mass Transfer*, *194*. https://doi.org/10.1016/j.ijheatmasstransfer.2022.123109

[79] Garimella, S., & Christensen, R. N. (1995). Heat Transfer and Pressure Drop Characteristics of Spirally Fluted Annuli: Part II-Heat Transfer. *Journal of Heat Transfer*, *117*(1), 61–68. https://doi.org/10.1115/1.2822324

[80] Gnielinski, V. (2013). On heat transfer in tubes. *International Journal of Heat and Mass Transfer*, *63*, 134–140. https://doi.org/10.1016/j.ijheatmasstransfer.2013.04.015

[81] Bergman, T., Lavine, A., Incopera, F., & Dewitt, D. (2011). *Fundamentals of Heat and Mass Transfer* (7th ed.). John Wiley & Sons, Inc.

[82] Çengel, Y., & Ghajar, A. (2015). *Heat and Mass Transfer* (5th ed.). Mc Graw Hill.

[83] Taler, D., & Taler, J. (2017). Simple heat transfer correlations for turbulent tube flow. *Journal of Thermal Science*, *26*(4), 339–348. https://doi.org/10.1007/s11630-017-0947-2

[84] Klein, S. A. (2015). *EES Engineering Equation Solver for Microsoft Windows Operating Systems*. F-Chart Software.

[85] Taylor, B. N., & Kuyatt, C. E. (2001). Guidelines for Evaluating and Expressing the Uncertainty of NIST Measurement Results: Appendix D1. Terminology. *National Institute for Standards and Technology, Gaithersburg, MD*, D.1.1.2. http://physics.nist.gov/TN1297

[86] Charnay, R., Revellin, R., & Bonjour, J. (2015). Flow boiling heat transfer in minichannels at high saturation temperatures: Part I - Experimental investigation and analysis of the heat transfer mechanisms. *International Journal of Heat and Mass Transfer*, *87*, 636–652. https://doi.org/10.1016/j.ijheatmasstransfer.2015.03.081

[87] Shah, M. M. (2019). Improved correlation for heat transfer during condensation in conventional and mini/micro channels. *International Journal of Refrigeration*, *98*, 222–237. https://doi.org/10.1016/j.ijrefrig.2018.07.037

[88] Głuch, S., Niksa-Rynkiewicz, T., Mikielewicz, D., & Stomma, P. (2023). Application of Feed Forward Neural Networks for modeling of heat transfer coefficient during flow condensation for low and high values of saturation temperature. *36th International Conference on Efficiency, Cost, Optimization, Simulation and Environmental Impact of Energy Systems, ECOS 2023*, 391–401. https://doi.org/10.52202/069564-0036

[89] Goodfellow, I., Bengio, Y., & Courville, A. (2016). *Deep Learning*. MIT Press.

[90] Revellin, R., & Thome, J. R. (2007). Experimental investigation of R-134a and R-245fa two-phase flow in microchannels for different flow conditions. *International Journal of Heat and Fluid Flow*, *28*(1 SPEC. ISS.), 63–71. https://doi.org/10.1016/j.ijheatfluidflow.2006.05.009

[91] Charnay, R., Revellin, R., & Bonjour, J. (2013). Flow pattern characterization for R-245fa in minichannels: Optical measurement technique and experimental results. *International Journal of Multiphase Flow*, *57*, 169–181. https://doi.org/10.1016/j.ijmultiphaseflow.2013.05.015

[92] Churchill, S. W., & Chu, H. H. S. (1975). Correlating equations for laminar and turbulent free convection from a vertical plate. *International Journal of Heat and Mass Transfer*, *18*(11), 1323–1329. https://doi.org/10.1016/0017-9310(75)90243-4

List of Figures

List of Tables

Appendix 1: Experimental data points.

Table A1.1 Experimental data points for R1233zd(E) compensating inside 3 mm diameter horizontal channel

number	T_{sat} [°C]	G $\left[\frac{kg}{s \cdot m^2}\right]$	±G	x [−]	± x	α_{exp} $\left[\frac{W}{m^2 K}\right]$	$\pm\alpha_{exp}$	q $\left[\frac{W}{m^2}\right]$	±q	ΔT [K]	±ΔT
1	79.97	602.8	4.06	0.052	0.016	2827	646	161.9	31.0	57.43	0.55
2	79.52	607.9	4.10	0.116	0.016	3702	695	201.8	31.0	55.57	0.51
3	80.65	591.4	3.99	0.185	0.017	3910	675	215.3	30.2	55.85	0.49
4	81.2	598.5	4.04	0.253	0.017	4305	683	234.7	29.9	55.55	0.48
5	81.2	598.5	4.04	0.387	0.017	4263	680	234.7	29.9	55.05	0.47
6	81.35	595.4	4.01	0.521	0.017	5487	733	283.3	29.4	53.83	0.46
7	81.31	599.7	4.04	0.638	0.018	6505	832	321.5	31.1	53.23	0.46
8	81.53	596.9	4.02	0.783	0.018	7641	896	359.8	31.2	52.7	0.46
9	78.71	1001	6.75	0.020	0.013	3193	570	176.3	25.8	55.61	0.68
10	81.11	1003	6.76	0.043	0.014	3819	571	212.2	25.6	56.35	0.59
11	81.22	987.5	6.66	0.112	0.014	4698	609	251.8	25.6	54.6	0.51
12	82.73	987.5	6.66	0.197	0.014	5231	618	280.8	25.6	54.49	0.48
13	83.23	993	6.69	0.305	0.014	5754	629	304.3	25.2	53.64	0.47
14	83.48	942.4	6.35	0.624	0.015	7129	694	354.1	25.2	51.84	0.45
15	115.5	598.1	4.03	0.117	0.021	2779	477	213.7	30.8	75.04	0.53
16	115	611.1	4.12	0.171	0.020	2863	443	218.2	28.2	73.61	0.51
17	114.6	594.2	4.01	0.427	0.020	3647	464	266.1	27.8	71.05	0.48
18	114.9	591.4	3.99	0.505	0.021	3887	469	280.9	27.7	70.82	0.48
19	115.4	589.5	3.97	0.605	0.021	4141	471	296.5	27.4	70.66	0.48
20	114.6	594.2	4.01	0.697	0.021	4409	479	308.0	27.1	69.49	0.47
21	114.9	596.9	4.02	0.782	0.021	4613	484	319.8	27.1	69.52	0.47
22	135.9	595	4.01	0.145	0.025	2432	362	217.3	27.3	85.47	0.53
23	135.7	596.9	4.02	0.216	0.025	2673	363	235.7	26.9	84.42	0.51
24	135.7	585.5	3.95	0.449	0.025	3079	373	267.1	27.0	82.94	0.49
25	135.8	593	4.00	0.528	0.026	3257	382	280.3	27.3	82.55	0.49
26	135.6	589.1	3.97	0.661	0.026	3507	390	297.1	27.4	81.9	0.48
27	135.5	601.6	4.06	0.749	0.026	3778	394	314.5	27.1	81.23	0.48
28	142.8	598.1	4.03	0.158	0.028	2559	356	243.2	28.6	91.67	0.54
29	143.5	597.7	4.03	0.206	0.029	2718	357	258.5	28.6	91.85	0.53
30	144.5	598.1	4.03	0.265	0.029	2799	343	267.9	27.6	92.16	0.52
31	144.9	594.2	4.01	0.336	0.029	2934	342	280.0	27.4	91.98	0.51
32	144.8	595.4	4.01	0.437	0.029	3110	343	294.1	27.1	91.2	0.50
33	145.2	595.4	4.01	0.510	0.030	3261	344	306.7	27.0	91.04	0.50
34	144.9	592.6	4.00	0.652	0.030	3423	349	318.5	27.0	90.31	0.49
35	145.4	587.9	3.96	0.747	0.030	3586	350	331.6	27.0	90.45	0.49
36	151.8	592.2	3.99	0.171	0.032	2276	243	215.0	19.5	90.05	0.53
37	152.2	596.5	4.02	0.341	0.036	3040	388	280.4	30.2	89.86	0.51
38	152.7	593.4	4.00	0.501	0.037	3114	373	288.1	29.2	89.69	0.50
39	153.2	591.4	3.99	0.631	0.037	3302	371	303.6	28.8	89.63	0.50

40	151.7	595	4.01	0.291	0.035	2761	368	256.8	29.0	89.73	0.52
41	151.2	597.7	4.03	0.170	0.035	2631	387	244.1	30.6	90.1	0.54
42	151.9	595.4	4.01	0.365	0.036	2904	391	269.7	30.7	89.69	0.51

Experimental data is presented in Table A1.1. d is internal tube diameter, T_{sat} is saturation temperature, G is mass velocity, α_{exp} condensation heat transfer coefficient, q is heat flux and ΔT difference between wall and refrigerant temperature. ± represent measurement uncertainty.

Appendix 2: EES Postprocessing Code.

"data"

Fluid$='water'

Fluid2$='R1233zd(E)'

"section internal diameter"

d1=0.003 [m]

"section outer diameter"

d2=0.004 [m]

"outer diameter annulus water cooling"

d3=0.005 [m]

"inner diameter construction tube 1/4'"

d4=0.0044 [m]

" section length heat transfer "

l=0.05 [m]

"length from heat transfer area to the end of the tube"

l2=0.042 [m]

{P=1 [mpa]}

"dh=4A/p for annulus"

dh=d3-d2

"measured copper heat conduction coeffcient"

kc= kexp [W/(m*K)]

kexp=124.6 [W/(m*K)]

Pii=3.1415927

A1=2*Pii*d1/2*l

A2=2*Pii*d2/2*l

A3=Pii*(d3/2)^2-Pii*(d2/2)^2

A4=Pii*(d4/2)^2

A5=Pii*(d1/2)^2

diso1=0.0044

diso2=0.0041

diso=(diso1+diso2)/2

liso=2.07

Aiso=3.14*liso*diso

"raw input data"

{t8=1; t9=1; t10=1; t11=1; t12=1; t13=1; t14=1; t15=1; t16=1; t17=1; t18=1; t19=1; t20=1; t21=1; t22=1; t23=1; t24=1; t25=1; } {t5=1 t6=1 t7=1}

{Q=300

t0=1

t1=1

t2=1

p1=8.306287633 [bar]

p2=8.3438684 [bar]

pdiff=0.9110828 [kpa]

mas=17.2457131 [hg/h]

ppre=9.5035651 [bar]

pl1=0.968973333 [bar]

pl2=0.932090633 [bar]

ML1=16.75 [g/s]

ML2=1.8 [g/s]

tc3=19.86567993 [C]

tc4=24.4148787 [C]

tc20=24.61376893 [C]

tc21=23.99541383 [C]

tc22=54.32942013 [C]

tc23=60.78859043 [C]

t6=1

"ambient temperature"

t5=16.8 [C]}

p1m=p1/10

p2m=p2/10

pdm=pdiff/1000

“average temperature water section loop1”

tl1=(tc20+tc21)/2

“average temperature water loop2”

tl2=(tc3+tc4)/2

“average temperature refrigerant”

tr=(tc22+tc23)/2

tr2=(tc20+tc21)/2

“average pressure refrigerant”

Pavg=(P1+P2)/2 [bar]

ML1g=ML1/1000 [kg/s]

ML2g=ML2*rol/1000000 [kg/s]

"measured deltaP"

deltaP=P1-P2-dp0

dp0=-0.041915704

"dp0 average from measurment without flow"

mass=mas/3600 [kg/s]

Qwat=ML2g*cpl*(tc4-tc3)-bil3

Qwat2=ML2g*cpl*(tc4-tc3)-bil3-qfinf-qfinf2

Qref=mass*cpl2*(tc23-tc22)

QloopI=ML1g*cpl3*(tc20-tc21)

"billance loop I"

deltaTB=tc21-17

“data form experiment on heat loss form loop1”

Bil3=**interpolate1**('BL1','bil2','deltaT',deltaT=deltaTB, 1, 7)

"wall heat transfer"

Rw=**ln**(d2/d1)/(2*PI*kc*l)

hwall=1/(Rw*a2)

"water heat transfer"

Rel3=(ML1g*dh)/(A3*mul3)

Nu3db=0.023*Rel3^(0.8)*Pral3^0.4

{Nu3=3.66}

Nu3=**if**(Rel3,2300,3.66,0.023*Rel3^(4/5)*Pral3^0.4,0.023*Rel3^(4/5)*Pral3^0.4)

ho=kl3*Nu3/dh

hodb=kl3*Nu3db/dh

"Seider Tate"

Nust=1.86*Rel3^(1/3)*Pral3^(1/3)*(d3/l)^(1/3)*(must/mul3)

must=**viscosity**(Fluid$,***P***=Pl1,***T***=tc22)

host=kl3*Nust/dh

"Garimella and Christensen 1995"

Nugc=0.025*rel3^0.78*Pral3^0.48*r^(-0.14)

r=d3/d2

hogc=kl3*Nugc/dh

"Gnielinski 2013"

twl2=tl1+hr/hogc*(tr-tl1)

ff2=(1.8***log10**(Rel3)-1.5)^(-2)

k2=(Pral3/Praw2)^0.11

Praw2=**prandtl**(Fluid$,***P***=Pl1,***T***=twl2)

NuG3= ((ff2/8)*(Rel3-1000)*Pral3)/(1+12.7*(ff2/8)^(0.5)*(Pral3^(2/3)-1))*(1+(dh/l)^(2/3))*K2

hoG3=NuG3*kl2/d1

Rel2=(mass*d1)/(A5*mul4)

Rel4=(mass*d4)/(d4^2*3.14/4*mul4)

Rel2D=(mass*d1)/(A5*mul4)

"Dittus-Boelter cooling"

n=0.3

{Nul=0.23*Rel^(4/5)*Pral^n}

Nul2=**if**(Rel2,1100,3.66,0.023*Rel2^(4/5)*Pral2^n,0.023*Rel2^(4/5)*Pral2^n)

alfal=Nul2*kl2/d1

Nul3=**if**(Rel2,1100,3.66,0.023*Rel2^(4/5)*Pral2^0.4,0.023*Rel2^(4/5)*Pral2^0.4)

alfal2=Nul3*kl2/d1

"Gnielinski76"

f=0.033

NuG= ((f/8)*(Rel2-1000)*Pral2)/(1+12.7*(f/8)^(0.5)*(Pral2^(2/3)-1))

alfalG=NuG*kl2/d1

"turbulent Darcy friction factor Gnielinski 2013"

ff=(1.8***log10**(Rel2)-1.5)^(-2)

k=(Pral2/Prw)^0.11

Prw=**prandtl**(Fluid2$,***P***=P2,***T***=Tr2)

"Gnielinski 2013"

NuG2= ((ff/8)*(Rel2-1000)*Pral2)/(1+12.7*(ff/8)^(0.5)*(Pral2^(2/3)-1))*(1+(d1/l)^(2/3))*K

alfalG2=NuG2*kl2/d1

"Taler"

NuT=c1*Rel2^c2*Pral2^c3*(1+(d1/l)^(2/3))

c1=**if**(Pral2,3,0.01253,0.01253,0.00881)

c2=**if**(Pral2,3,0.8413,0.8413,0.8991)

c3=**if**(Pral2,3,0.6179,0.6179,0.3911)

alfaT=NuT*kl2/d1

{alfav=Nuv*kv/d}

“mass velocity"

G=mass/A5

"Mikielewicz modification"

"RMSH"

CON=(sigma2/(gearth*(rol4-rov4)))^(1/2)/d1

f1=**if**(Rel2,2300,(rov4/rol4)*(mul4/muv4),(rov4/rol4)*(mul4/muv4)^0.25,(rov4/rol4)*(mul4/muv4)^0.25)

f1z=**if**(Rel2,2300,(kl4/kv4),(muv4/mul4)*(kl4/kv4)^(1.5)*(Cpl4/Cpv4),(muv4/mul4)*(kl4/kv4)^(1.5)*(Cpl4/Cpv4))

RMSH=(1+2*(1/f1-1)*xavg*CON^m)*(1-xavg)^(1/3)+1/f1z*xavg^3

m=-0.875

"Mikielewicz 2011"

atpbal=(RMSH^nn)^0.5

"modification for r1233zde"

apoprawka=((RMSH^nn)/Bd^(0.1))^0.5

nn=0.76

htc=alfal*atpbal

htcPC=alfal*apoprawka

"LMTD"

dTa=tc23-tc21

dTb=tc22-tc20

LMTD=(dTa-dTb)/(**ln**(dTa/dTb))

UA=Qwat2/LMTD

UA2=Qwat/LMTD*0.7

“experiment heat transfer coefficient hr”

Rwat=1/(hogc*Pii*d2*l)

Rtotal=1/UA

Rrefg=Rtotal-Rwat-Rw

Rrefg=1/(hr*Pii*d1*l)

hrtest=1/(Rrefg*3.14*d1*l)

"test"

Rczynnika=1/(alfal*Pii*d1*l)

Rzzz=Rczynnika+Rwat+Rw

zasth=qref/(a2*lmtd)

hx=20000

uu=UA/a1

hzzz=1/(1/uu-1/hodb)

"deltaT and heat flux"

qq=Qwat/A1

deltaT=tr-tr2

"calcualtions of heat transfer through wall lenght before and after section"

l3=0.002755 [m]

d6=0.00635 [m]

m3=((alfalG2*peri)/(kexp*Ac2))^(0.5)

Ac2=3.14*(d6^2/4-d1^2/4)

"adaibatic tip"

peri=d1*3.14

"inlet"

hogc*(Tb-TC21)*d2=htcPC*(TC23-Tb)*d1

"outlet"

hogc*(Tb2-TC20)*d2=htcPC*(TC22-Tb2)*d1

qfadia=(htcPC*peri*kexp*Ac2)*(TC23-Tb)*tanh(m3*l3)

qfadia2=(htcPC*peri*kexp*Ac2)*(TC22-Tb2)*tanh(m3*l3)

"infinitly long tip"

qfinf=(htcPC*peri*kexp*Ac2)*(TC23-Tb)

qfinf2=(htcPC*peri*kexp*Ac2)*(TC22-Tb2)

"average quality"

hh0=enthalpy(Fluid2$,T=t0 ,P=P1)

H0=hh0*mass

hhx1=**enthalpy**(Fluid2$,***T***=Tr ,***x***=1)

hhx0=**enthalpy**(Fluid2$,***T***=Tr ,***x***=0)

Hx1=hhx1*mass-H0

Hx0=hhx0*mass-H0

Hevap=hx1-hx0

Qr=effipreh*Q

xavg=(Qr-hx0-(Qwat/2))/Hevap

"inlet quality"

hhx1_2=**enthalpy**(Fluid2$,***T***=Tc23 ,***x***=1)

hhx0_2=**enthalpy**(Fluid2$,***T***=Tc23 ,***x***=0)

Hx1_2=hhx1_2*mass-H0

Hx0_2=hhx0_2*mass-H0

Hevap2=hx1_2-hx0_2

x2in= (Qr-hx0_2)/hevap2

"outlet quality"

hhx1_3=**enthalpy**(Fluid2$,***T***=Tc22,***x***=1)

hhx0_3=**enthalpy**(Fluid2$,***T***=Tc22 ,***x***=0)

Hx1_3=hhx1_3*mass-H0

Hx0_3=hhx0_3*mass-H0

Hevap3=hx1_3-hx0_3

x3out= (Qr-hx0_3-Qwat)/hevap3

“properties”

"water loop 2"

mul=**viscosity**(Fluid$,***P***=Pl2,***T***=tl2)

rol=**density**(Fluid$,***P***=Pl2,***T***=tl2)

Pral=**prandtl**(Fluid$,***P***=Pl2,***T***=tl2)

kl=**conductivity**(Fluid$,***P***=Pl2,***T***=tl2)

Cpl=**cp**(Fluid$,***P***=Pl2,***T***=tl2)

"refrigerant"

mul2=**viscosity**(Fluid2$,***P***=Pavg,***T***=Tr)

rol2=**density**(Fluid2$,***P***=Pavg,***T***=Tr)

Pral2=**prandtl**(Fluid2$,***P***=Pavg,***T***=Tr)

kl2=**conductivity**(Fluid2$,***P***=Pavg,***T***=Tr)

Cpl2=**cp**(Fluid2$,***P***=Pavg,***T***=Tr)

Pcrit=**p_crit**(Fluid2$)

sigma2=**surfacetension**(Fluid2$,***T***=Tr)

gearth=9.71

rol4=**density**(Fluid2$,***T***=Tr, ***x***=0)

rov4=**density**(Fluid2$,***T***=Tr, ***x***=1)

mul4=**viscosity**(Fluid$,***T***=Tr,***x***=0)

muv4=**viscosity**(Fluid$,***T***=Tr,***x***=1)

sigma4=**surfacetension**(Fluid$,***T***=Tr)

Pral4=**prandtl**(Fluid$,***T***=Tr,***x***=0)

Prav4=**prandtl**(Fluid$, ***T***=Tr,***x***=1)

kl4=**conductivity**(Fluid$,***T***=Tr,***x***=0)

kv4=**conductivity**(Fluid$,***T***=Tr,***x***=1)

Cpl4=**cp**(Fluid$,***T***=Tr,***x***=0)

Cpv4=**cp**(Fluid$,***T***=Tr,***x***=1)

"Bond"

Bd=gearth*(rol4-rov4)*d1^2/sigma4

"water loop 1"

mul3=**viscosity**(Fluid$,***P***=Pl1,***T***=tl1)

rol3=**density**(Fluid$,***P***=Pl1,***T***=tl1)

Pral3=**prandtl**(Fluid$,***P***=Pl1,***T***=tl1)

kl3=**conductivity**(Fluid$,***P***=Pl1,***T***=tl1)

Cpl3=**cp**(Fluid$,***P***=Pl1,***T***=tl1)

Appendix 3: EES code modelling of heat transfer coefficient during condensation.

```
"input data"
{"synthetic 2 natural 1"
SN=
"refrigerant name"
Fluid$=
"diameter"
d=
"saturation temperature in centigrade"
TsC=
"Mass velocity"
G
"quality"
x
"experimental heat transfer coefficient"
htcexp=}

Ts=TsC+273.15
P=pressure(Fluid$,T=TS,x=0)

"reduced pressure"

Pr=P/Pc

"calcualtions"

Pc=p_crit(Fluid$)
```

"Reynolds"

Rel=G*d/mul

Rev=G*d/muv

Resl=G*(1-x)*d/mul

Resv=G*x*d/muv

Retf=Resl+Resv

"Confinement number"

CON=(sigma/(gearth*(rol-rov)))^(1/2)/d

"RMS"

"one phase cooling"

"dittusboelter cooling"

n=0.3

Nul=if(Rel,2300,4.36,0.023*Rel^(4/5)*Pral^n,0.023*Rel^(4/5)*Pral^n)

Nuv=if(Rev,2300,4.36,0.023*Rev^(4/5)*Prav^n,0.023*Rev^(4/5)*Prav^n)

alfal=Nul*kl/d

alfav=Nuv*kv/d

"RMSH"

"turbulent flow"

{f1=(rol/rov)*(mul/muv)^0.25

f1z=(muv/mul)*(kl/kv)^(1.5)*(Cpl/Cpv)}

"laminar flow"

{ f1=(rol/rov)*(mul/muv)

f1z=(kl/kv)}

f1=if(Rel,2300,(rov/rol)*(mul/muv),(rov/rol)*(mul/muv)^0.25,(rov/rol)*(mul/muv)^0.25)

f1z=if(Rel,2300,(kl/kv),(muv/mul)*(kl/kv)^(1.5)*(Cpl/Cpv),(muv/mul)*(kl/kv)^(1.5)*(Cpl/Cpv))

RMSH=(1+2*(1/f1-1)*x*CON^m)*(1-x)^(1/3)+1/f1z*x^3

m=-0.875

"Mikielewicz 2011"

atpbal=(RMSH^nn)^0.5

"modificaton Mikieleiwcz"

apoprawka=((RMSH^nn)*Con^(sg))^0.5

sg=0.1+0.28*Pr

a1=1

nn=if(Rel,2300,0.76,0.76,0.76)

htc=alfal*atpbal

htcPC=alfal*apoprawka

dhtcM=htcexp-htc

dhtcJ=htcexp-htcPC

dhtcM%=dhtcM/htcexp*100

dhtcJ%=dhtcJ/htcexp*100

"other methods"

"Bohdal et al"

NuB=25.084*Rel^0.258*Pral^(-0.495)*Pr^(-0.288)*(x/(1-x))^0.266

htcB=NuB*kl/d

"Doarro Fernandino"

NuJ=0.023*Retf^0.8*Pratf^0.3

NuJJ=41.5*d^0.6*Retf^0.4*Pratf^0.3

Nudf=(NuJ^9+NuJJ^9)^(1/9)

HtcDF=Nudf*kl/d

"Shah 1979"

HtcS=0.023*Pral^0.4*Rel^0.8*((1-x)^0.8+(3.8*x^0.76*(1-x)^0.04)/(Pr^0.38))*kl/d

"Methods utilizing zones are finally processed in Excel with "if" and "and" logical functions"

"Cavalliini 2006"

Jg=(x*G)/(gearth*d*rov*(rol-rov))^0.5

JgT=((7.5/(4.3*Xtt^1.111))^(-3)+Ct^(-3))^(-1/3)

"For hydrocarbones : CT = 1.6 ; For other refrigerants : CT = 2.6"

CT=if(sn,1.5,2.6,2.6,1.6)

"lack of data on wall temperature in nearly all sources"

hstrat=0.725*(1+0.741*((1-x)/x)^0.3321)^(-1)*(kl^3*rol*(rol-rov)*gearth*hlv/(mul*d*dT))^0.25+(1-x^0.087)*alfalC

alfalC=0.023*Rel^0.8*Pral^0.4*kl/d

HC=alfalC*(1+1.128*x^0.817*(rol/rov)^0.3685*(mul/muv)^0.2363*(1-muv/mul)^2.144*Pral^(-0.1))

"Shah 2009"

hi=0.023*Rel^0.8*Pral^0.4*(mul/(14*muv))^n2*((1-x)^0.8+(3.8*x^0.76*(1-x)^0.04)/(Pr^0.38))*kl/d

n2=0.0058+0.557*pr

hNu=1.32*Resl^(-1/3)*((rol*(rol-rov)*gearth*kl^3)/(mul^2))^(1/3)

Z=(1/x-1)^0.8*Pr^0.4

"HTPII=hi+hNu"

JgC=0.98*(z+0.263)^(-0.62)

"Shah 2019"

hII=0.023*Rel^0.8*Pral^0.3*(1+1.128*x^0.8170*(rol/rov)^0.3685*(mul/muv)^0.2363*(1-muv/mul)^2.144*Pral^(-0.1))*(kl/d)

JgCC=0.95*(1.254+2.27*Z^1.249)^(-1)

"properities"

mul=viscosity(Fluid$,P=P,x=0)

muv=viscosity(Fluid$,P=P,x=1)

sigma=surfacetension(Fluid$,T=TS)

gearth=9.71

rol=density(Fluid$,P=P,x=0)

rov=density(Fluid$,P=P,x=1)

“Prandtl"

Pral=prandtl(Fluid$,P=P,x=0)

Prav=prandtl(Fluid$,P=P,x=1)

Pratf=Pral+Prav

kl=conductivity(Fluid$,P=P,x=0)

kv=conductivity(Fluid$,P=P,x=1)

Cpl=cp(Fluid$,P=P,x=0)

Cpv=cp(Fluid$,P=P,x=1)

"criterial numbers"

"superficial velocities"

Jv=(G*x)/(rov)

Jl=(G*(1-x))/(rol)

"lockhar Martinelli parameter"

Xtt=((mul/muv)^0.1*((1-x)/x)^0.9*(rov/rol)^0.5)

"Bond"

Bd=gearth*(rol-rov)*d^2/sigma

"boiling -do wrzenia"

"convection"

Co=((1-x)/x)^0.8*(rov/rol)^0.5

"Froude"

Frl=G^2/(rol^2*gearth*d)

Frv=G^2/(rov^2*gearth*d)

"liquid and vapour fraction froude"

Frlf=(G*(1-x))^2/(rol^2*gearth*d)

Frvf=(G*x)^2/(rov^2*gearth*d)

"Galileo number"

Ga=rol*gearth*(rol-rov)*d^3/mul^2

"Suratman"

Sul=sigma*rol*d/mul^2

Suv=sigma*rov*d/muv^2

"Weber"

wel=G^2*d/(rol*sigma)

wev=G^2*d/(rov*sigma)

"Weber fraction vapour liq"

welf=(G*(1-x))^2*d/(rol*sigma)

wevf=(G*x)^2*d/(rov*sigma)

R=(rol-rov)/rol

Appendix 4: Experimental measurement of heat conduction coefficient of tube used in main experiment.

Conduction coefficient of pure copper could be easily read from the property tables. Unfortunately materials sold as copper usually are alloys of copper with other metals. Some materials require higher yield strength but usually it is just cheaper to produce elements form alloys instead of pure copper. Difference of thermal resistance for thin 3 mm copper tube in conductance is negligible for values of conduction coefficient varying from 100 to 400 $\left[\frac{W}{mK}\right]$ for calculation of refrigerant heat transfer coefficient if only standard heat exchanger calculations are assumed. In reality Copper wall temperature equalize with refrigerant even 20 mm after water cooling surface in measurement section. Initially author conducted finite element method calculations in Ansys Steady Thermal simulation to investigate this effect. Example is resented in Figure 3.6. In this case copper tube is working as fin for heat exchanger.

This “fin” effect could increase measured refrigerant heat transfer coefficient even by 30%. To accurately calculate fin effect exact value of copper tube conduction coefficient was needed. For this purpose simple experiment was conducted. Spare 20 cm long copper tube, same as used in test section was utilised in experiment. 6 cm was submerged in boiling water. 14 cm was cooled by free convection. Ambient temperature and end of the tube temperature was measured by K thermocouples connected to NI DAQ used in main experiment. Experimental setup is shown in the Figure A4.1. Free convection heat transfer coefficient was calculated by Churchill and Chu [92] correlation. Conduction coefficient was derived from partial differential conduction equation (Fourier equation) - this case is similar to “finite length fin - adiabatic tip” case presented in heat transfer coursebooks [81,82]. Boiling water temperature was assumed to be 100°C. Ambient temperature was 16.8 °C and temperature 10 mm before the end of the tube was 44°C. Dimensions were measured by calliper. Copper conduction coefficient was calculated k=124.6 ±10.25. Uncertainty was calculated by method embodied into ESS in the same way as described in main thesis.

Figure A4.1 Experimental setup – boiling water, examined 200 mm long copper tube with thermocouple K attached 10 mm before the end of the tube.

Code from EES

```
Fluid4$='air'
t5=81 [C]
t6=16.8 [C]
Patm=1 [bar]
d4=0.004 [m]
d3=0.003 [m]
d5=0.00635 [m]
 Ac=3.14*(d4^2/4-d3^2/4)
 "Churchill and Chu free convection"
Ra4=(ro4*beta3*(t5-t6)*d4^3)/(nu_4*alpha_4)
Nu4=(0.6+(0.387*Ra4^(1/6))/(1+(0.559/Pra4)^(9/16))^(8/27))^2
hcon=k4*Nu4/d4
 mu4=viscosity(Fluid4$,T=t6)
ro4=density(Fluid4$,P=Patm,T=t6)
Pra4=prandtl(Fluid4$,T=t6)
k4=conductivity(Fluid4$,T=t6)
Cp4=cp(Fluid4$,T=t6)
nu_4=kinematicviscosity(Fluid4$,T=t6, P=Patm)
alpha_4=thermaldiffusivity(Fluid4$,T=t6, P=Patm)
{beta=linearexpcoef(Fluid$, T=t2)}
beta1=3.5*10^(-3) { 15 degc}
beta2=3.43*10^(-3) [1/K] { 20 degc}
beta3=beta1-(beta1-beta2)*(t5-15)/(20-15)
```

"derived partial differential equations for fin”

tx=44 [C]

l=0.14 [m]

l2=0.13 [m]

"m to calcualte k"

p=3.14*d4

m=((hcon*p)/(k*Ac))^(0.5)

h=8.929

Appendix 5: Code flow map prediction.

```
"data"
 {
Fluid$='r1233zd(e)'
d=0.003 [m]
pr=0.2
G= 300 [kg/(m^2*s)]
  xexp=1
 }
 q=0
 vl=G/rol
"input data reduced pressure"
 Pc=p_crit(Fluid$)
P=pr*Pc
TS=temperature(Fluid$, P=P,x=0)
"Reynolds"
Rel=G*d/mul
Rev=G*d/muv
"Confinement number"
CON=(sigma/(gearth*(rol-rov)))^(1/2)/d
"Weber"
wel=G^2*d/(rol*sigma)
wev=G^2*d/(rov*sigma)
"Eotwos Bond"
Bd=gearth*(rol-rov)*d^2/sigma
"Suratman"
Sul=sigma*rol*d/mul^2

Suv=sigma*rov*d/muv^2
```

"Zuhang 2016 annualr"

18.91*((mul/muv)^0.1*((1-xz)/xz)^0.9*(rov/rol)^0.5)^0.33=(2.45*(Rev^0.64)/(Suv^0.3*(1+1.09*((mul/muv)^0.1*((1-xz)/xz)^0.9*(rov/rol)^0.5)^0.039)^0.4))

"Zhuang bubbly"

4.38*((mul/muv)^0.1*((1-xzb)/xzb)^0.9*(rov/rol)^0.5)^0.45=(2.45*(Rev^0.64)/(Suv^0.3*(1+1.09*((mul/muv)^0.1*((1-xzb)/xzb)^0.9*(rov/rol)^0.5)^0.039)^0.4))

"Kim Mudawar 2012 annular"

24*((mul/muv)^0.1*((1-xk)/xk)^0.9*(rov/rol)^0.5)^0.41=(2.45*(Rev^0.64)/(Suv^0.3*(1+1.09*((mul/muv)^0.1*((1-xk)/xk)^0.9*(rov/rol)^0.5)^0.039)^0.4))

" Kim Mudawar bubbly"

7*((mul/muv)^0.1*((1-xkb)/xkb)^0.9*(rov/rol)^0.5)^0.2=(2.45*(Rev^0.64)/(Suv^0.3*(1+1.09*((mul/muv)^0.1*((1-xkb)/xkb)^0.9*(rov/rol)^0.5)^0.039)^0.4))

"Coalescing bubble/annular (CB/A) Ong and Thome"

xot=0.047*(CON^0.05)*(muv/mul)^0.7*(rov/rol)^0.6*Rev^0.8*Wel^(-0.91)

"isolated bubble/coalescing"

xotb=0.036*(CON^0.20)*(muv/mul)^0.65*(rov/rol)^0.9*Rev^0.75*Wel^(-0.91)*Boc^(0.25)

"Revellin 2006 annular"

xr=0.00014*(Rel^1.47)/(Wel^1.23)

"bubbly annular Revellin 2007 without BO"

BOC=10/(G*HLV)

xrb=0.763*((Rel*BOC)/Wev)^0.41

"Cavalini 2002"

2.5=(G*xcav)/(rov*(rol-rov)*gearth*d)^(0.5)

"Cheng 2006 anular"

xc=(1.8^(1/0.875)*(rov/rol)^(-1/1.75)*(mul/muv)^(-1/7)+1)^(-1)

"El Hajal 2003 annular"

xeh=((0.2914*(rov/rol)^(-1/1.75)*(mul/muv)^(-1/7))+1)^(-1)

"Present work-modification Revellin 2006"

"Intermittent/annular transition"

xSG=0.00014*(Rel^1.47)/(Wel^1.23)*bd^1.9/400

"Bubbly/Intermittent transition horizontal"

xSGbhori= 2*(((Rel/(G*HLV*wev))))^0.41

"Bubbly/Intermittent transition vertical"

xSGvert= 0.0109*(((Rel*10/(G*HLV*wev))))^0.41*con^(-2.8)

"properies"

gearth=9.71

mul=viscosity(Fluid$,P=P,x=0)

muv=viscosity(Fluid$,P=P,x=1)

sigma=surfacetension(Fluid$,T=TS)

rol=density(Fluid$,P=P,x=0)

rov=density(Fluid$,P=P,x=1)

Pral=prandtl(Fluid$,P=P,x=0)

Prav=prandtl(Fluid$,P=P,x=1)

kl=conductivity(Fluid$,P=P,x=0)

kv=conductivity(Fluid$,P=P,x=1)

Cpl=cp(Fluid$,P=P,x=0)

Cpv=cp(Fluid$,P=P,x=1)

HLV=enthalpy_vaporization(Fluid$,T=TS)

Appendix 6: Experimental Visualization of flow patterns in vertical channel

Flow patterns were captured during vertical up flow inside 3 mm inner diameter borosilicate tube after boiling test section. Tests were performed at reduced pressures (p_r) ranging from 0.2 to 0.8 of the critical pressure value, with mass velocities of 180, 265, 355, and 445 kg/(m²·s).

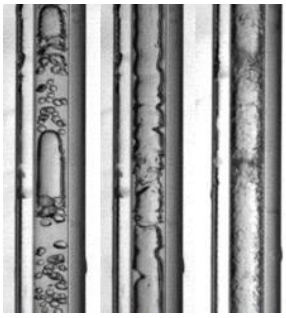

Figure A6.1 Flow patterns p_r=0,2 G=355 kg/(m2·s), quality respectively: 2%, 7%, 5,03%

In Figure A6.1 bubbly/slug flow and annular flow can be observed.

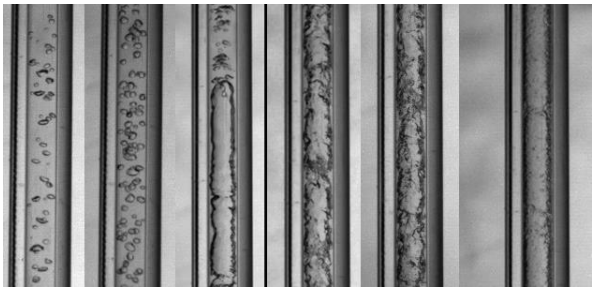

Figure A6.2 Flow patterns p_r=0,4 G=355 kg/(m2·s), quality respectively: 3,1%, 4,2%, 10%, 23,1%, 80,5%

In Figure A6.2 bubbly flow, slug flow, intermittent flow and annular flow. can be observed.

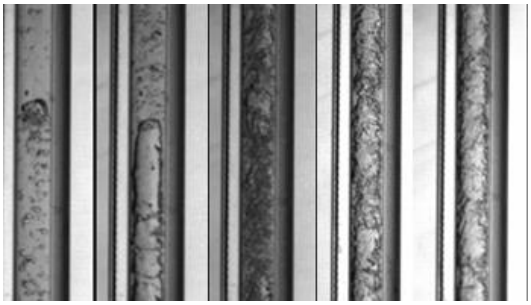

Figure A6.3 Flow patterns p_r=0,6 G=355 kg/(m2·s), quality respectively: 12%, 15,6%, 19,6%, 23,9%, 36,2%, 60,7%

In Figure A6.3 bubbly flow, slug flow, intermittent flow and annular flow. can be observed.

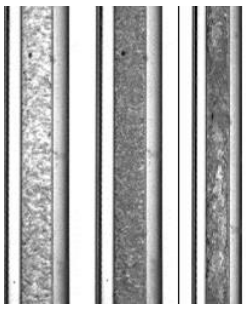

Figure A6.4 Flow patterns p_r=0,7 G=355 kg/(m2·s), quality respectively: 8.5%, 18.6%, 46%.

In Figure A6.4 bubbly flow, intermittent flow and annular flow can be observed.

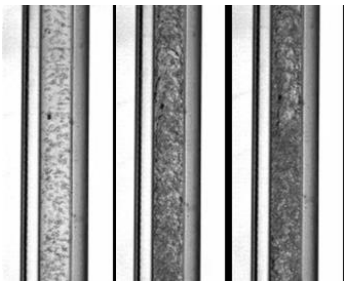

Figure A6.5 Flow patterns p_r=0,8 G=355 kg/(m2·s), quality respectively: 8.2%, 19%, 33,7%.

In Figure A6.5 bubbly flow and intermittent flow can be observed.

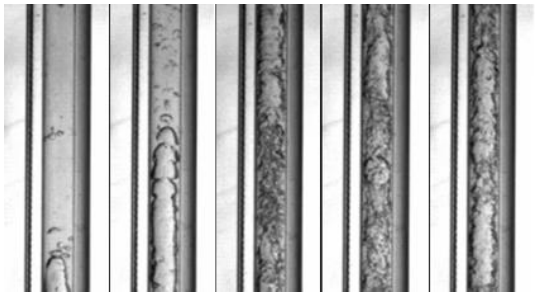

Figure A6.6 Flow patterns p_r=0,6 G=180 kg/(m2·s), quality respectively: 37,2%, 48,6%, 64,6%, 72,8%, 93%

In Figure A6.6 bubbly flow, slug flow, intermittent flow and annular flow. can be observed.

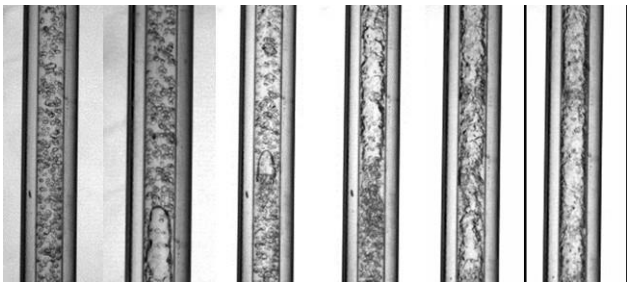

Figure A6.7 Flow patterns p_r=0,6 G=265 kg/(m2·s), quality respectively: 19,6%, 27%, 35,2%, 55,6%

In Figure A6.7 bubbly flow, slug flow, intermittent flow and annular flow. can be observed.

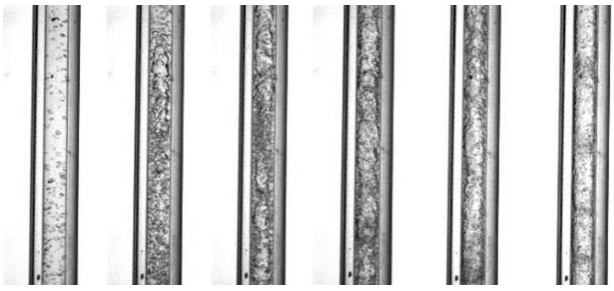

Figure A6.8 Flow patterns p_r=0,6 G=445 kg/(m2·s), quality respectively: 8,5%, 15,9%, 23,7%, 36,5%, 52,4%, 67,6%

In Figure A6.8 bubbly flow, slug flow, intermittent flow and annular flow. can be observed.